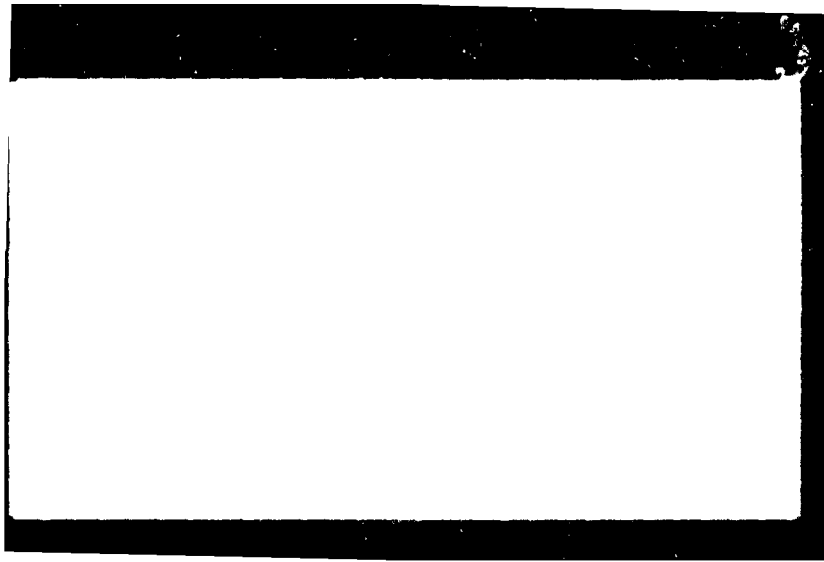


MICROCOPY RESOLUTION TEST CHART
NATIONAL BUREAU OF STANDARDS-1963-A



12

Contract N00014-81-K0039

A FUNDAMENTAL STUDY OF TOOL STEELS
PROCESSED FROM RAPIDLY SOLIDIFIED POWDERS

A. Lawley and M. J. Koczak
Department of Materials Engineering
Drexel University
Philadelphia, PA 19104

January 1983

Annual Report for Period 1 October 1981 - September 30, 1982

Approved for Public Release; Distribution Unlimited
Reproduction in whole or in part is permitted for
any purpose of the United States Government

Office of Naval Research
Materials Division
800 N. Quincy Street
Arlington, VA 22217



Accession For	
NTIS GRA&I	<input checked="" type="checkbox"/>
DTIC TAB	<input type="checkbox"/>
Unannounced	<input type="checkbox"/>
Justification	
By _____	
Distribution/	
Availability Codes	
Dist	Avail and/or Special
A	

Unclassified

SECURITY CLASSIFICATION OF THIS PAGE (When Data Entered)

REPORT DOCUMENTATION PAGE		READ INSTRUCTIONS BEFORE COMPLETING FORM
1. REPORT NUMBER	2. GOVT ACCESSION NO.	3. RECIPIENT'S CATALOG NUMBER
	AD/A126163	
4. TITLE (and Subtitle) A Fundamental Study of Tool Steels Processed From Rapidly Solidified Powders		5. TYPE OF REPORT & PERIOD COVERED Annual Report October 1981-September 1982
		6. PERFORMING ORG. REPORT NUMBER
7. AUTHOR(s) A. Lawley and M. J. Koczak		8. CONTRACT OR GRANT NUMBER(s) N00014-81-K0039
9. PERFORMING ORGANIZATION NAME AND ADDRESS Drexel University Department of Materials Engineering Philadelphia, PA 19104		10. PROGRAM ELEMENT, PROJECT, TASK AREA & WORK UNIT NUMBERS
11. CONTROLLING OFFICE NAME AND ADDRESS Department of the Navy Materials Division Office of Naval Research Arlington, VA 22217		12. REPORT DATE January 1983
		13. NUMBER OF PAGES 96
14. MONITORING AGENCY NAME & ADDRESS (if different from Controlling Office)		15. SECURITY CLASS. (of this report) Unclassified
		15a. DECLASSIFICATION/DOWNGRADING SCHEDULE
16. DISTRIBUTION STATEMENT (of this Report)		
17. DISTRIBUTION STATEMENT (of the abstract entered in Block 20, if different from Report)		
18. SUPPLEMENTARY NOTES		
19. KEY WORDS (Continue on reverse side if necessary and identify by block number) Tool steel powder atomization; powder characterization; powder consolidation; heat-treatment; microstructures.		
20. ABSTRACT (Continue on reverse side if necessary and identify by block number) A detailed microstructural examination has been made of T15 and Rex 25 high speed tool steels processed from rapidly solidified powders. Gas atomized powders were screened into selected size fractions, hot isostatically pressed to full density and heat-treated. Two HIPing temperatures, two austenitizing temperatures and three tempering temperatures were included in the study. Atomized and consolidated materials were characterized by means of optical and electron microscopy, x-ray diffraction and hardness. Both cellular and dendritic		

DD FORM 1 JAN 73 1473 EDITION OF 1 NOV 65 IS OBSOLETE

Unclassified
SECURITY CLASSIFICATION OF THIS PAGE (When Data Entered)

Unclassified

SECURITY CLASSIFICATION OF THIS PAGE(When Data Entered)

structures are present in the atomized powders depending on particle size, with MC carbides present primarily at cell boundaries. The partitioning of alloying elements in the cell structure decreases with decreasing particle size. Independent of prior particle size fraction, the carbide size distribution after HIPing is skewed to larger carbide sizes with increasing HIPing temperature, but with no significant change in volume fraction of carbides. At a given HIPing temperature the carbide size distribution for MC and M_6C carbides is dependent on prior particle size fraction; it is broader for the coarser size fractions. After heat-treatment, the constituents present are tempered martensite, MC and M_6C carbides, independent of prior particle size fraction and HIPing temperature. In T15, the size distribution of MC carbides after tempering is relatively independent of HIPing temperature. In contrast, there is a significant increase in the size spread of M_6C with increase in HIPing temperature; this is accompanied by a skewing of the M_6C carbide size distribution to coarser carbide sizes. Microstructures are analyzed in terms of particle cooling rate and structural stability during consolidation.

Unclassified

SECURITY CLASSIFICATION OF THIS PAGE(When Data Entered)

TABLE OF CONTENTS

	Page
ABSTRACT	
INTRODUCTION	1
EXPERIMENTAL PROCEDURE	2
1. Powder Atomization	2
2. Powder Characterization	3
3. Powder Consolidation	3
4. Characterization of HIPed Material	4
5. Heat-Treatment	5
6. Characterization of Heat-Treated Material	5
PART I: P/M T15 TOOL STEEL	6
RESULTS AND OBSERVATIONS	7
1. Atomized Powder	7
a) Scanning Electron Microscopy	7
b) Element Mapping	8
2. Consolidated Material	8
a) Scanning Electron Microscopy	8
b) EDAX	9
c) Quantitative Metallography	10
3. Heat-Treated Material	10
a) Scanning Electron Microscopy	10
b) X-Ray Diffraction	11
c) Quantitative Metallography	11
DISCUSSION	12
1. Atomized Powder	12
2. Consolidated Material	14
3. Heat-Treated Material	16
CONCLUSIONS	18
PART II: P/M Rex 25 TOOL STEEL	20
RESULTS AND OBSERVATIONS	21
1. Atomized Powder	21
2. Annealed Powder	21
3. Consolidated Material	22
4. Heat-Treated Material	23

DISCUSSION	24
1. Atomized Powder	24
2. Annealed Powder	25
3. Consolidated Material	26
4. Heat-Treated Material	27
CONCLUSIONS	28
REFERENCES	31
TABLES	32
FIGURES	35
APPENDIX: CARBIDE SIZE DISTRIBUTIONS IN P/M T15	77
PRESENTATIONS, REPORTS AND PUBLICATIONS	
DISTRIBUTION LIST	

ABSTRACT

A detailed microstructural examination has been made of T15 and Rex 25 high speed tool steels processed from rapidly solidified powders. Gas atomized powders were screened into selected size fractions, hot isostatically pressed to full density and heat-treated. Two HIPing temperatures, two austenitizing temperatures and three tempering temperatures were included in the study. Atomized and consolidated materials were characterized by means of optical and electron microscopy, x-ray diffraction and hardness. Both cellular and dendritic structures are present in the atomized powders depending on particle size, with MC carbides present primarily at cell boundaries. The partitioning of alloying elements in the cell structure decreases with decreasing particle size. Independent of prior particle size fraction, the carbide size distribution after HIPing is skewed to larger carbide sizes with increasing HIPing temperature, but with no significant change in volume fraction of carbides. At a given HIPing temperature, the carbide size distribution for MC and M_6C carbides is dependent on prior particle size fraction; it is broader for the coarser size fractions. After heat-treatment, the constituents present are tempered martensite, MC and M_6C carbides, independent of prior particle size fraction and HIPing temperature. In T15, the size distribution of MC carbides after tempering is relatively independent of HIPing temperature. In contrast, there is a significant increase in the size spread of M_6C with increase in HIPing temperature; this is accompanied by a skewing of the M_6C carbide size distribution to coarser carbide sizes. Microstructures are analyzed in terms of particle cooling rate and structural stability during consolidation.

INTRODUCTION

To optimize mechanical properties and performance in high speed tool steels, it is necessary to control the carbide size and carbide distribution. While heat-treatment will affect the final microstructure, the influence of the solidification process per se is extremely important. Because of the complex solidification sequence in high speed steels, alloy segregation can occur. The long freezing range leads to dendritic coring with attendant coarse primary carbide networks in the microstructure of conventionally cast material. Since the carbide distribution is determined primarily by the extent of alloy segregation during solidification, it is necessary to utilize high cooling rates to minimize this segregation.

Significant refinements in the microstructure of a high speed tool steel is possible by means of powder metallurgy (P/M) processing since each powder particle is a mini-ingot and the extent of segregation will be limited by the maximum powder particle dimensions. Coupled with increased alloying flexibility and fine-scale microstructures, this had led to the development of commercially viable P/M processes for a wide range of high speed tool steel compositions (1-4). These processes utilize gas atomized powder which is consolidated by hot isostatic pressing. Compared to conventional ingot metallurgy (I/M) high speed tool steels, the commercial P/M materials exhibit superior microstructures with respect to austenite grain size, and the fineness and homogeneity of carbide dispersions. These features have been shown to result in improved hot workability, grindability, toughness, tool life and out-of-roundness distortion (1,3,4-6).

Commercial P/M tool steels are consolidated from gas atomized powder covering a broad particle size range, typically up to 1200 μm . Thus, a wide range of cooling rates is inherent in the powders prior to consolidation,

with the finer powder particle sizes falling in the rapid solidification regime. Since the structure of high-speed steel is extremely sensitive to cooling rate (7-9), it is clear that a spectrum of microstructures is present in commercial high speed tool steel powders prior to consolidation. Further, the extent to which the structures in the atomized powder are retained during hot isostatic pressing will depend on prior particle cooling rate and consolidation temperature.

The overall goal of the present study is to: (i) determine and understand the effect of cooling rate, including the rapid solidification regime, on powder particle microstructures, (ii) evaluate microstructural changes accompanying hot isostatic pressing of the powder, and (iii) establish and interpret processing-microstructure-property/performance relations, as a function of prior powder particle size. Two high speed steel compositions were included, T15 and Rex 25; the latter is a cobalt-free version of T15 with similar heat-treatment response, mechanical properties and tool performance. The atomized powders were screened into narrow size ranges in order to obtain the required spectrum of cooling rates.

EXPERIMENTAL PROCEDURE

1. Powder Atomization

Heats of T15 and Rex 25 high speed tool steels have been atomized at the Materials Research Center, Crucible Inc. The alloy charge was melted in a nitrogen atmosphere and nitrogen gas atomized. Powder was collected in liquid nitrogen at the base of the atomizing unit.

Chemical analysis of the two batches of powder are summarized in Table I. Typical compositions for corresponding commercial alloy powders and the ingot metallurgy counterpart are included in the table for purposes of comparison. The levels of the alloying elements in the powders atomized

for this research program are similar to those in the commercial Crucible particulate metallurgy T15 and Rex 25 tool steels. Powders evaluated were within the size range $\leq 37 \mu\text{m}$ to $2000 \mu\text{m}$.

2. Powder Characterization

T15 and Rex 25 powders of selected size fraction were characterized in the as-atomized condition and after annealing at 1125°C (T15) and 1175°C (Rex 25) for 30 minutes. Powders were characterized in terms of their microstructure, microhardness and constituent phases, utilizing scanning electron microscopy, transmission electron microscopy of two-stage replicas, and x-ray diffraction (10).

3. Powder Consolidation

Small bar samples (1" x 6" (25.4 mm x 152.4 mm)) of each alloy from specific size ranges (10) were hot outgassed, sealed and hot-isostatically pressed (HIPed) at 1130°C or 1195°C . The former is the temperature used by Crucible Inc. for commercial high-speed tool steels. The lower temperature was used as a possible means for grain size control during densification in the HIP cycle. This yielded a matrix of eight samples for each composition, i.e. four size fraction and two HIP temperatures.

The purpose of the small samples was to verify that HIP consolidation had brought about complete densification. Subsequently, larger compacts (4" (101.6 mm) diameter x 11" (279.4 mm) length) were produced by HIPing the balance of the powder. Each of the small bar samples was cut in half for purposes of microstructural characterization and preliminary examination of heat-treatment response. The system of coding used is given in Table II.

4. Characterization of HIPed Material

Each of the eight T15 and eight Rex 25 samples was mounted, polished and etched using Kalling's reagent. Two stage carbon replicas of the samples were prepared and examined by TEM. Rockwell hardness measurements were carried out on each of the sixteen samples.

X-ray diffraction patterns were obtained using diffractometry and the Debye-Scherrer technique. The former was used essentially to evaluate the matrix phase. The Debye-Scherrer method was used to identify the carbides. To this end, isolation of the carbides from the consolidated material was achieved by electrolytic extraction. This procedure was followed for each of the sixteen compacts (11).

Eight compacts (4 from each composition) corresponding to the coarsest and finest size fractions and the two HIPing temperatures were polished, etched and examined by SEM.

Selective etching techniques were used to aid in unambiguous determination of the carbides present in the HIPed samples. M_6C type carbides are selectively stain-etched using a $KMnO_4 + NaOH$ solution. MC carbides are electrolytically etched using a chromic acid solution. EDAX spectra of MC and M_6C carbides were obtained for each of the eight HIPed compacts. EDAX spectra of the matrix were obtained from samples etched with Kalling's reagent.

Volume fractions of MC and M_6C carbides, and accompanying size distributions, were obtained from appropriately etched samples by means of quantitative metallography utilizing a Texture Analysis System (TAS). The TAS is an image analyzer which optically scans the sample and provides data accumulated over 'n' fields of view. 'n' was set at 25 fields in the present study.

5. Heat-Treatment

A study of the heat treatment response of material cut from the small HIP bars (T15 and REx 25) was initiated. Two austenitizing temperatures 1176°C and 1226°C were selected. Samples were heated to the austenitizing temperature and held at temperature for four minutes before oil-quenching. Three tempering temperatures were used (538°C, 552°C and 655°C). A coding system for the various processing treatments is given in Table II.

6. Characterization of Heat-Treated Material

The heat treatment schedule yielded a matrix of sixty-four samples (8 HIPed samples x 2 austenitizing temperatures x 3 tempering temperature + 8 HIPed samples x 2 austenitizing temperatures) for T15 and Rex 25, each of which had been subjected to a specific heat treating sequence. Samples from this matrix were characterized in terms of microstructure, hardness and constituent phases. 32 samples per composition (coarse and fine size fraction x 2 HIP temperatures x 2 austenitizing temperatures x 3 temperatures + 8 samples in the austenitized and quenched condition) were characterized quantitatively. The volume fraction of MC and M₆C carbides, as well as the size distribution of each type of carbide was determined for each of the thirty two samples using the techniques outlined previously.

PART I: P/M T15 TOOL STEEL

RESULTS AND OBSERVATIONS

1. Atomized Powder:

a) Scanning Electron Microscopy

It has previously been shown (10) that over the size range examined, the powder particles were essentially spherical in shape with small satellites attached. Also, Debye-Scherrer diffraction patterns of extracted carbides from each size fraction were consistent with the presence of cubic and hexagonal MC carbides (10).

Subsequently, polished and etched powder cross-sections from three size fractions (550-700 μm , 110-130 μm , <37 μm) have been examined by high resolution SEM. Representative micrographs are shown in Figures 2, 3, 4, 5, 6 and 7.

In the 550-700 μm size fraction, there is a cellular structure in which the cells are outlined by a discontinuous network of carbides, Figure 2. The rectangular area outlined in Figure 2 is shown at a higher magnification in Figure 3; needles of martensite are visible in the matrix. Figures 4 and 5 show the microstructure of the 110-130 μm size fraction. A cellular structure is again evident but the cell size is much smaller and the carbide network more-continuous than in the coarser size fraction (cf. Figures 2 and 4). In several locations, particularly at the junction of three cells, the structure has a lamellar morphology characteristic of eutectic solidification, Figures 3 and 5.

The microstructure of the <37 μm screen size powder is illustrated in Figures 6 and 7. In some particles a predominantly dendritic mode of solidification is evident (Figure 6) while in others, the cellular structure characteristic of the coarser size fractions is seen, Figure 7. In the latter, the cell size is similar to that in the 110-130 μm size

fraction. A cellular-like morphology is seen in the lower right hand corner of Figure 6; elsewhere in this particle the structure is dendritic.

b) Element Mapping

Figures 8(a-f) show element mapping for the 550-700 μm size fraction. The elements vanadium, tungsten and chromium are partitioned between the cell walls and the cell interior, the extent of partitioning increasing in the order chromium, tungsten and vanadium (Figures 8b,c,d). In addition, it is seen that the distribution of these elements in the cell wall is not uniform. In contrast, iron and cobalt are depleted in the cell boundaries, with the depletion of iron being more pronounced than that of cobalt.*

A comparison of Figures 8(b-d) and 9(b-d) shows that the extent of segregation of the chromium, tungsten and vanadium at cell boundaries is less in the finer (<37 μm) powder size fraction. Also, the distribution of iron and cobalt between cell walls and cell interiors is more uniform in the -37 μm size fraction; cf. Figures 8e,f and 9e,f.

2. Consolidated Material

a) Scanning Electron Microscopy

Micrographs (SEM) of polished and etched samples corresponding to the coarsest (840-250 μm) and finest (<44 μm) size fractions are shown in Figures 10 through 13. The carbides are coarser following HIPing at the higher temperature (H2). For a given HIPing temperature (H1 or H2), the carbide size is essentially independent of prior particle size fraction. The matrix consists of α -ferrite and three carbides are present, namely

*The cobalt K_{α} energy level overlaps that of iron K_{β} ; thus the true partitioning of cobalt between the cell walls and cell interior will be even less than that inferred from Figure 8f.

MC, M_6C and $M_{23}C_6$.

b) EDAX

An EDAX spectrum of material HIPed from the 250-840 μ m size fraction at H1 shows that the matrix is iron-rich with small amounts of tungsten and vanadium present, Figure 14. The level of chromium in the matrix is higher than that of tungsten and vanadium. A representative EDAX spectrum for the MC carbides in the 250-840 μ m sample HIPed at H1 is given in Figure 15. This carbide is vanadium-rich, as expected, but there are significant amounts of iron, tungsten and chromium present. A similar spectrum for the M_6C carbides shows that these carbides are iron-rich but with tungsten, vanadium, and to a lesser extent chromium, present, Figure 16.

The EDAX spectrum for the matrix of the material HIPed at H2 from the 250-840 μ m size powder is shown in Figure 17. The matrix is iron-rich with chromium and cobalt, and to a lesser extent tungsten and vanadium, in solution. In comparison to the MC carbides in the material HIPed at H1, there is a higher level of iron present, cf. Figures 15 and 18. The M_6C carbides contain more tungsten after HIPing at H2 than at H1, cf. Figures 16 and 19.

An EDAX spectrum of the MC carbides after HIPing the <44 μ m size powder at H1 is shown in Figure 20. This carbide dissolves significant amounts of iron and tungsten, and to a lesser extent chromium. As expected, the MC carbide is vanadium-rich. The M_6C carbide is iron-rich but contains small amounts of tungsten, vanadium and chromium, Figure 21. In the <44 μ m size powder HIPed at H2, the MC carbides are no longer iron-rich, Figure 22; however, tungsten remains at about the same level as in MC carbides following HIPing at H1. The ratio of iron to vanadium is significantly reduced after HIPing at the higher of the two temperatures, cf. Figures 20 and 22.

An EDAX spectrum for M_6C carbides, after HIPing the $<44 \mu m$ size powder at H2, is shown in Figure 23. Comparing Figures 21 and 23, it is seen that increasing the HIPing temperature from H1 to H2 changes the composition of M_6C from an iron-rich carbide containing tungsten to a tungsten-rich carbide which contains iron.

c) Quantitative Metallography

Carbide volume fractions, as a function of particle size fraction and HIPing temperature, are compared in Figure 24. For both carbides, the volume fraction is not a sensitive function of size fraction or HIPing temperature.* Carbide size distributions (MC, M_6C , H1, H2 coarse and fine size fractions) are given in Figures A1 through A8.** The size distribution is skewed to higher carbide sizes with an increase in HIPing temperature, cf. Figures A1 and A2, A3 and A4, A5 and A6, A7 and A8. The extent of the skew is greater for the M_6C carbides than for the MC carbides. The carbide size distribution for M_6C is dependent on the prior particle size fraction, for a given HIPing temperature; it is broader for the coarser size fraction. To a lesser extent, the same trend in size distribution exists for the MC carbides. No selective etching technique exists for the unambiguous and quantitative identification of $M_{23}C_6$; this carbide precipitates during the HIPing cycle.

3. Heat-Treated Material

a) Scanning Electron Microscopy

Micrographs of the T15 P/M tool steel after austenitizing,

*The variations in volume fraction of MC and M_6C with HIPing temperature or screen fraction are less than the limits of uncertainty defined by the standard deviations.

**All size distribution data are included in the Appendix to this report.

and austenitizing plus tempering, are shown in Figures 25 through 35. After quenching from the austenitizing temperature, martensite is visible in material from both the coarse and fine size fractions, Figures 25, 28 and 31. After tempering, the matrix is characteristic of tempered martensite, cf. Figures 28 and 29.

b) X-Ray Diffraction

Analysis of diffraction traces from extracted carbides confirms the presence of MC and M_6C at each stage of heat-treatment. Some $M_{23}C_6$ remains after austenitizing at A1, but all this carbide is dissolved at A2. $M_{23}C_6$ does not reprecipitate during tempering. No new carbide-types have been identified after heat-treatment.

c) Quantitative Metallography

Carbide volume fractions of MC after HIPing (H1 or H2) and HIPing plus austenitizing (A1 or A2) are compared in Figure 36. A similar comparison for M_6C carbides is given in Figure 37. It can be seen that MC carbides go into solution during austenitizing; the volume fraction of MC remaining decreases with increasing austenitizing temperature. A similar response is observed for the M_6C carbides, Figure 37; the effect is more pronounced than for MC carbides. After austenitizing at A1 and quenching, the volume fraction of M_6C is in the range 6.5-7.0%. The corresponding volume fraction following austenitizing at A2 and quenching is 5.0-5.5%.

HIPing temperature influences the volume fraction of MC carbides present after austenitizing and quenching. For HIPing at H1 and austenitizing at A2, the volume fraction is in the range 12.0 to 13.0%. In contrast, a combination of HIPing at H2 and austenitizing at A2 results in a carbide volume fraction of ~8.75%.

Volume fractions of MC and M_6C carbides, as a function of tempering temperature, are compared in Figures 38 through 43. Limits of uncertainty are defined by the standard deviation. The volume fraction of M_6C carbides increases from within the range 4.5 to 7% in the as-quenched condition to within the range 8-10% after tempering. The volume fraction of M_6C increases with increasing tempering temperature. A similar, but not as pronounced effect is observed for the MC carbides; in this case, the volume fraction first increases and then stays relatively constant with further increases in tempering temperature.

Carbide size distributions for MC and M_6C , as a function of prior particle size fraction, HIPing temperature and heat-treatment, are compared in Figures A9 through A54. For M_6C carbides, the size distribution is skewed to the right with increasing tempering temperature, irrespective of prior particle size fraction or HIPing temperature. This trend is not as evident for the MC carbides.

Irrespective of heat-treatment conditions, 60 to 65% of the total MC carbide content reflects carbides in the size range 0.6 to 1.2 μm . The size distribution for M_6C carbides depends on the HIPing temperature. For coarse and fine size fractions, HIPing at H2 results in 45-50% of the total M_6C carbide content having sizes in the range 1.2-1.8 μm , irrespective of austenitizing or tempering temperature. After HIPing at H1, the corresponding ranges are 60-65% and 0.6-1.2 μm .

DISCUSSION

1. Atomized Powder

In gas atomization, a stream of liquid metal is broken-up by means of a high pressure gas stream. The resulting liquid droplets spheroidize in

free fall before solidification due to surface tension. Particle collisions can occur before and/or after solidification (9) and this is responsible for satellite formation. Cubic MC and hexagonal γ -MC carbides have been identified in all the powder size fractions examined. γ -MC is not present in the HIPed material. This implies that γ -MC is not an equilibrium phase but is present in the atomized powder as a result of the high cooling rate. On annealing of the powder or during the HIPing cycle, γ -MC goes into solution and/or reverts to the cubic form. From Figures 2 and 4, it appears that austenite nucleates first on solidification. The solute-rich liquid solidifies later at the γ cell boundaries and there is evidence for eutectic decomposition, e.g. Figures 3 and 5. The latter is substantiated by the elemental mapping results (Figures 8a-8f) in which segregation of tungsten, chromium and vanadium was confirmed at the cell walls, with an accompanying depletion of iron.

With increasing rates of particle cooling (i.e. smaller particle size), higher degrees of undercooling result in a higher nucleation rate of austenite, and hence a smaller cell size, Figures 4 and 5. The transition from a cellular to a dendritic mode of solidification with decreasing particle size (cf. Figure 4 and Figure 6) can be explained in terms of the cooling rate T , the thermal gradient G , and the solid/liquid interface velocity, R . Similar observations have been reported by Smugeresky (12), Levi and Mehrabian (13) have pointed out that as the droplet size decreases, the time for the start and completion of solidification decreases, the interface velocity at equivalent fractions solidified increases, and the G to R ratio decreases. Consequently as the droplet size and the G to R ratio decreases, a change from a cellular to a dendritic structure can be expected.

The presence of a cellular structure in some of the particles in the <37 μm screen fraction is possibly due to the fact that some of these fine particles spend a longer time in the turbulent gas zone during atomization; in consequence, they experience a decrease in the extent of undercooling. As expected, elemental segregation is less in the fine powder than in the coarser size fractions.

Needles of martensite are visible in the coarsest size fraction but are not evident in the finer powder particles. This can be explained in terms of the high degree of supersaturation of the austenite associated with higher cooling rates in the <37 μm particles (9).

2. Consolidated Material

After HIPing, MC, M_6C and M_{23}C_6 carbides are present. This is to be expected since the slow cooling inherent in the HIP cycle leaves the consolidated material essentially in the annealed condition. These carbides are known to be present after annealing (11).

A comparison of Figures 10, 11, 12 and 13 shows that for a particular HIPing temperature, the carbides are approximately the same size. However, the carbides are coarser following HIPing at the higher temperature.

EDAX of the matrix in Figures 14 and 17 for the 250-840 μm screen fraction, consolidated at H1 and H2 respectively, shows the matrix to be essentially iron-rich with chromium and cobalt in solution. Limited amounts of vanadium and tungsten are also present in solution in the matrix. For both the coarse and fine screen fractions HIPed at H1, the M_6C carbides are iron-rich with a significant amount of tungsten present. However, after HIPing at H2, the M_6C carbides are rich in tungsten with some iron still present. This behavior can be attributed to the slower rate of diffusion of tungsten as well as to the variation of the solubility of iron and

tungsten in M_6C with temperature. MC carbides are vanadium-rich in both the coarse and the fine screen fractions HIPed at H1 or H2. It is known (14) that these carbides can dissolve only limited amounts of iron and tungsten. However, Figures 18 and 20 show these MC carbides to be iron-rich. This behavior is possibly due to the fact that the high energy beams used in the analysis pick up iron from the matrix around and below the small ($\sim 1 \mu\text{m}$ dia.) MC carbide particles.

No appreciable dependence of volume fraction of MC and M_6C carbides with HIPing temperature and/or prior powder particle size exists; Figure 24. This implies that the equilibrium level of solubility is achieved.

A close examination of the size distribution for M_6C carbides shows that for a given HIPing temperature (H1 or H2), the 250-840 μm powder size fraction exhibits a wider spread of carbide sizes than does the $\leq 44 \mu\text{m}$ powder screen; cf. Figures A5 with A7 and A6 with A8. M_6C carbides are not present in the atomized powder. Assuming that supersaturation of the matrix with respect to tungsten is similar for the two size fractions, then on heating to the HIPing temperature (H1 or H2), this supersaturation is relieved by the precipitation of tungsten-rich M_6C carbides. M_6C carbides can precipitate within the cells and more readily at the cell walls. With decreasing particle size, particle surface area per unit volume increases and cell size decreases. Thus, more nucleation sites are available in the finer size fraction; this results in a narrow spread in carbide sizes in the fine size fraction compared to the coarser fraction. At both HIPing temperatures, significant dissolution of the M_6C carbides occurs. The rate of dissolution is dependent on intercarbide distance, carbide size, carbide size distribution and carbide stability. Hence, M_6C carbides in the coarser size fraction will dissolve at a faster rate than those in the finer size fraction. During cooling from H1 or H2 reprecipitation of the M_6C

carbides occurs on existing carbides and this further enhances the spread in size distribution.

MC carbides are present in the as-atomized powders. If it is assumed that the volume fraction of MC in the powder decreases with decreasing particle size (i.e. increasing cooling rate), then the degree of supersaturation of vanadium in the matrix will increase with decreasing particle size. This factor is superimposed on those discussed above for M_6C carbides and favors a broader spread in carbide sizes. However, MC carbides are extremely stable and on heating to H1 or H2 are readily nucleated with a high nucleation rate in both coarse and fine powder fractions. In addition, once formed the MC carbides are very stable and resist coarsening. These latter two factors preclude a broadening of the carbide size distribution for MC.

3. Heat-Treated Material

The presence of traces of $M_{23}C_6$ in the consolidated tool steel after austenitizing at A1 confirms that this temperature is not high enough to dissolve all this type of carbide which was present after HIPing. Therefore, maximum strengthening of the matrix requires a higher austenitizing temperature, e.g. A2 at which all the $M_{23}C_6$ is dissolved.

From Figure 36 it can be seen that the MC carbides go into solution on austenitizing and the volume of MC carbides going into solution increases with increasing austenitizing temperature. Further, for similar size fractions, HIPing temperature influences the volume fraction of MC carbides that go into solution on austenitizing. Samples HIPed at H1 and austenitized at A2 exhibit a higher volume fraction of MC carbides than those HIPed at H2 and austenitized at A2, Figure 36. A possible interpretation of this behavior is that for similar volume fractions of MC carbides, the material HIPed at H2, exhibits a size distribution skewed to the coarser side. This in turn

implies a longer intercarbide distance in the sample HIPed at H2. In this sample the presence of coarse and fine carbides, together with a larger intercarbide distance, causes accelerated dissolution of the fine carbides. In the sample HIPed at H1 the size distribution is more narrow and therefore a correspondingly lower, more uniform rate of dissolution. This feature is not observed for the M_6C carbides which are not as stable as the MC carbides, Figure 37. In comparison to MC, a larger fraction of M_6C dissolves on austenitizing. Here too, the amount of M_6C carbides that go into solution, increases with increasing austenitizing temperature. The volume fraction of M_6C carbides present after austenitizing and quenching is not a sensitive function of the HIPing temperature.

Volume fraction of MC and M_6C carbides, as a function of tempering temperature, are shown in Figures 38 to 43. On tempering, the excess carbon precipitates from the supersaturated matrix in the form of MC or M_6C carbides. The volume fraction of M_6C increase with increasing tempering temperature due to nucleation and growth.

Taking account of the limits of uncertainty (\pm standard deviation), in most cases a small increase in the volume fraction of MC carbides is observed as a function of tempering temperature. This reflects the high degree of stability of the MC carbides compared to M_6C .

Figures A9 through A54 show the size distribution of MC and M_6C carbides as a function of prior particle screen fraction, HIPing temperature and the heat-treatment sequence. With increase in tempering temperature the size distribution of M_6C carbides skews to the coarser side. This is due to nucleation and growth. This effect is not so pronounced for the MC carbides which are more stable. Although, the size distribution of MC carbides in the heat-treated samples is relatively independent of the HIPing temperature, the size distribution of M_6C is not. No matter what

heat treatment was used. Samples HIPed at H1 have about 60-65% by volume of M_6C carbides in the 0.6-1.2 μm range. Sample HIPed at H2 and subsequently heat-treated have 45-50% of the total M_6C volume fraction lying in the size range 1.2-1.8 μm . This behavior emphasizes the importance of the HIPing temperature as a processing parameter and its effect on the microstructure of the heat treated material.

CONCLUSIONS

1. For powder particle sizes below 37 μm , both cellular and dendritic microstructures are observed. In some particles, both morphologies are present. These different microstructures reflect differences in the G/R ratio with particle size.
2. The fraction of martensite decreases with decreasing particle size and is due to the increase in the level of alloying elements and carbon in solid solution in the smaller powder particles.
3. In particles exhibiting a cell structure, primary austenite solidifies first, followed by eutectic decomposition with attendant carbide formation at cell boundaries.
4. Cr, W and V are partitioned between cell walls and cell interiors in the powder. The extent of partitioning decreases with decreasing particle size.
5. Cubic and hexagonal MC are present in the atomized powder; the hexagonal form is shown to be metastable.
6. In the HIPed condition, microstructures consist of a matrix of α -ferrite and isolated carbides of MC, M_6C and $M_{23}C_6$.

7. Independent of prior particle size fraction, the carbide size distribution is skewed to larger carbide sizes with an increase in HIPing temperature, but with no significant change in volume fraction of carbides. Thus, by using lower HIPing temperatures, it is possible to achieve a finer distribution of carbides without a decrease in their volume fraction.
8. At a given HIPing temperature, the carbide size distribution for MC and M_6C carbides is dependent on prior particle size fraction; it is broader for the coarser size fractions.
9. The compositions of MC and M_6C carbides are a sensitive function of HIPing temperature, independent of prior particle size fraction.
10. After heat-treatment, the constituents present are tempered martensite, MC and M_6C carbides, independent of prior particle size fraction and HIPing temperature. Traces of $M_{23}C_6$ are also present if the austenitizing temperature is not sufficiently high.
11. The volume fractions of both MC and M_6C increase with increasing tempering temperature, independent of HIPing temperature and prior particle size fraction. The effect is greater for M_6C than for MC.
12. The size distribution of MC and M_6C carbides are skewed to coarser carbide sizes with an increase in tempering temperature; the effect is more pronounced for M_6C than MC.
13. The size distribution of MC carbides in the tempered material is relatively independent of HIPing temperature. In contrast, there is a significant increase in the size spread of M_6C with increase in HIPing temperature; this is accompanied by a skewing of the M_6C carbide size distribution to coarser carbide sizes.

PART II: P/M REX 25 TOOL STEEL

RESULTS AND OBSERVATIONS

1. Atomized Powder

Four size fractions of atomized powder were studied, namely $\leq 37 \mu\text{m}$, 62-74 μm , 350-420 μm and 840-2000 μm . Representative micrographs (SEM) from each size fraction are compared in Figures 44 and 45. Two types of structure are observed for the finest powder size fraction, namely dendritic (Figure 44(a)) and cellular (Figure 44(b)). In the other size fractions, a cellular microstructure is evident with carbides precipitated predominantly at cell boundaries, Figure 45. The mean cell size decreases with decreasing particle size. Cells in the 62-74 μm size fraction are well-defined in some regions, but faint in others, Figure 45(a).

To-date, Debye-Scherrer x-ray analysis of as-atomized powders has confirmed the presence of cubic and hexagonal MC carbides. Lattice parameters are currently being determined from extracted carbides.

A plot of microhardness as a function of particle size is shown in Figure 46. After an initial drop, hardness increases and then levels out with increasing particle size.

2. Annealed Powder

Atomized powders of each of the four size fractions were held at a temperature of 1175°C (2150°F) for 30 minutes, and furnace cooled. The annealed powders were studied under the transmission electron microscope by examining two-stage carbon replicas prepared from mounted, polished and etched samples. Representative TEM micrographs of the coarse and fine size fractions are shown in Figures 47(a) and 47(b). There is no appreciable difference in the carbide sizes in these two size fractions. Carbides exist as individual particles; the interconnected networks, as well as the

matrix structure, observed in the atomized powders (Figures 44 and 45), are no longer present.

X-ray analysis of extracted carbides is presently in progress. To date, the presence of two excess phases have been determined, viz. cubic M_6C and cubic MC. The matrix consists of α -ferrite. The change in α -ferrite lattice parameter with powder particle size is shown in Figure 48.

Results of microhardness measurements, as a function of particle size, are shown in Figure 49. Although hardness values decrease by approximately 130-160 KHN as compared to the as-atomized powder (Figure 46), the general shape of the curve is the same.

3. Consolidated Material

Powders from four size fractions ($\leq 44 \mu m$, 44-100 μm , 250-840 μm , $\leq 840 \mu m$) were HIPed at H1 or H2. Representative micrographs of the coarsest and finest size fractions are illustrated in Figures 50 and 51, respectively. Samples HIPed at the higher temperature (H2) show coarser carbides for both size fractions. However, there is no visible difference in carbide size, for size fractions HIPed at the same temperature. The micrographs show the presence of predominantly three types of carbides: (i) blocky, massive type, which are mostly interconnected; (ii) small, globular carbides; (iii) fine, needle-like carbides.

The matrix is α -ferrite with MC and M_6C carbides present. Lattice parameters of each phase are summarized in Table . There is no significant variation in lattice parameter with particle size fraction or HIPing temperature.

EDAX spectra, showing typical compositions of MC and M_6C carbides are illustrated in Figures 52(a) and 52(b), respectively. The MC carbides are vanadium rich, whereas M_6C carbides are rich in tungsten, iron and molybdenum.

EDAX shows that the darker carbides present in Figures 50 and 51 are MC, whereas the lighter ones are of the M_6C -type. These micrographs show that MC carbides are usually sandwiched between two or more M_6C carbides.

Size distribution for the M_6C carbide are illustrated in Figure 53. For a given HIPing temperature, the finest size fraction ($\leq 44 \mu\text{m}$) has a larger volume fraction of fine carbides as compared to the coarse, 250-840 μm size fraction. Total volume fraction of carbides in both size fractions is essentially the same. Although an increase in HIPing temperature results in the size distribution being skewed to larger sizes, the total volume fraction of carbides remains relatively unchanged. Similar results are obtained for MC carbides as shown in Figure 54. However, the change in size distribution, with size fraction at a particular HIPing temperature is not as pronounced as for the M_6C carbides.

4. Heat-Treated Material

Microstructures obtained after HIPing the 250-840 μm size fraction at H1 and austenitizing at A1, or tempering at T1 or T3, are illustrated in Figure 55. Tempering results in an increase in carbide content, but the increase in carbide volume fraction between T1 and T3 is marginal. Martensite is present after quenching (Figure 56(a)) and is replaced by a fine network of needle-like carbides on tempering, Figure 56(b).

The effect of the higher austenitizing temperature (A2) on microstructure is shown in Figure 57. Carbide volume fraction is highest for the highest tempering temperature (T3) and smallest in the as-quenched condition (H1 + A2). A comparison of Figures 55(a) and 57(a) shows that the volume fraction of carbide in the as-quenched condition decreases with increasing temperature of austenitization.

For a given HIPing temperature, prior particle size fraction has no appreciable effect on microstructure after heat-treatment, cf. Figures 55 and 58. Prior austenite grain boundaries are visible in the as-quenched material, Figure 58(a). These grains coarsen at the higher austenitizing temperature, Figure 58(d).

The effect of HIPing temperature on carbide size after heat-treatment is seen from a comparison of Figures 55(a) and 57(a) with Figures 59(a) and 59(b). The higher HIPing temperature results in coarser primary carbides.

Hardness curves of the heat-treated samples as a function of tempering temperature are illustrated in Figure 60. Samples austenitized at the lower temperature (A1) show a continuous drop in hardness with increasing tempering temperatures, whereas, those austenitized at the higher temperature (A2), peak at the lowest tempering temperature (T1). A comparison of Figures 60(a) and 60(b) shows no appreciable change in hardness with size fraction, for the same HIPing temperature. Figure 61 illustrates the effect of HIPing temperature on hardness. A higher HIPing temperature results in lower hardness values.

DISCUSSION

1. Atomized Powders

The origins of both dendritic and cellular structures in powder particles from the finest size fraction have been discussed in Part I of this report for T15 tool steels. Similar considerations apply to the Rex 25 powder. The presence of these two forms of microstructure may, in part, be responsible for the scatter in microhardness data, Figure 46. The small powder sizes mandated use of a small indentation load and this is also expected to contribute to scatter.

Decreasing cell size with decreasing particle size is the result of increasing cooling rates. The latter also promote a greater degree of solutionizing of alloying elements. The matrix in the powder particles is expected to consist of retained austenite, martensite and possibly δ -ferrite, depending on cooling rate. The last liquid to freeze, which is rich in alloying elements and carbon, is responsible for the precipitation of carbides along cell boundaries. Slower cooling rates decrease the level of alloying elements and carbon in solution in the matrix, with a necessary increase in the size and volume fraction of carbides. The carbide network observed in the coarsest size fraction (Figure 45(c)) is similar to the "fishbone" shaped carbides described by Bunghardt et al. (15) in conventional tool steels. These carbides were identified as M_6C , and the globular carbides as MC (15). In the present study on Rex 25, the identity of the carbides present has yet to be established. Uneven etching of the cellular structure is attributed to segregation of alloying elements within the powder particle.

2. Annealed Powder

The matrix structure and interconnected carbide networks present in as-atomized powder are substantially modified on annealing. Slow cooling from the annealing temperature results in a depletion of alloying elements and carbon from the matrix, leading to the precipitation of individual carbides and the formation of α -ferrite. The decrease in hardness of the powder after annealing is the result of (i) a decrease in solid solution strengthening, (ii) increase in carbide size, and (iii) a change in the matrix structure from martensite (or δ -ferrite) to α -ferrite.

The increase in the lattice parameter of the matrix of the annealed powder, compared to pure α -ferrite ($a_0 = 2.866 \text{ \AA}$), is attributed to the presence of the metallic alloying elements in solid solution. Each of these elements has an atomic radius greater than that of iron.

3. Consolidated Material

After HIPing, microstructures are similar to those observed in the annealed powders. It is clear that increasing the HIPing temperature results in a skewing of the carbide size distribution to larger sizes. Carbide coarsening is enhanced at H2 compared to H1 because of the increased diffusion rates of the alloying elements.

An explanation of the broader size distribution with increasing size fraction (Figures 53 and 54) has been given in Part I for T15. A similar argument should apply for Rex 25.

The relatively high volume fraction ($V_f \approx 0.3$) of M_6C carbides results in some clustering of the fine carbides. Thus, it was not possible to resolve each carbide as a separate entity; in most cases, the clusters were recorded as a single, large M_6C carbide. This accounts for the relatively high volume fraction of carbides, with an equivalent diameter greater than 2.4 \mu m (Figure 53).

Lattice parameters of the α -ferrite, M_6C and MC (Table III) do not show any significant variation with size fraction or HIPing temperature. Matrix lattice parameters are similar to those observed for annealed powders (Figure 48). The prototype of MC carbide is V_4C_3 . As shown by the EDAX spectrum in Figure 52(b), this carbide is rich in vanadium. The presence of tungsten and molybdenum is responsible for the increase in the MC lattice parameter as compared to that of pure V_4C_3 ($a_0 = 4.16 \text{ \AA}$). Pure M_6C , which varies from $Fe_3W_3C - Fe_4W_2C$ or $Fe_3Mo_3C - Fe_4Mo_2C$, has an average lattice parameter of 11.04 \AA . Figure 52(a) confirms the large tungsten, iron and

molybdenum content in these carbides. Replacement of iron by alloying elements results in the increased lattice parameter observed for M_6C . Variations of a_0 values obtained in Table III are due to experimental errors.

The absence of $M_{23}C_6$ may be attributed to its weak scattering of x-rays, and to the fact that for $M_{23}C_6$ the stronger diffraction lines lie close to those of M_6C , which is a strong scatterer of x-rays (11). A second possibility is that the relatively low amount of chromium (3 wt %) present in the steel has resulted in too small a fraction of $M_{23}C_6$ to be detected.

4. Heat-treated Material

Carbides dissolve during heating to the austenitizing temperature and are precluded from reprecipitating due to the rapid quench. On tempering, the alloying elements and carbon in solution precipitate out as carbides. Tempering at a higher temperature results in only a marginal increase in carbide volume fraction.

The lower total carbide volume fraction existing at the higher austenitizing temperature reflects the higher level of solubility of the alloying elements and carbon at this temperature (Figures 58(a) and 58(d)). A lower volume fraction of carbides allows for an increase in grain size at the higher austenitizing temperature. Since the number of nucleating sites is lower in the coarse grained material, this may also be a contributing factor to the decrease in carbide volume fraction with increasing austenitizing temperature.

The above discussion is based solely on the examination of micrographs (SEM). A tentative identification of carbides has been carried out by means of selective etching and carbide sizes, and size distributions determined by qualitative metallography. It remains to unambiguously identify the carbides by x-ray analysis.

Hardness as a function of tempering temperature is dependent on (i) solid solution strengthening, (ii) carbide precipitation, and (iii) carbide coarsening. Austenitizing temperature does not appear to have any significant effect on the hardness of the as-quenched material (Figures 60 and 61). This implies that the increase in solid solution hardening due to a higher austenitizing temperature has been nullified by, (i) a coarser austenite grain size, (ii) a lower volume fraction of martensite in the matrix, and (iii) a decreased amount of carbide precipitation.

The decrease in hardness with increasing tempering temperature for material austenitized at A1 (Figures 60 and 61) is due to carbide coarsening. The lower austenitizing temperature also results in decreased solutionizing of alloying elements, which decreases the amount of secondary carbide precipitation on subsequent tempering. Material austenitized at A2 has a greater amount of alloying elements in solution, which results in an increasing amount of fine, secondary carbide precipitation on tempering. Carbide coarsening occurs with further increase in tempering temperature. This explains the peak in hardness shown in Figures 60 and 61.

The decrease in hardness with increasing HIPing temperature (Figure 61) is due to the presence of coarser primary carbides which form at the higher HIPing temperature.

CONCLUSIONS

1. For powder particle sizes below 37 μm , both cellular and dendritic microstructures are observed. These different microstructures reflect differences in the G/R ratio with particle size.

2. For powder particle sizes above 37 μm , only cellular structures exist; mean cell size decreases with decreasing particle size.
3. Cubic and hexagonal MC are present in the atomized powder; the hexagonal form is shown to be metastable.
4. The cellular structure disappears on annealing of the powder and the interconnected network of carbides is replaced by isolated carbide particles of MC and M_6C .
5. Microhardness of powder particles decreases on annealing.
6. In the HIPed condition, microstructures consist of a matrix of α -ferrite and isolated carbides of MC and M_6C . The carbides are blocky, globular or needle-like in appearance.
7. Independent of prior particle size fraction, the carbide size distribution is skewed to larger carbide sizes with an increase in HIPing temperature, but with no significant change in volume fraction of carbides. Thus, by using lower HIPing temperatures, it is possible to achieve a finer distribution of carbides without a decrease in their volume fraction.
8. At a given HIPing temperature, the carbide size distribution for MC and M_6C carbides is dependent on prior particle size fractions; it is broader for the coarser size fractions.
9. After austenitizing and quenching, martensite is present, independent of prior particle size and HIPing temperature.
10. In the quenched condition, carbide volume fraction decreases with increasing austenitizing temperature, independent of prior particle sizes.

11. Carbide volume fraction increases with tempering, independent of prior particle size fraction.
12. Independent of prior particle size fraction and HIPing temperature, there is a continuous drop in hardness with tempering after austenitizing at the lower temperature A1. For the higher austenitizing temperature A2, tempering at T1 results in a peak in hardness.
13. Tempered hardness decreases with increase in HIPing temperature.

REFERENCES

1. E.J. Dulis in Powder Metallurgy for High Performance Applications, Editors: J.J. Burke and V. Weiss, Syracuse University Press, Syracuse, N.Y., p. 317, 1972.
2. K. Zander, Powder Metallurgy International, Vol. 2, #4, p. 129, 1970.
3. H.F. Fischmeister, in Ann. Reviews Materials Science, Vol. 5, p. 151, 1975.
4. H. Takigawa, H. Manto, N. Kawai and K. Homma, Powder Metallurgy, Vol. 24, #4, p. 196, 1981.
5. P. Hellman in Processing and Properties of High-Speed Tool Steels, Editors: M.G.H. Wells and L.W. Lherbier, The Metallurgical Society of AIME, Warrendale, PA, p. 167, 1980.
6. P. Hellman and H. Wisell, Colloquium on High Speed Tool Steels, Saint-Etienne, France, p. 1, 1975.
7. I.R. Sare and R W.K. Honeycombe, Metal Science, Vol. 13, p. 269, 1979.
8. J.J. Rayment and B. Cantor, Met. Trans., Vol. 12A, p. 1557, 1981.
9. H.F. Fischmeister, A.D. Ozerskii and L. Olsson, Powder Metallurgy, Vol. 25, #1, p. 1, 1982.
10. A. Lawley and M.J. Koczak, "A Fundamental Study of Tool Steels Processed from Rapidly Solidified Powders, Annual Technical Report; Office of Naval Research Contract #N00014-81-K0039, Drexel University, Phila., PA, December 1981.
11. D.J. Blickwede, M. Cohen and G.A. Roberts, ASM Trans. Vol. 42, p. 1161, 1950.
12. J.E. Smugeresky, Met. Trans., Vol. 13A, p. 1535, 1982.
13. C.J. Levi and R. Mehrabian, Met. Trans., Vol. 11B, p. 21, 1980.
14. G.A. Roberts and R A. Cary, Tool Steels, 4th edition, American Society for Metals, Metals Park, Ohio, p. 638, 1980.
15. K. Bungardt, E. Haberling, A. Rose and H.H. Weigand, DEW-Techn. Ber., Vol. 12, p. 111, 1972.

Table I: Chemical Analyses of Powder and Ingot Metallurgy
High Speed Tool Steels (Weight%)

Alloy	Alloy Form	C	Cr	Co	W	V	Mo	Mn	Si	O ₂	N ₂
T15	Powder/This Program	1.52	4.67	5.22	12.19	4.85	----	0.31	0.46	0.0063	0.1
Rex 25	Powder/This Program	1.79	3.01	----	13.29	4.63	6.52	0.31	0.46	0.0061	0.1
T15	Powder/Commercial	1.48	4.00	4.59	12.12	4.65	0.58	0.32	0.42	0.008	0.057
Rex 25	Powder/Commercial	1.81	4.04	0.48	12.46	4.95	6.48	0.40	0.33	0.013	0.086
T15	Ingot/Commercial	1.57	4.62	5.10	13.59	4.86	0.69	0.30	0.21	----	----
Rex 25	Ingot/Commercial	1.82	4.11	0.28	12.35	5.18	6.48	0.34	0.39	----	0.039

Table 11: Coding System for Powder Consolidation and Heat Treatment

Code	Interpretation
H1	Hot Isostatically Pressed at 1130°C (2065°F)
H2	Hot Isostatically Pressed at 1195°C (2185°F)
A1	Austenitized at 1176°C (2150°F) for 4 mins. and oil-quenched
A2	Austenitized at 1226°C (2240°F) for 4 mins. and oil-quenched
T1	Tempered for (2 + 2 + 2) hrs. at 538°C (1000°F)
T2	Tempered for (2 + 2 + 2) hrs. at 552°C (1025°F)
T3	Tempered for (2 + 2 + 2) hrs. at 565°C (1050°F)

Table III: HIPed Material - Lattice Parameters of Matrix and Carbides

SAMPLE	PHASES PRESENT	LATTICE PARAMETER (Å)
H1/840 μm screen	Matrix: α-ferrite	$a_o = 2.873 \text{ Å}$
	Carbides: cubic M_6C	$a_o = 11.039 \text{ Å}$
	cubic MC	$a_o = 4.173 \text{ Å}$
H1/55-7 μm screen	Matrix: α-ferrite	$a_o = 2.875 \text{ Å}$
	Carbides: cubic M_6C	$a_o = 11.043 \text{ Å}$
	cubic MC	$a_o = 4.175 \text{ Å}$
H1/250-840 μm screen	Matrix: α-ferrite	$a_o = 2.875 \text{ Å}$
	Carbides: cubic M_6C	$a_o = 11.047 \text{ Å}$
	cubic MC	$a_o = 4.175 \text{ Å}$
H2/250-840 μm screen	Matrix: α-ferrite	$a_o = 2.873 \text{ Å}$
	Carbides: cubic M_6C	$a_o = 11.054 \text{ Å}$
	cubic MC	$a_o = 4.178 \text{ Å}$
H1/44-100 μm screen	Matrix: α-ferrite	$a_o = 2.866 \text{ Å}$
	Carbides: cubic M_6C	$a_o = 11.040 \text{ Å}$
	cubic MC	$a_o = 4.175 \text{ Å}$
H2/44-100 μm screen	Matrix: α-ferrite	$a_o = 2.870 \text{ Å}$
	Carbides: cubic M_6C	$a_o = 11.049 \text{ Å}$
	cubic MC	$a_o = 4.177 \text{ Å}$
H1/<44 μm screen	Matrix: α-ferrite	$a_o = 2.869 \text{ Å}$
	Carbides: cubic M_6C	$a_o = 11.049 \text{ Å}$
	cubic MC	$a_o = 4.176 \text{ Å}$
H2/<44 μm screen	Matrix: α-ferrite	$a_o = 2.871 \text{ Å}$
	Carbides: cubic M_6C	$a_o = 11.051 \text{ Å}$
	cubic MC	$a_o = 4.178 \text{ Å}$

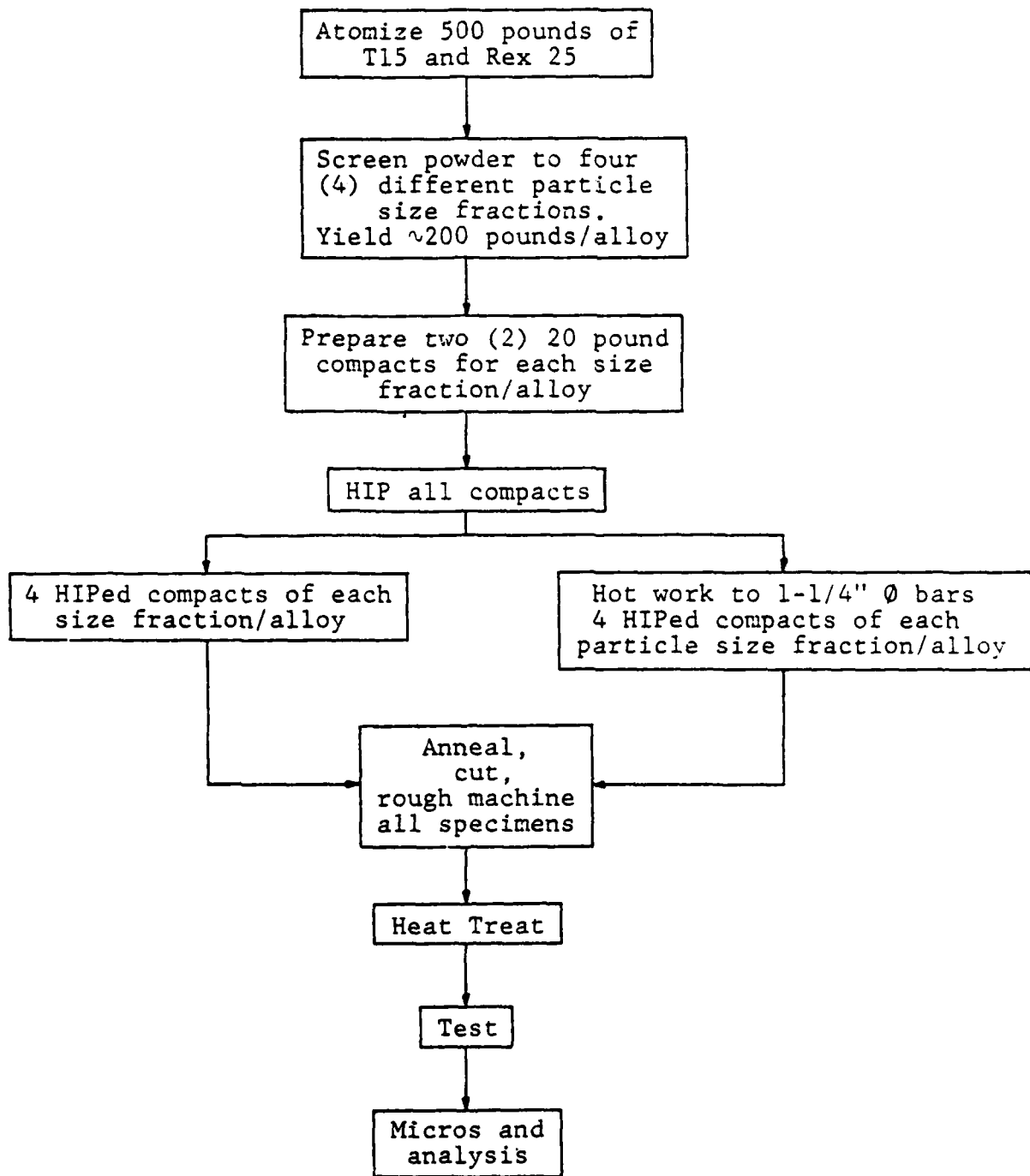


Figure 1. Schematic of overall program.

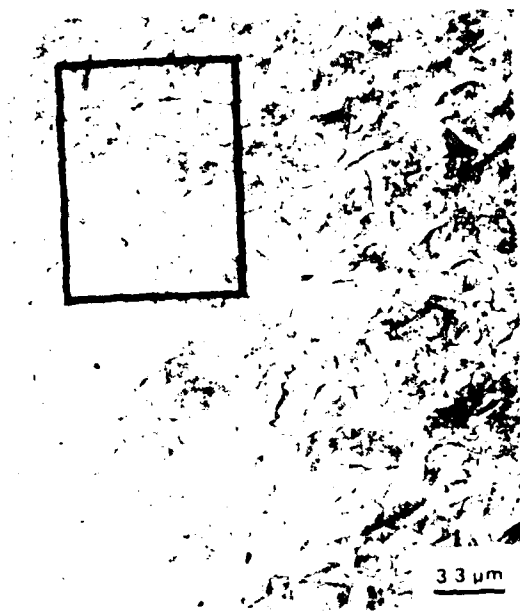


Figure 2. As-atomized powder, 500-700 μm ; Kalling's etch. SEM



Figure 3. As-atomized powder, 500-700 μm ; Kalling's etch. SEM

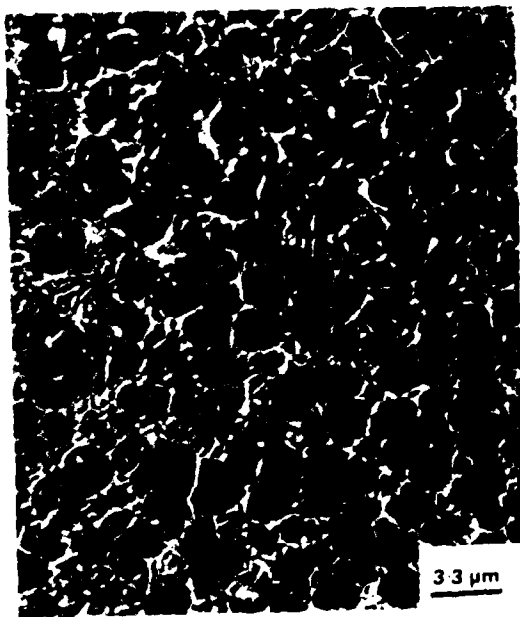


Figure 4. As-atomized powder, 110-130 μm , Kalling's etch. SEM



Figure 5. As-atomized powder, 110-130 μm , Kalling's etch. SEM

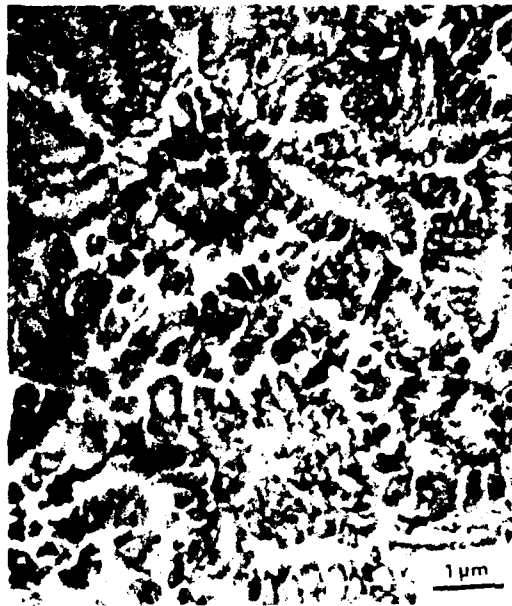


Figure 6. As-atomized powder, <37 μm ;
Kalling's etch. SEM.



Figure 7. As-atomized powder, <37 μm ;
Kalling's etch. SEM.

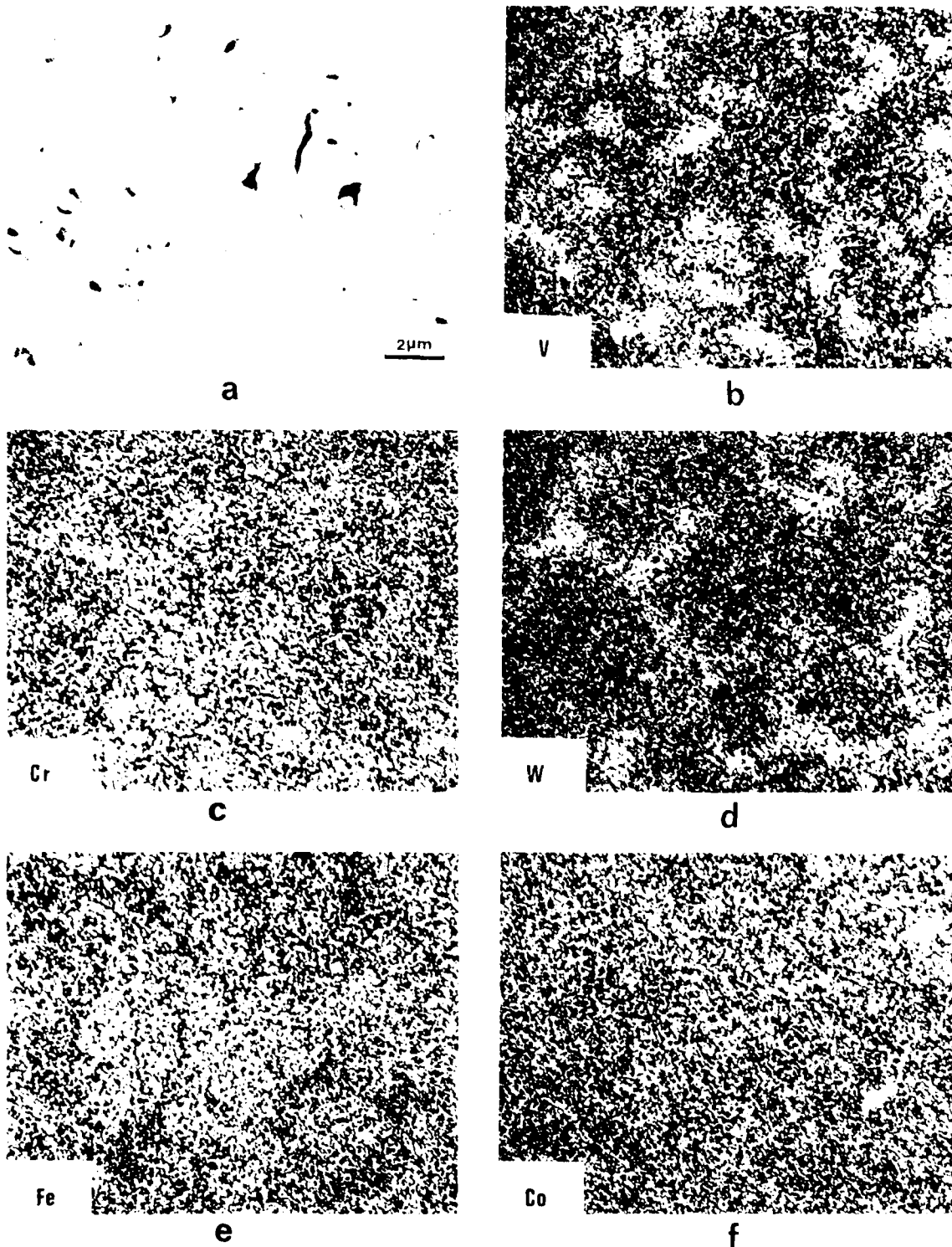
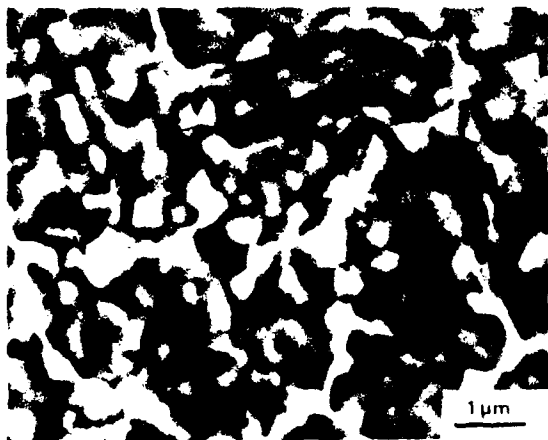
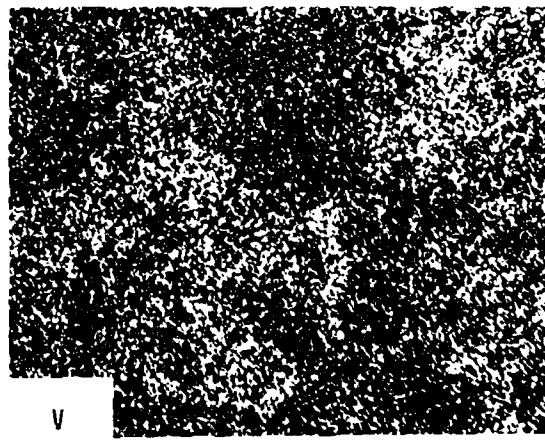


Figure 8. As-atomized powder, 550-700 μm , Kalling's etch. Element mapping.
 a. Reference SEM, b. Vanadium, c. Chromium, d. Tungsten, e. Iron, f. Cobalt.

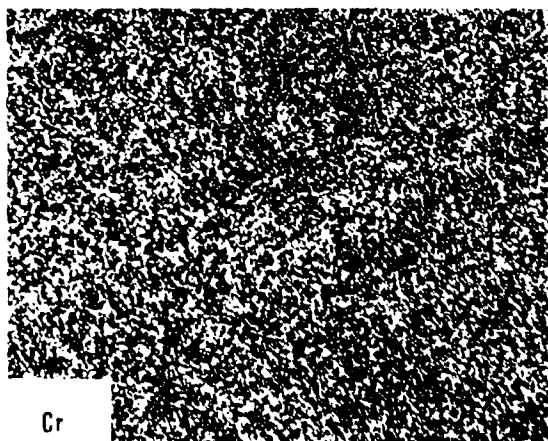


a



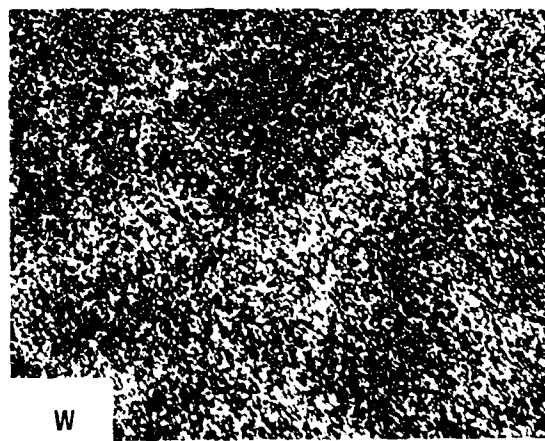
V

b



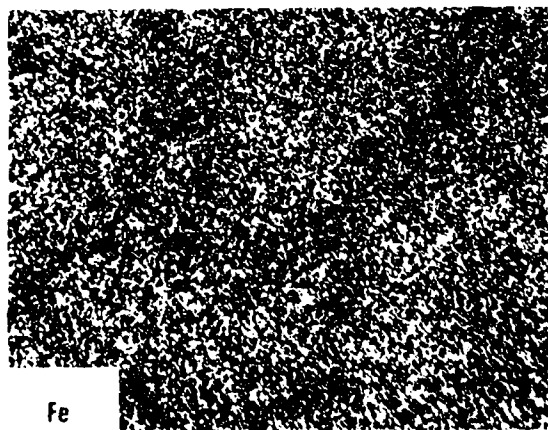
Cr

c



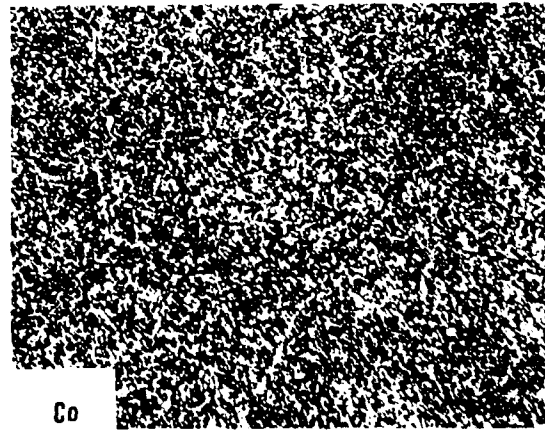
W

d



Fe

e



Co

f

Figure 9. As-atomized powder, <37 μm, Kalling's etch. Element-mapping.
a. Reference SEM, b. Vanadium, c. Chromium, d. Tungsten,
e. Iron, f. Cobalt.

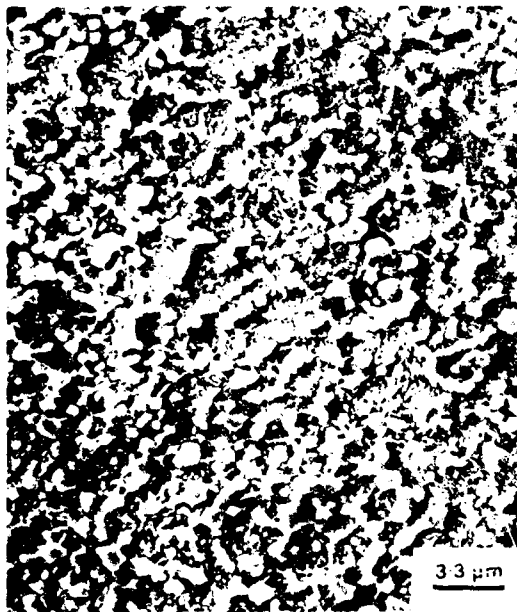


Figure 10. HIPed (H1)/250-840 μm screen; Kalling's etch. SEM.



Figure 11. HIPed (H1)/ $\leq 44 \mu\text{m}$ screen; Kalling's etch. SEM.



Figure 12. HIPed (H2) 250-840 μm screen; Kalling's etch. SEM.

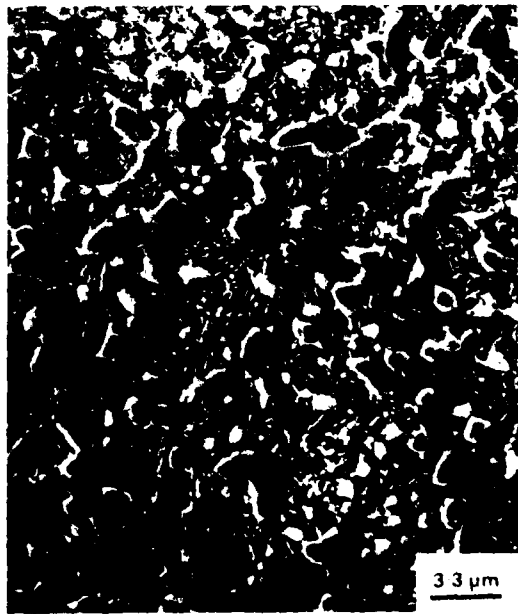


Figure 13. HIPed (H2)/ $\leq 44 \mu\text{m}$ screen; Kalling's etch. SEM.

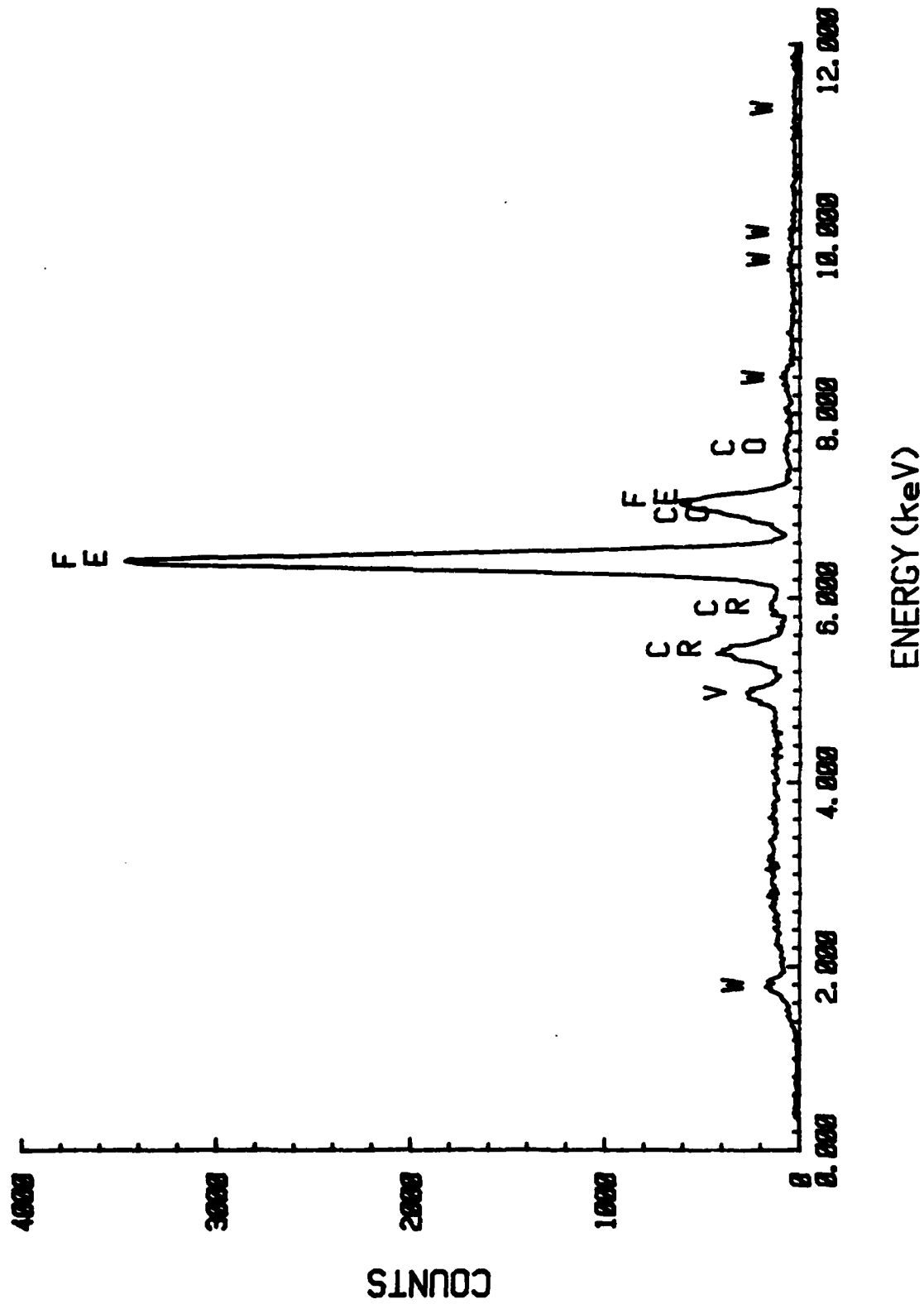


Figure 14. HIPed (H1)/250-840 μm screen. EDAX Spectrum - Matrix.

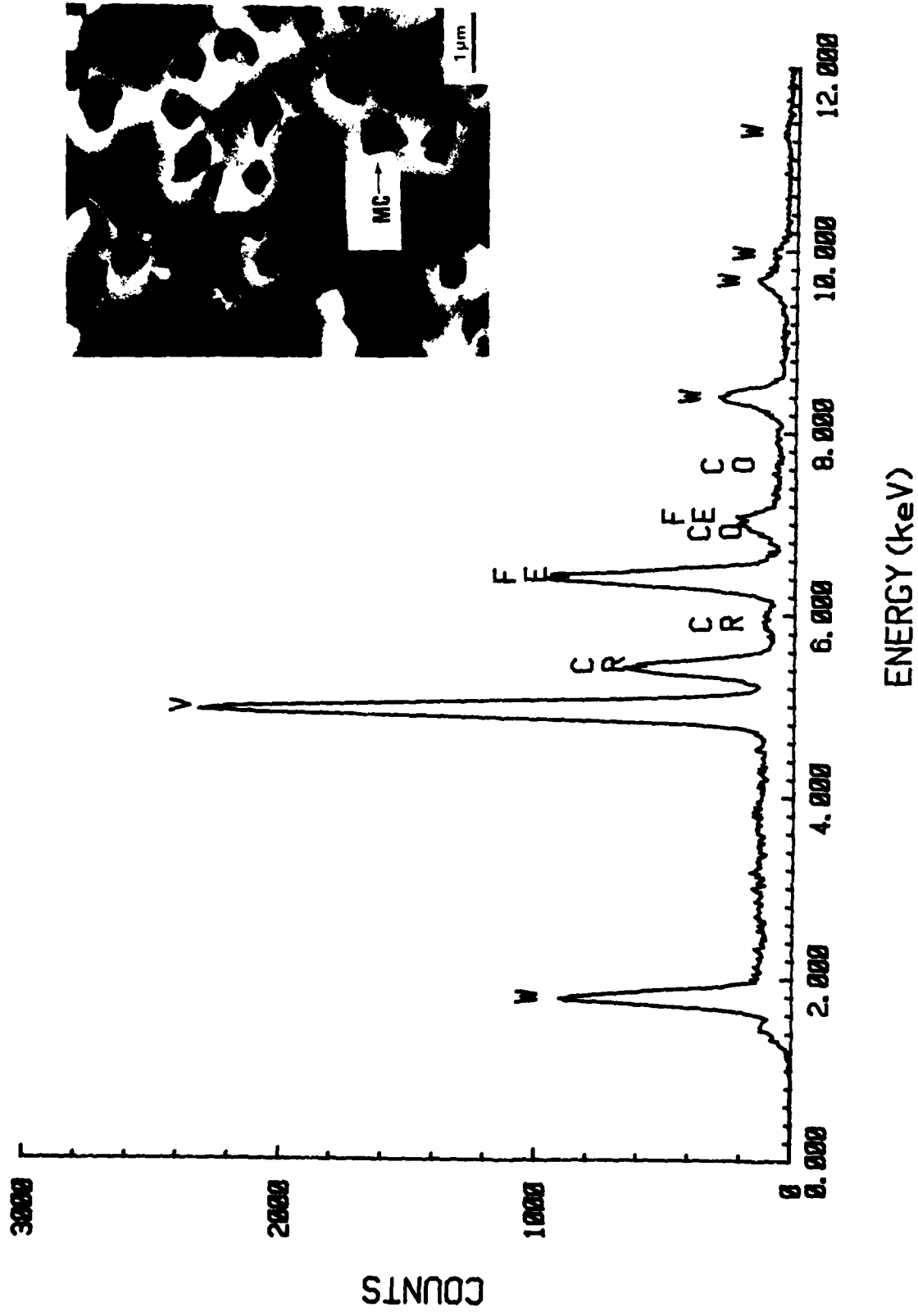


Figure 15. HIPed (H1)/250-840 μm screen. EDAX Spectrum - MC Carbides (Black).

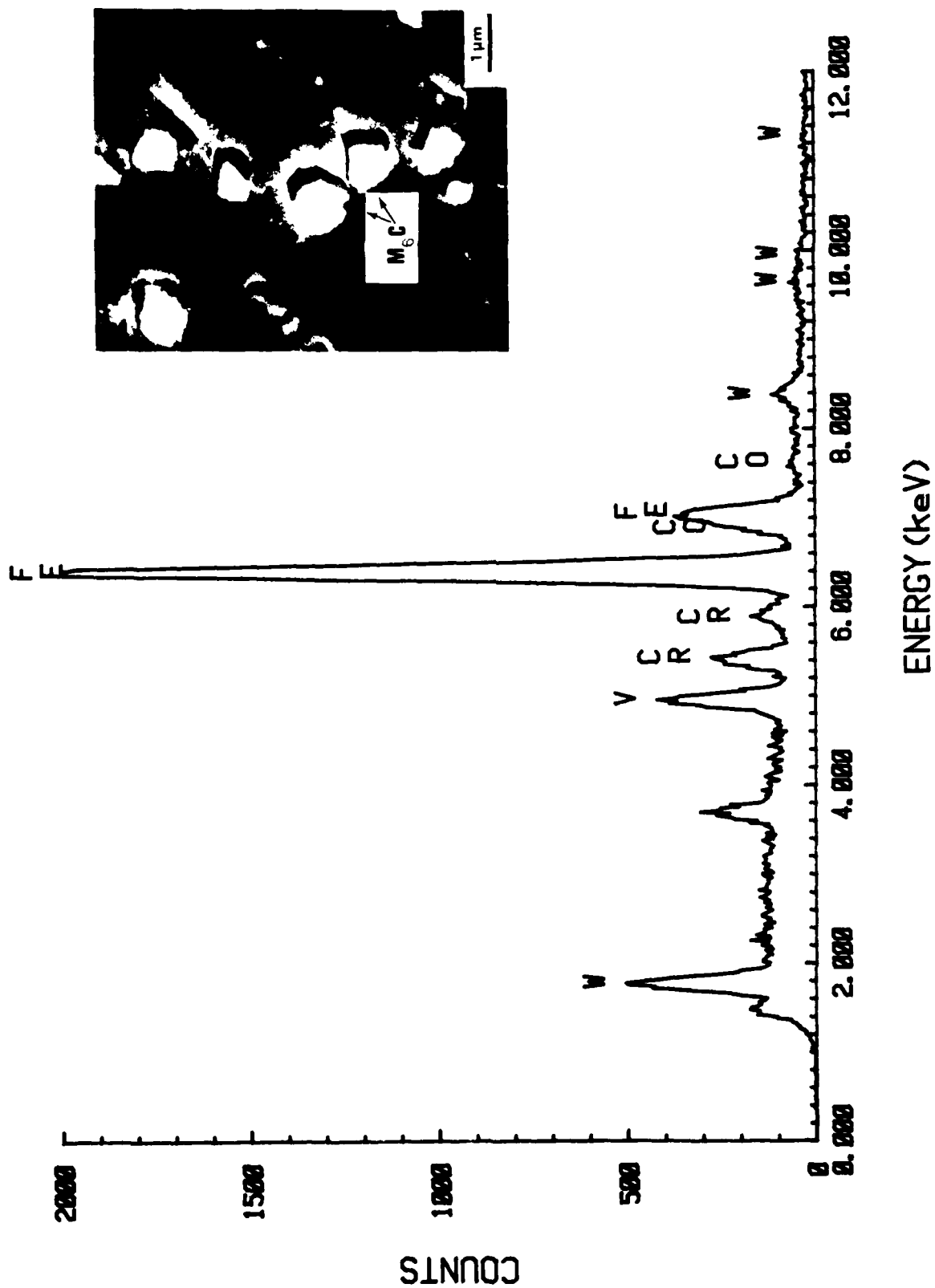


Figure 16. HIPed (H1)/250-840 μm screen. EDAX Spectrum - M₆C Carbides.

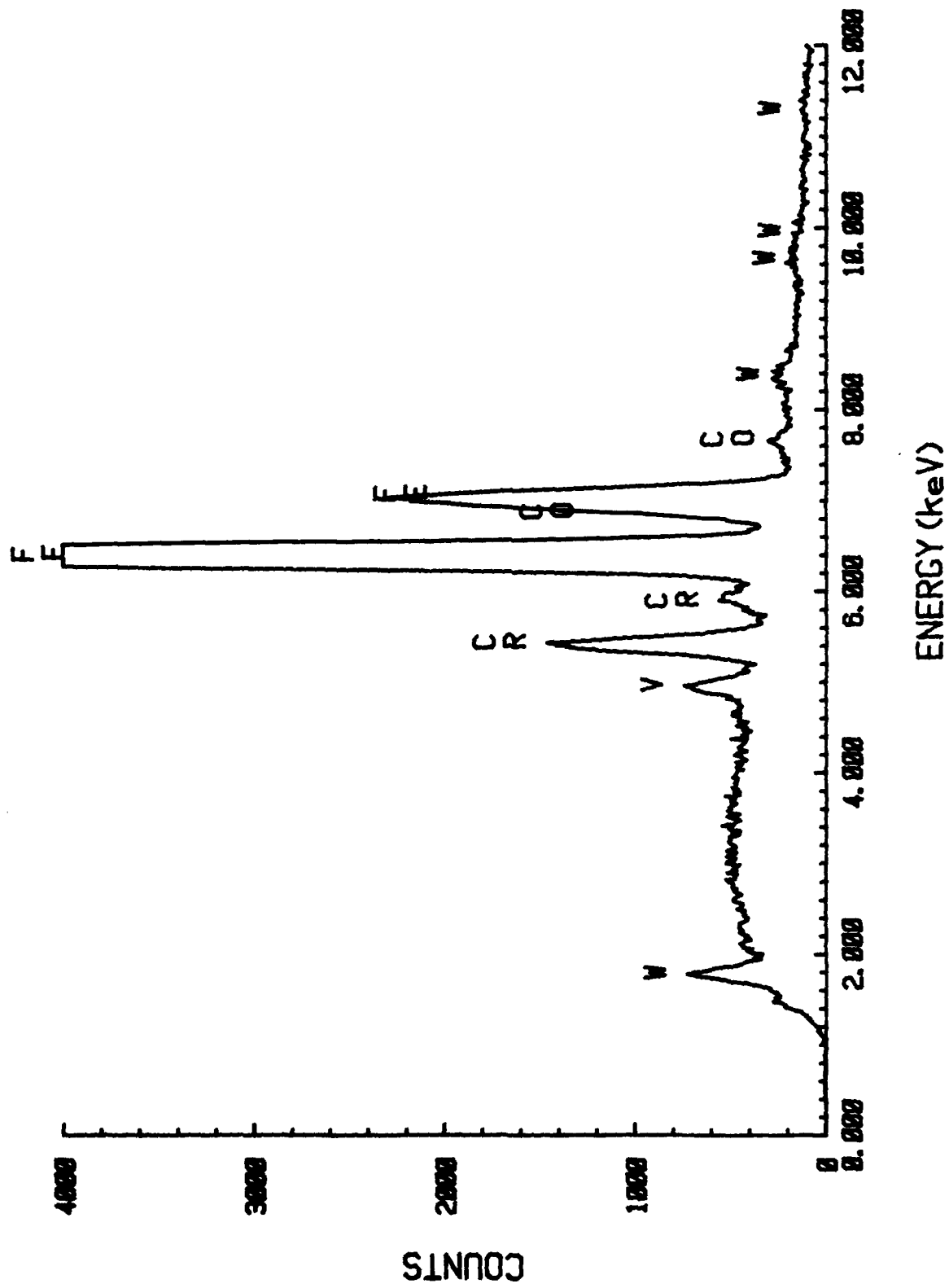


Figure 17. HIPed (H2)/250-840 μm screen. EDAX Spectrum - Matrix.

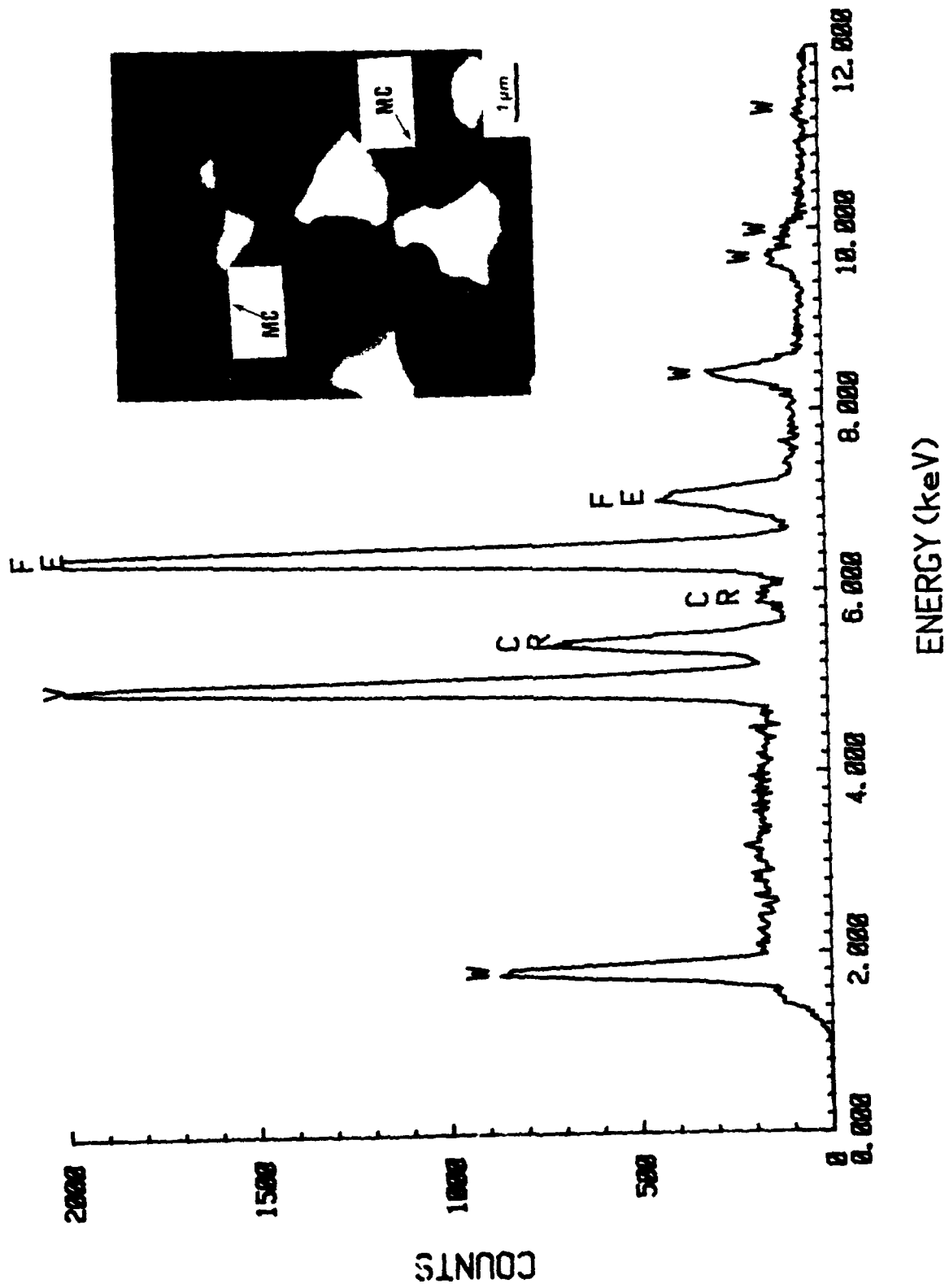


Figure 18. HIPed (H2)/750-840 μm screen. EDAX Spectrum - MC Carbides (Black).

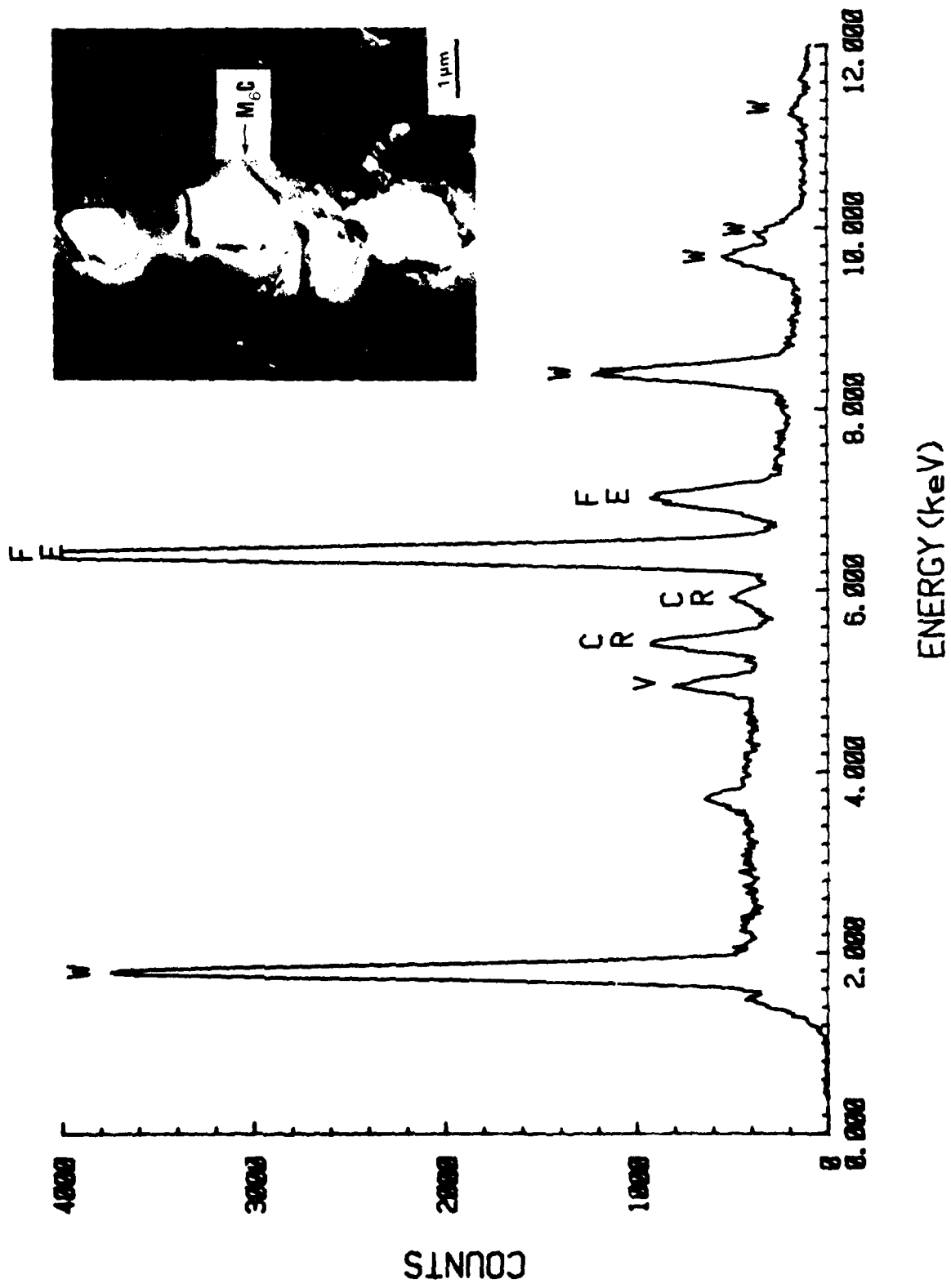


Figure 19. HIPed (H2)/250-840 μm screen. EDAX Spectrum - M₆C Carbides.

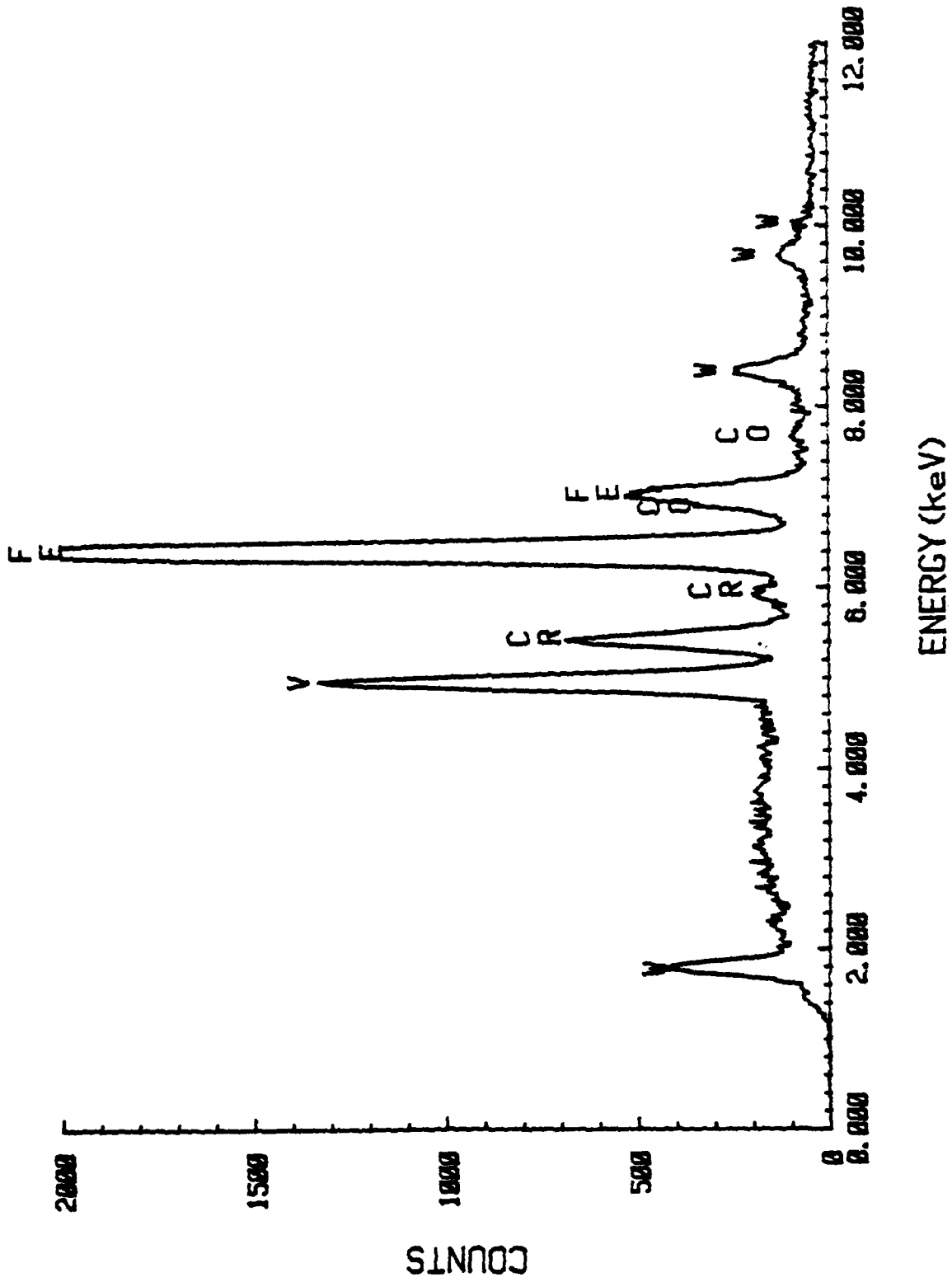


Figure 20. HIPed (III)/ ≤ 44 μm screen. EDAX Spectrum - MC Carbides.

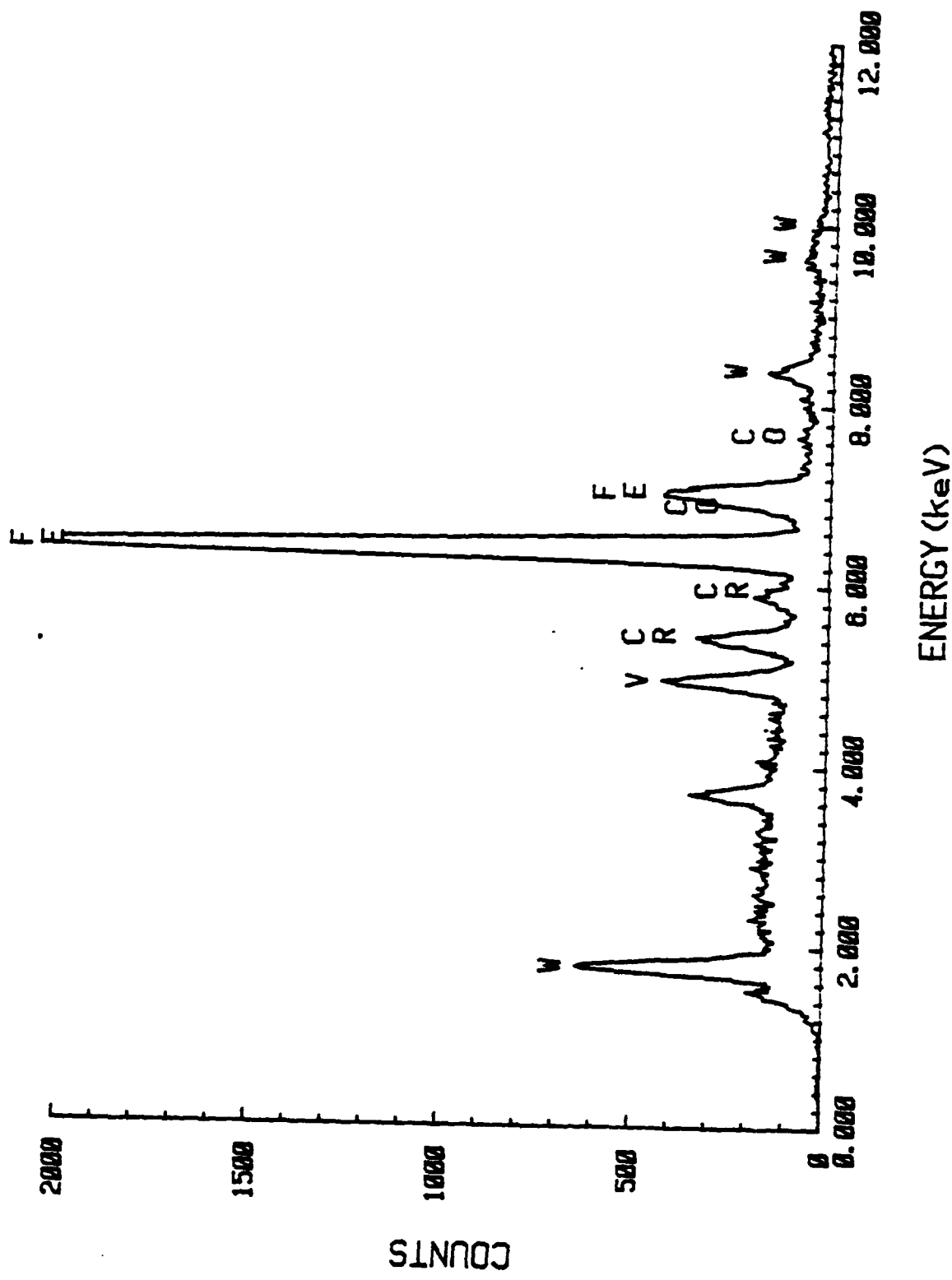


Figure 21. HIPed (III) / 44 μm screen. EDAX Spectrum - M₆C Carbides.

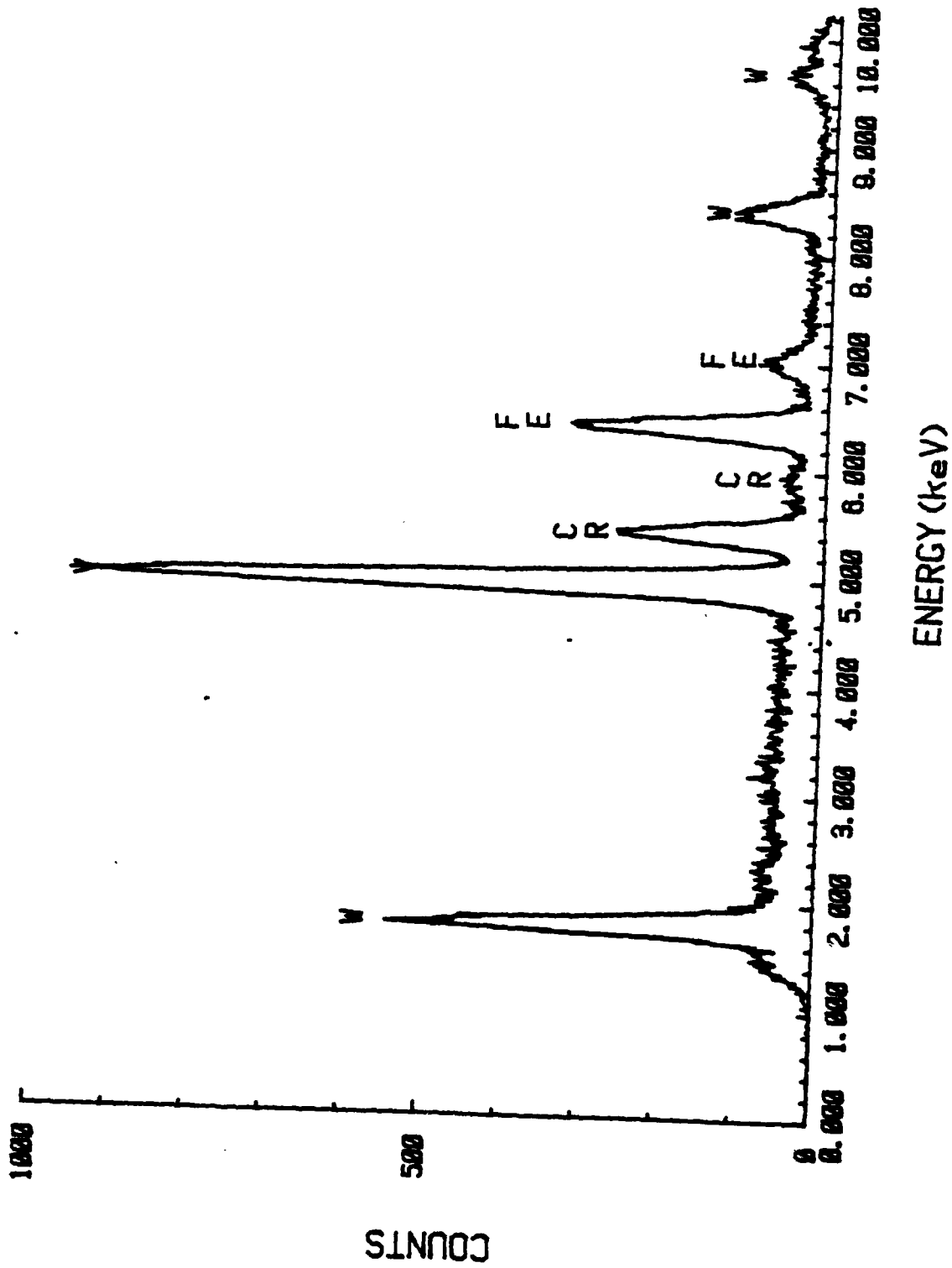


Figure 22. HIPed (H2)/ ≤ 44 μm screen. EDAX Spectrum - MC Carbides.

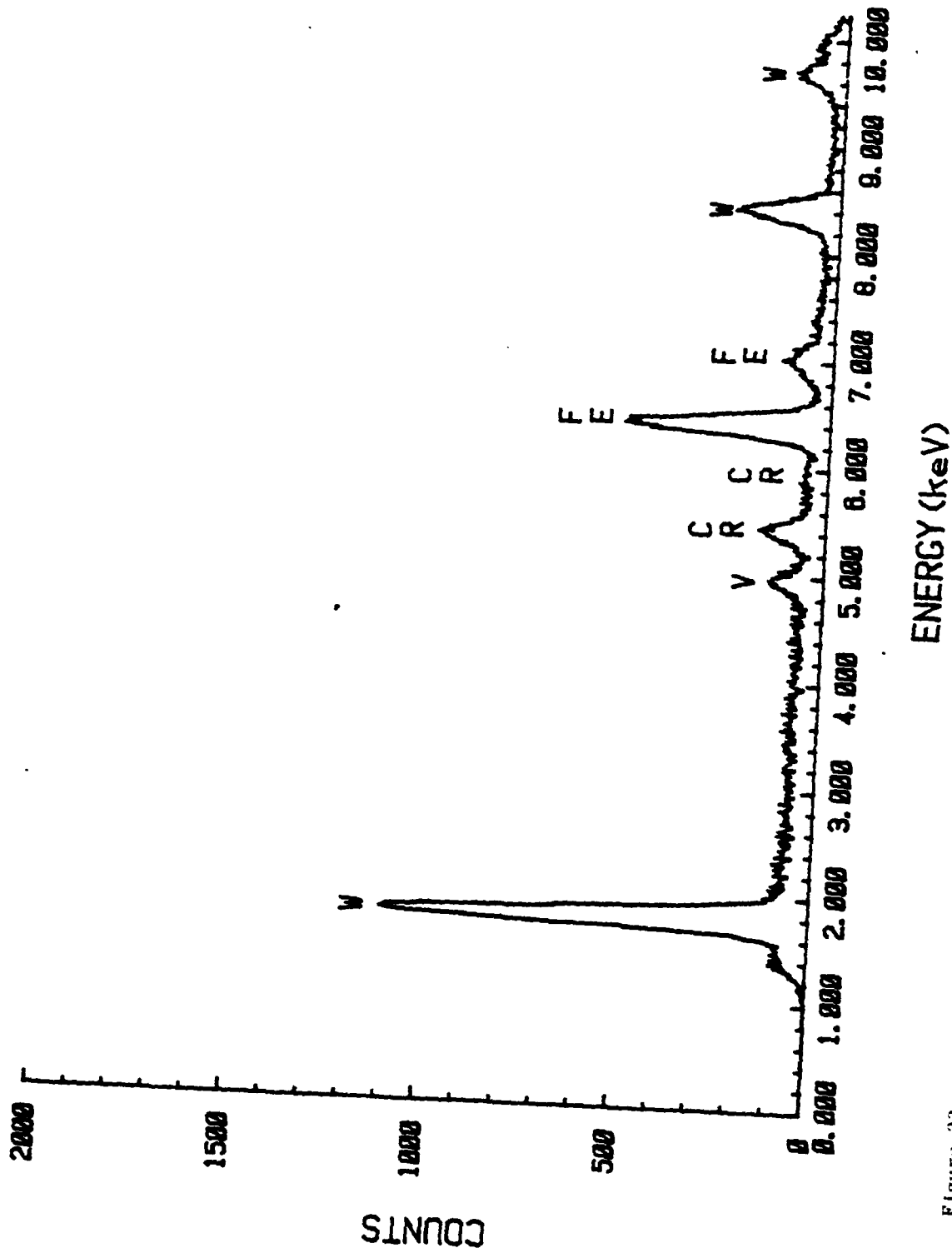


Figure 23. HIPed (H2)/ ϵ 44 μ m screen. EDAX Spectrum - M_6C Carbides.

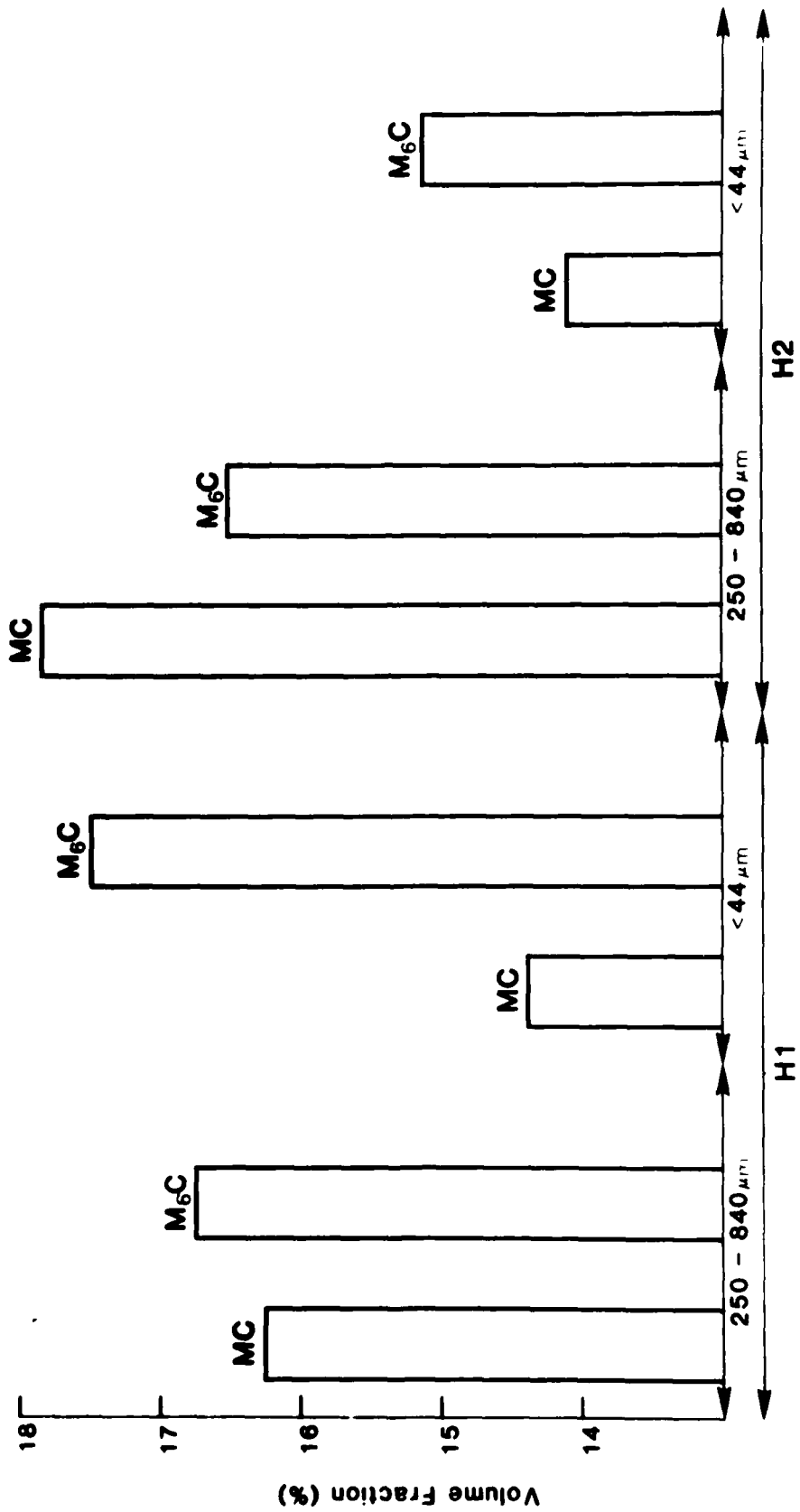


Figure 24. Carbide volume fraction as a function of powder screen fraction and HIPing temperature.

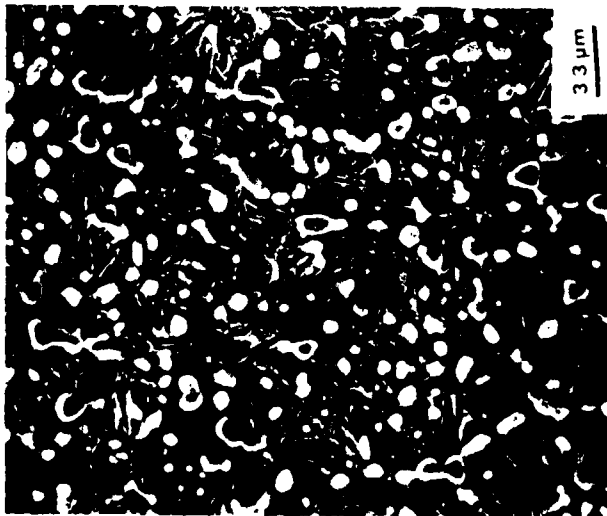


Figure 25. Heat-treated material;
H2+Al/250-840 um screen.
Kalling's etch. SEM

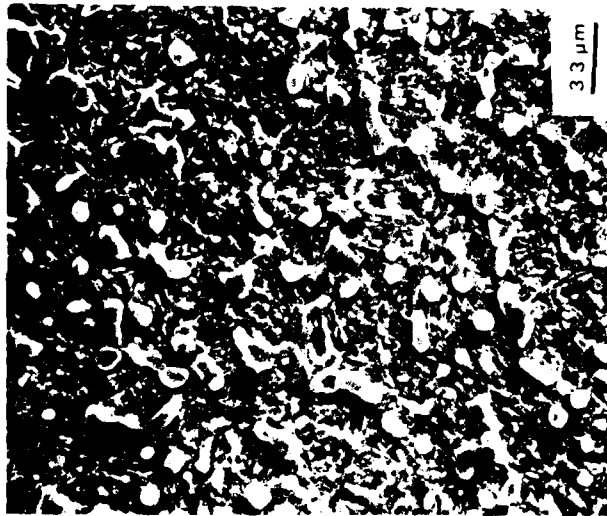


Figure 26. Heat-treated material;
H2+Al+T1/250-840 um screen.
Kalling's etch. SEM

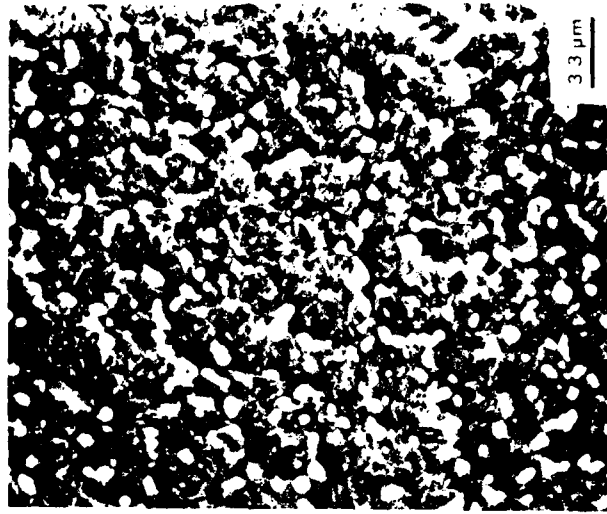


Figure 27. Heat-treated material;
H2+Al+T3/250-840 um screen.
Kalling's etch. SEM

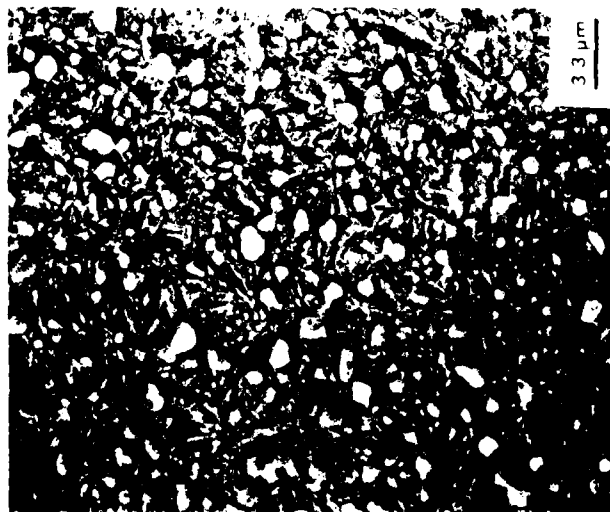


Figure 28. Heat-treated material;
H2+A2/250-840 μm screen,
Kalling's etch. SEM

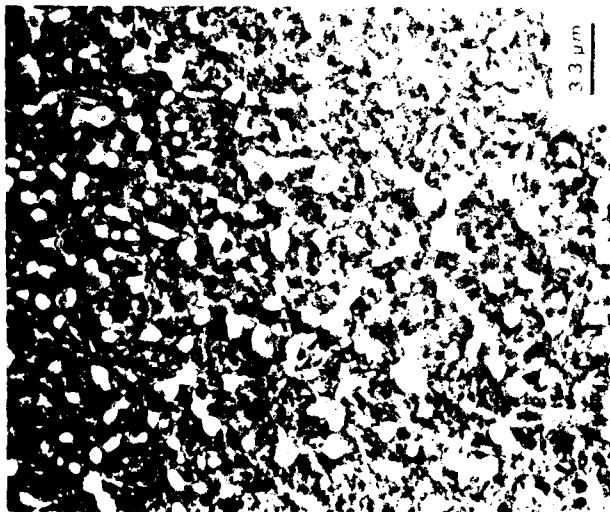


Figure 29. Heat-treated material;
H2+A2+T1/250-840 μm screen,
Kalling's etch. SEM

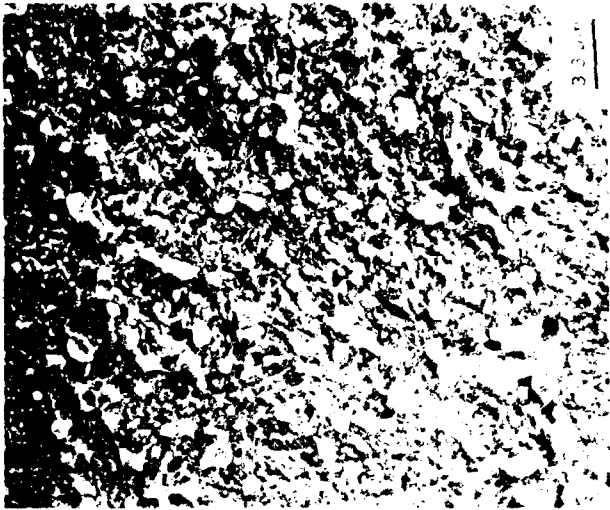


Figure 30. Heat-treated material;
H2+A2+T3/250-840 μm screen,
Kalling's etch. SEM

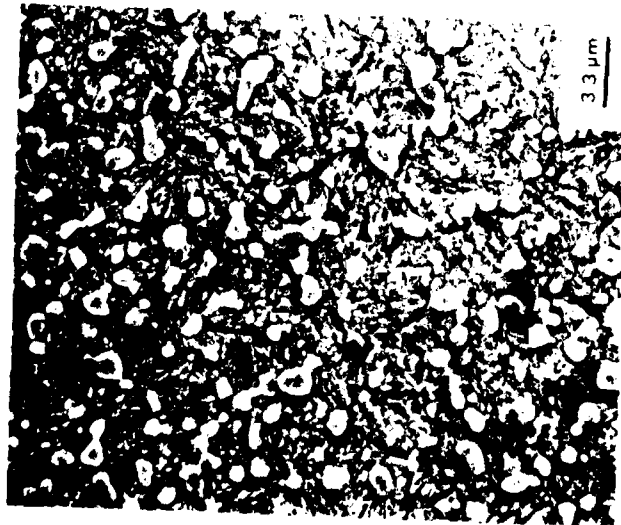


Figure 31. Heat-treated material;
H2+Al/≤44 μm screen,
Kalling's etch. SEM

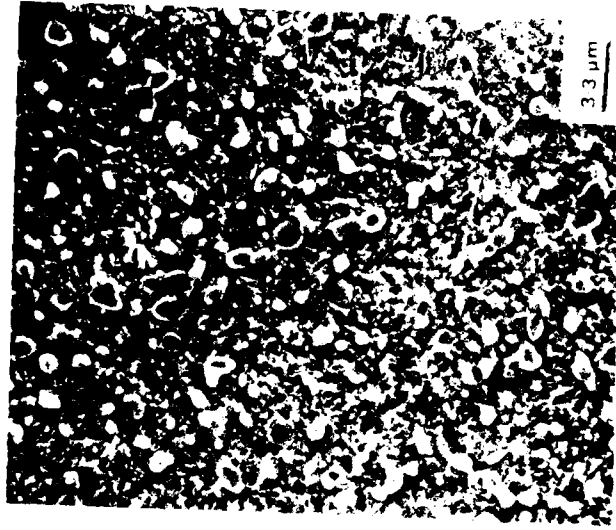


Figure 32. Heat-treated material;
H2+Al+T1/≤44 μm screen,
Kalling's etch. SEM

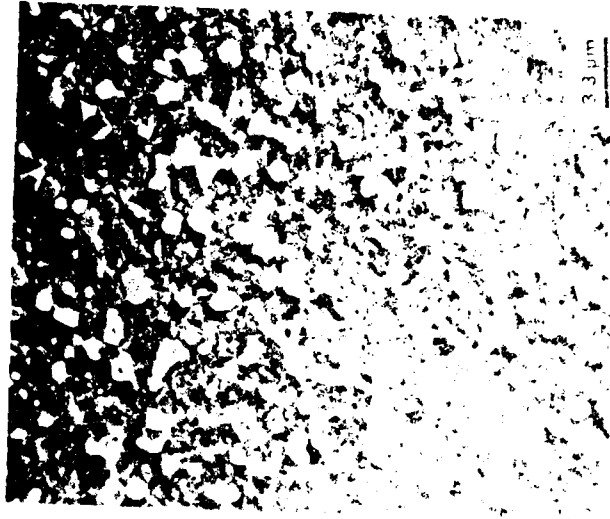


Figure 33. Heat-treated material;
H2+Al+T3/≤44 μm screen,
Kalling's etch. SEM



Figure 34. Heat-treated material; H₂+A₂+T₁/≤44 μm screen.
Kalling's etch. SEM.

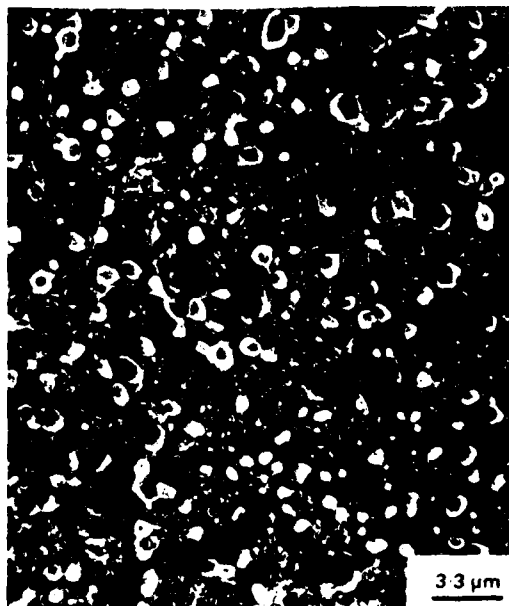


Figure 35. Heat-treated material; H₂+A₂+T₃/≤44 μm screen.
Kalling's etch. SEM.

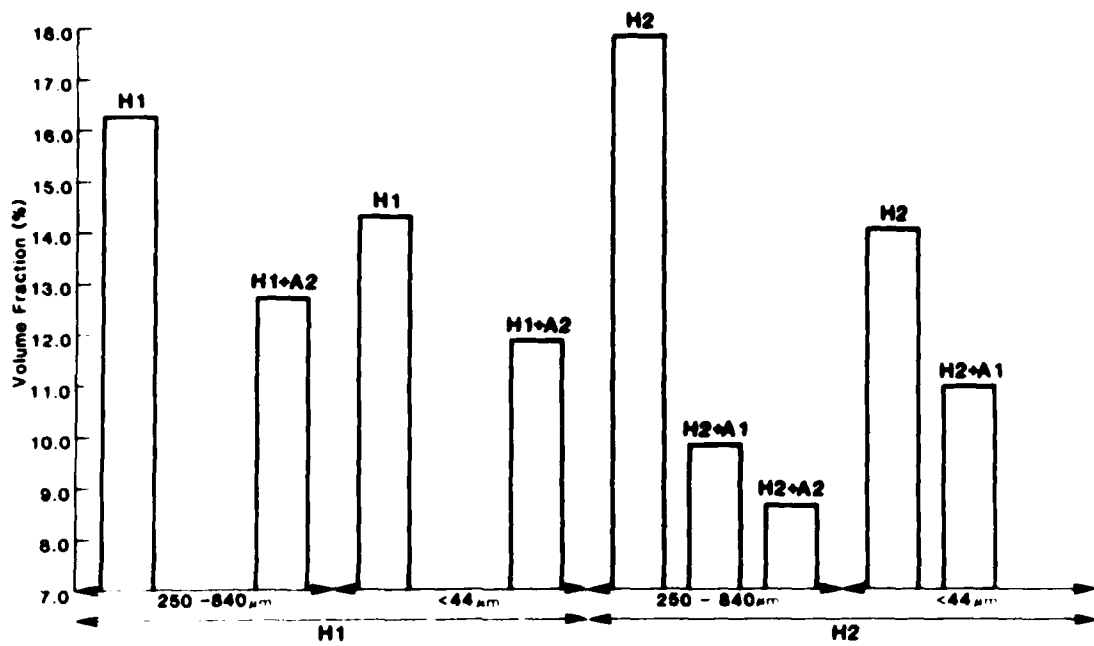


Figure 36. MC carbide volume fraction as a function of powder screen fraction, HIPing temperature and austenitizing temperature.

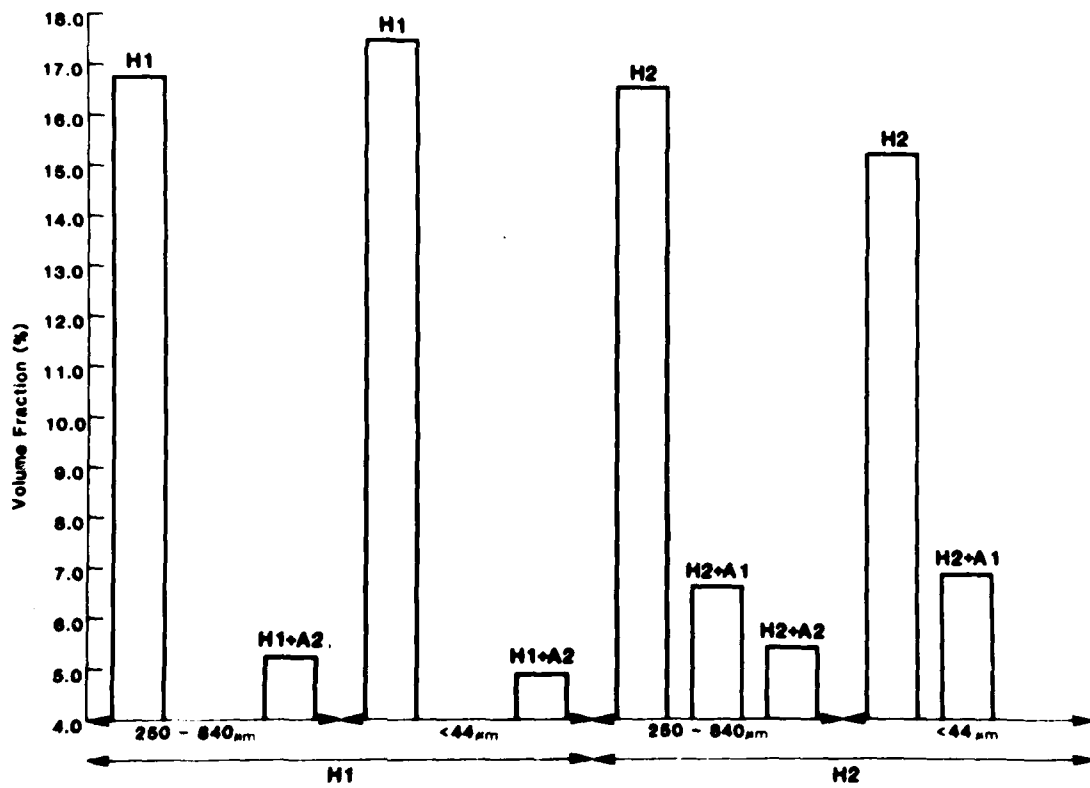


Figure 37. MC carbide volume fraction as a function of powder screen fraction, HIPing temperature and austenitizing temperature.

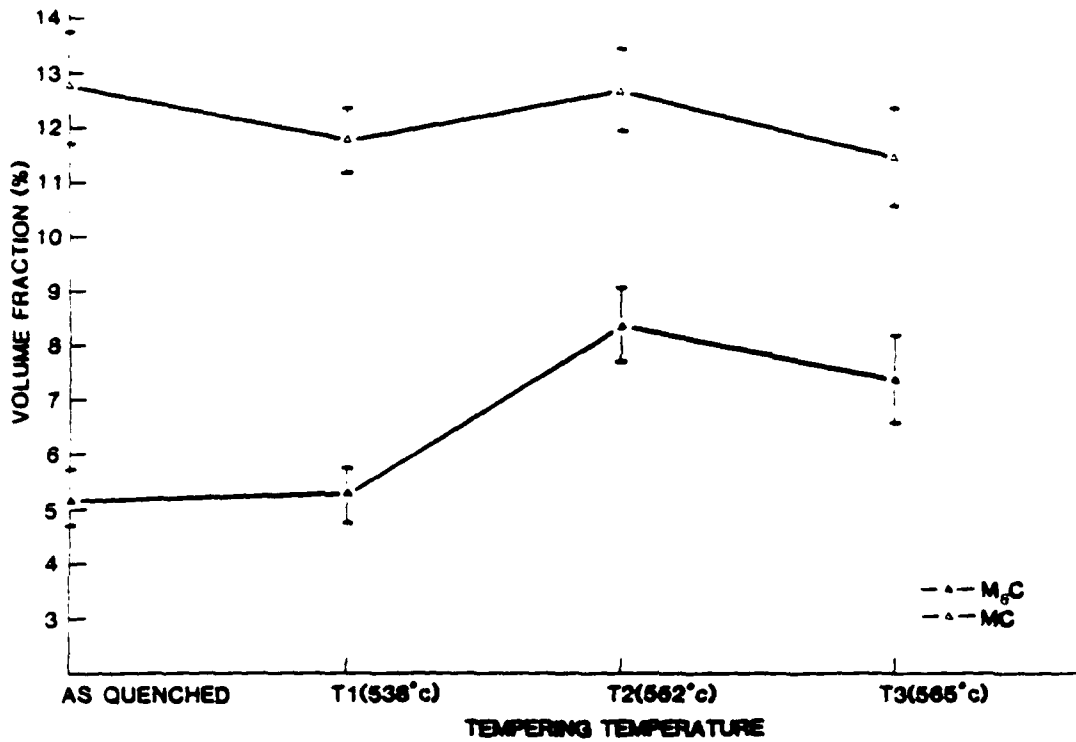


Figure 38. Volume fraction of MC and M₆C carbides as a function of tempering temperature; H1 + A2/250-840 μm.

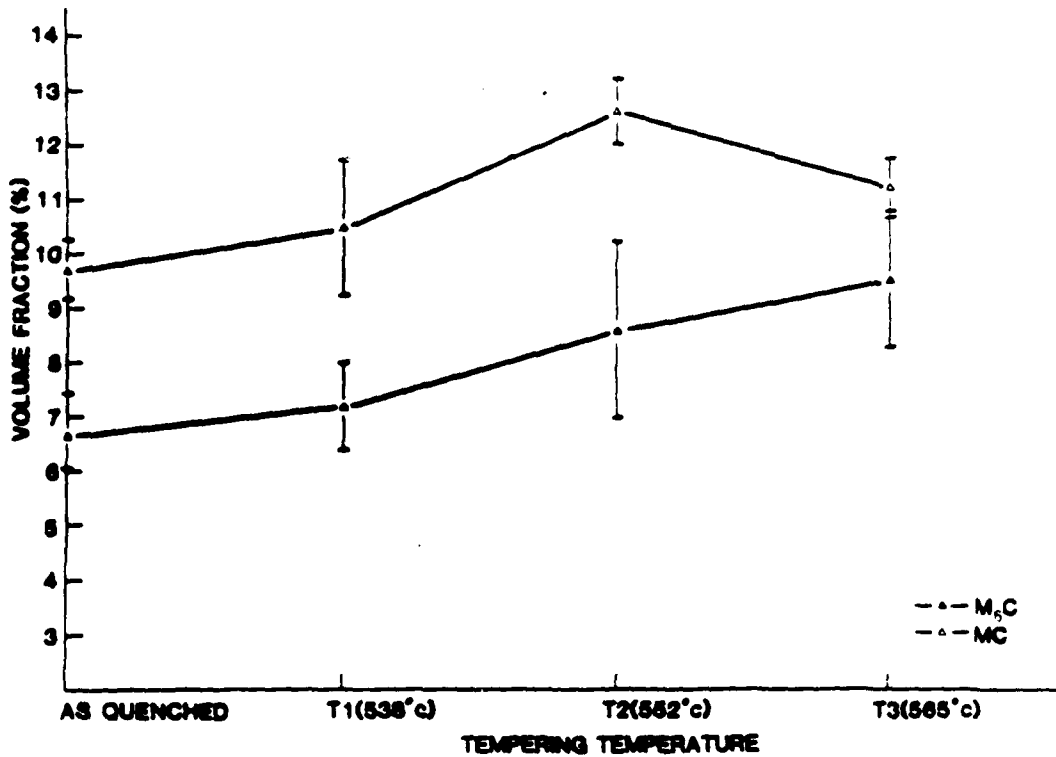


Figure 39. Volume fraction of MC and M₆C carbides as a function of tempering temperature; H2 + A1/250-840 μm.

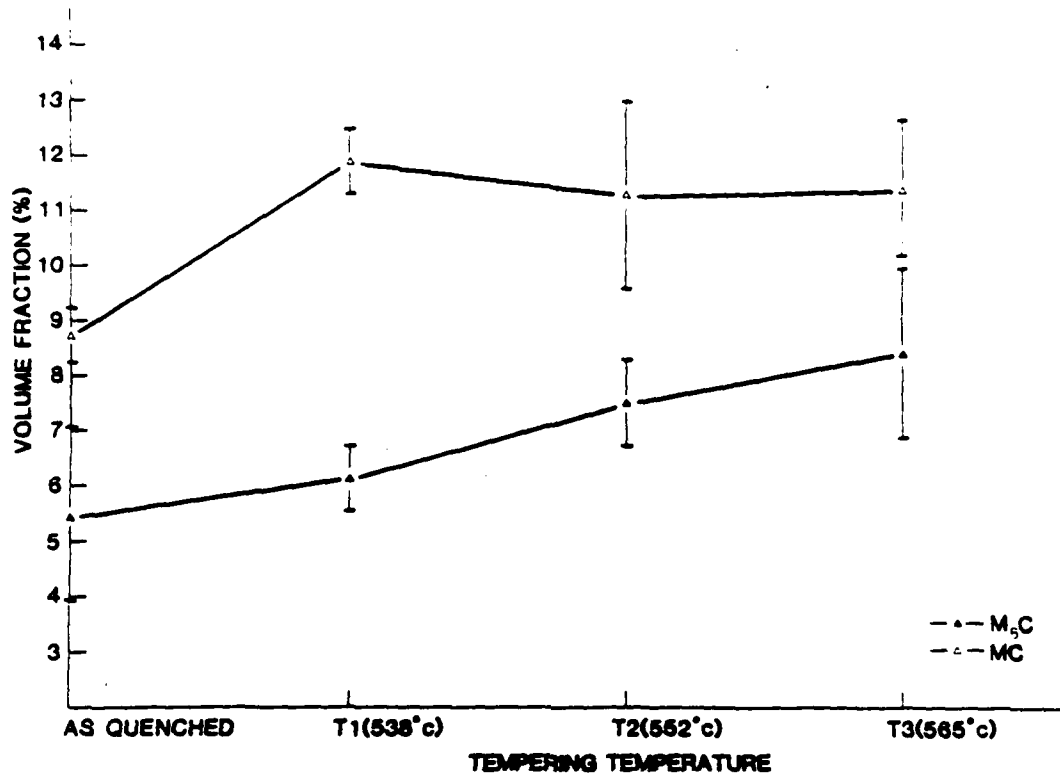


Figure 40. Volume fraction of MC and M₆C carbides as a function of tempering temperature; H₂ + A₂/250-840 μm.

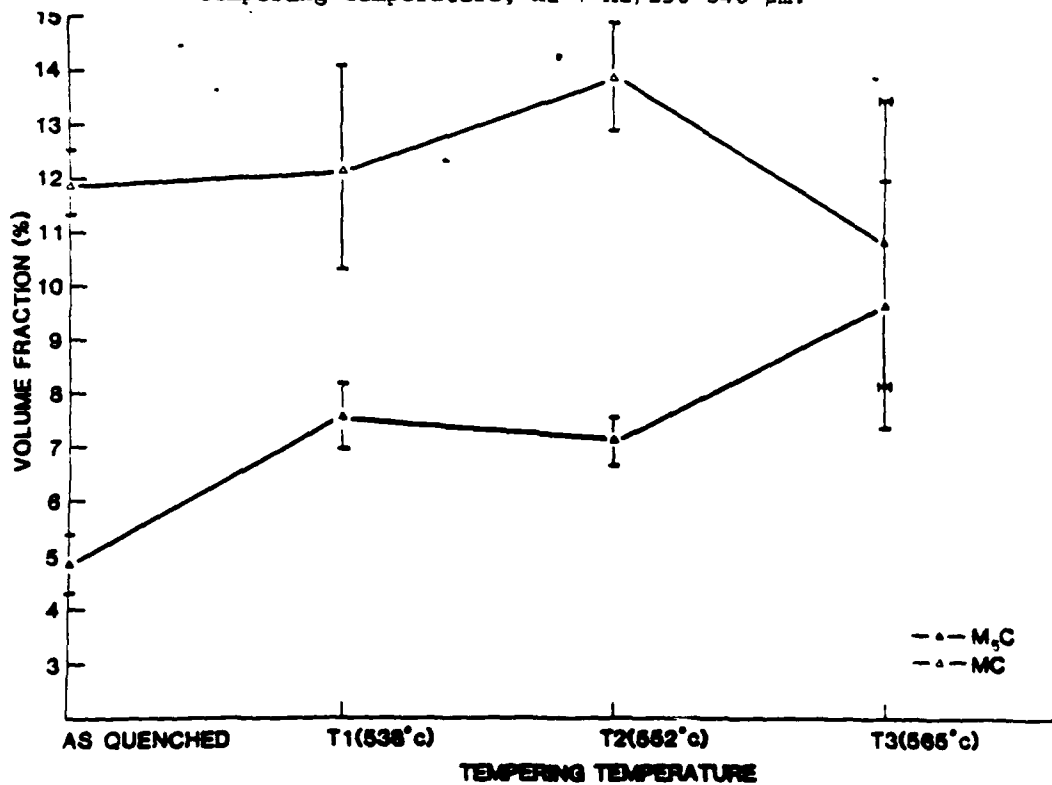


Figure 41. Volume fraction of MC and M₆C carbides as a function of tempering temperature; H₁ + A₂/≤44 μm.

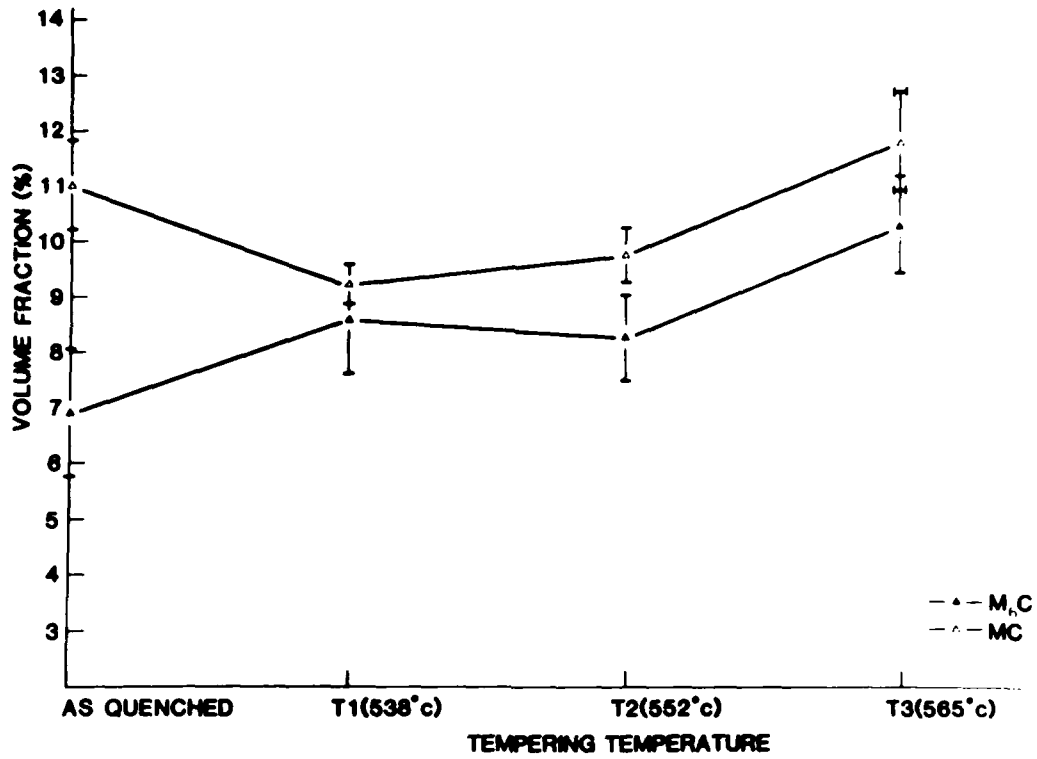


Figure 42. Volume fraction of MC and M₆C carbides as a function of tempering temperature; H₂ + Al/≤44 μm.

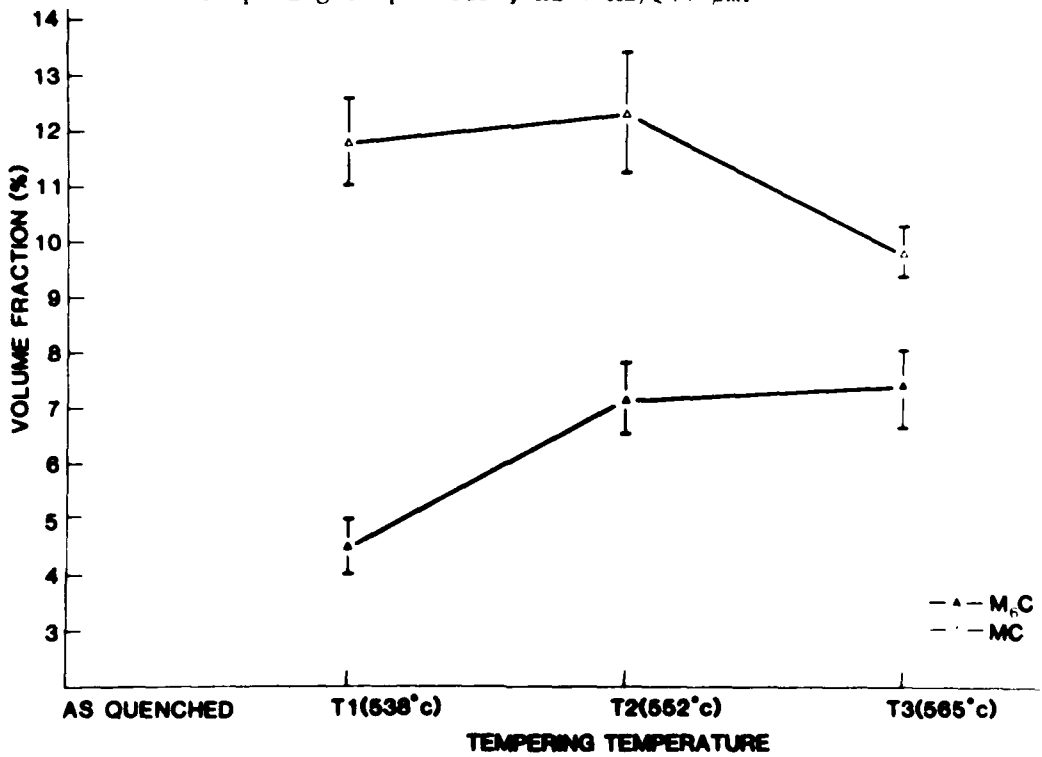
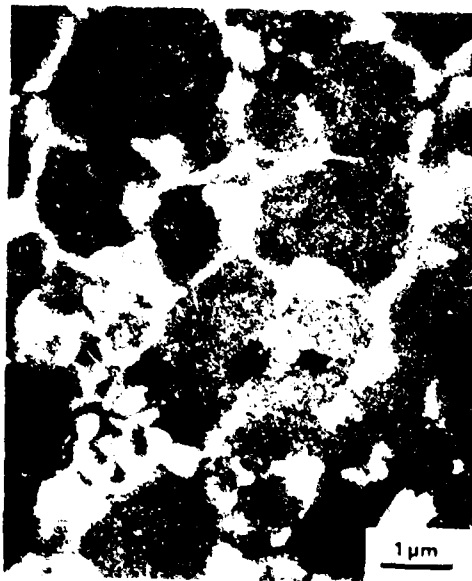


Figure 43. Volume fraction of MC and M₆C carbides as a function of tempering temperature; H₂ + A₂/≤44 μm.



(a)

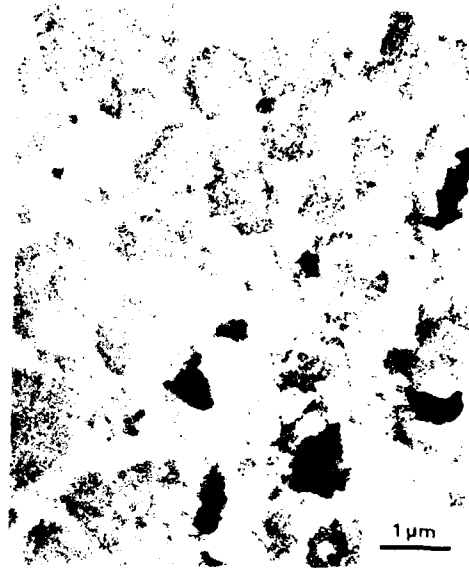


(b)

Figure 99. As-atomized powder, 100 μm; Rolling: etch (HCl + Picral, SF₆).



(a)



(b)



(c)

Figure 45. As-atomized powder; Kallina's etch. SEM. (a) 62-74 μm , (b) 350-420 μm , (c) 800-1000 μm .

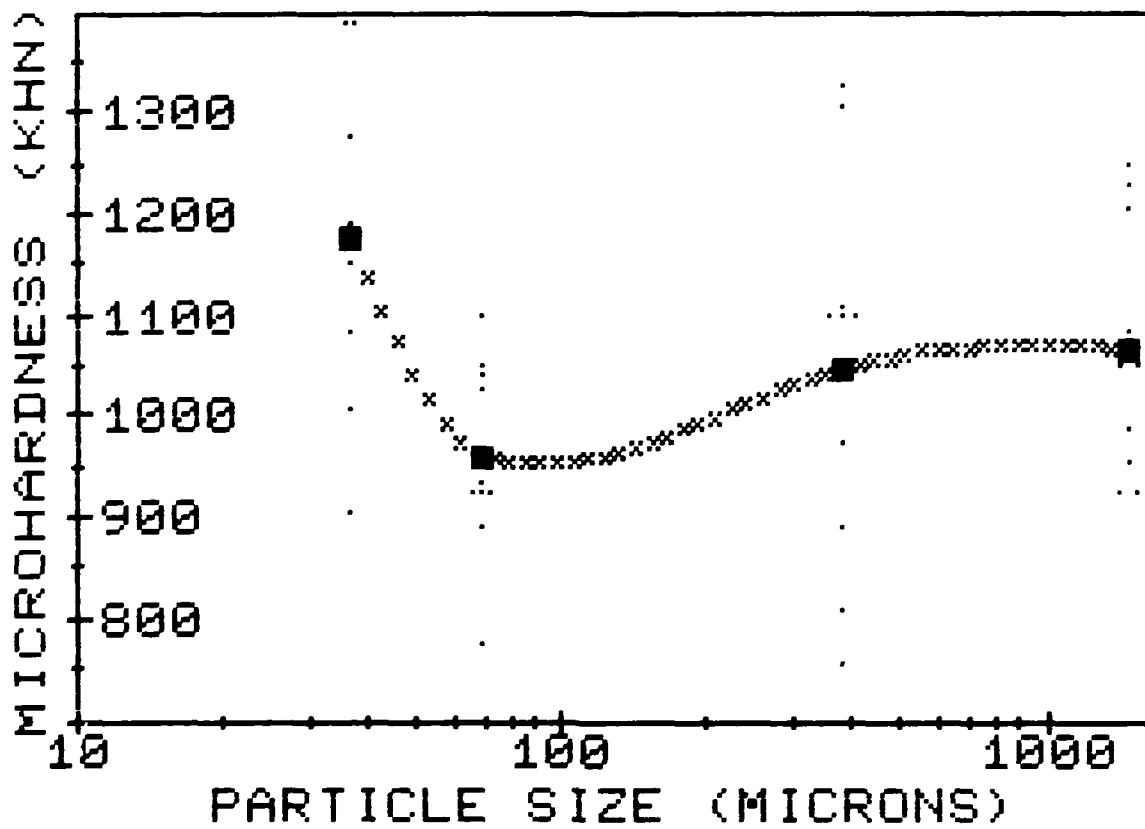
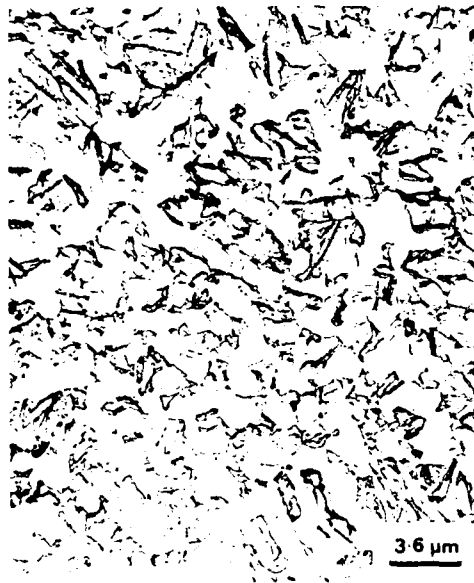


Figure 46. Microhardness of as-atomized powder as a function of particle size (Indentation load = 25 g).



(a)



(b)

Figure 47. Annealed powder; TEM/replica. Kalling's etch. a) 840-2000 μm. b) ≤ 37 μm.

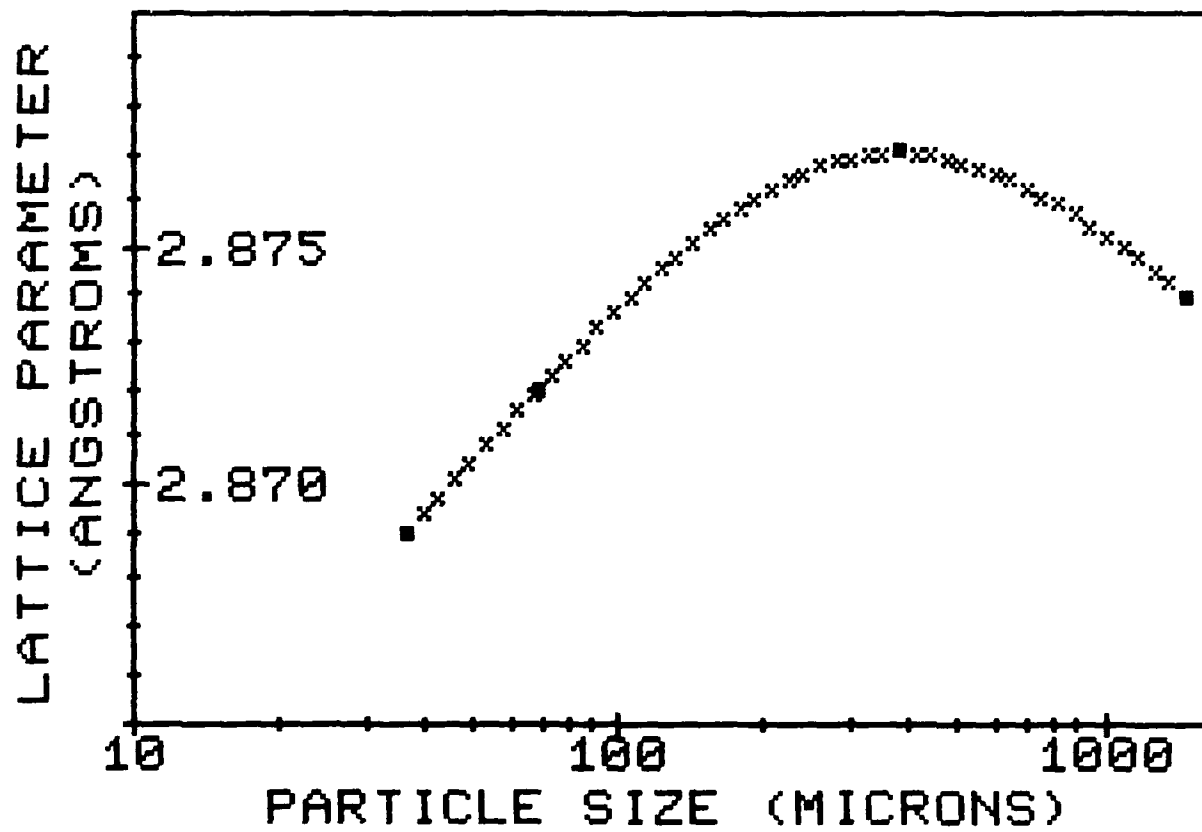
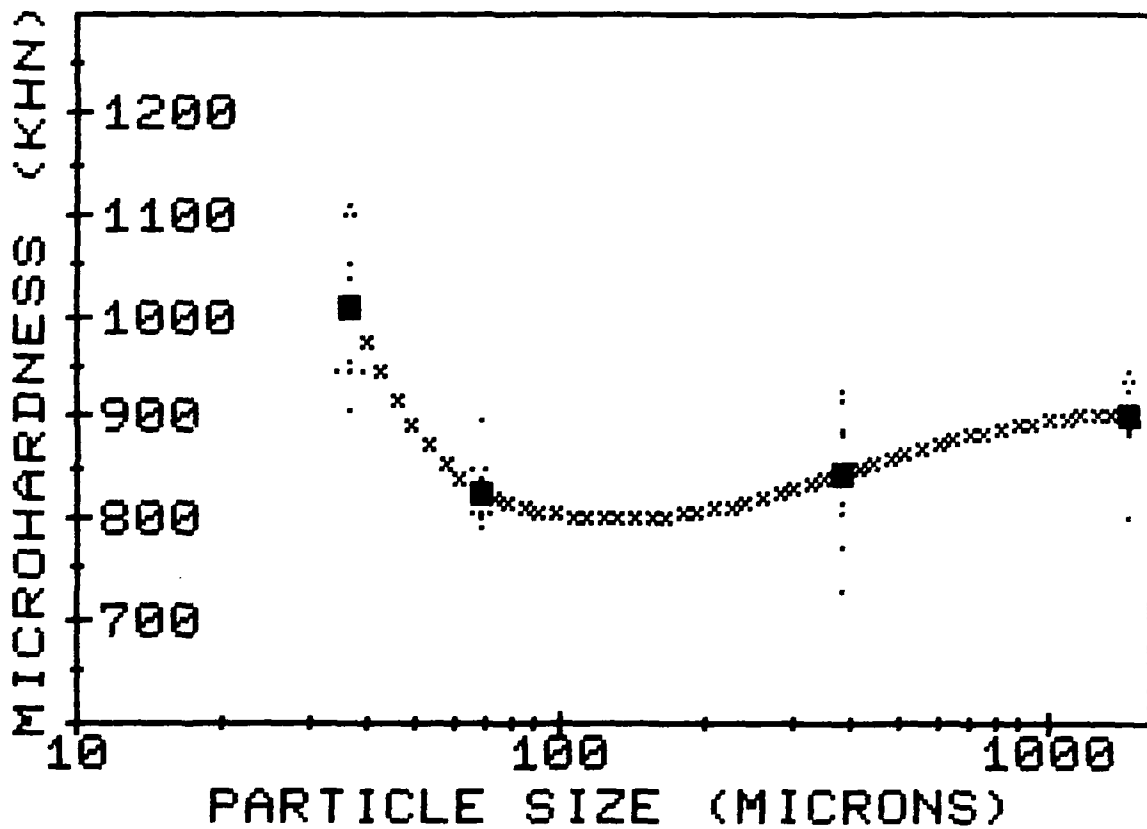
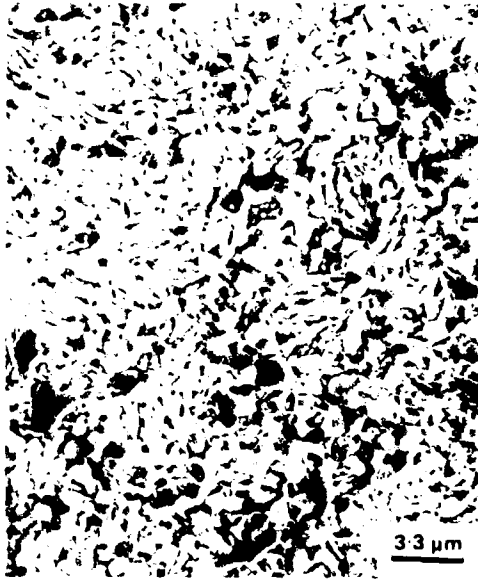
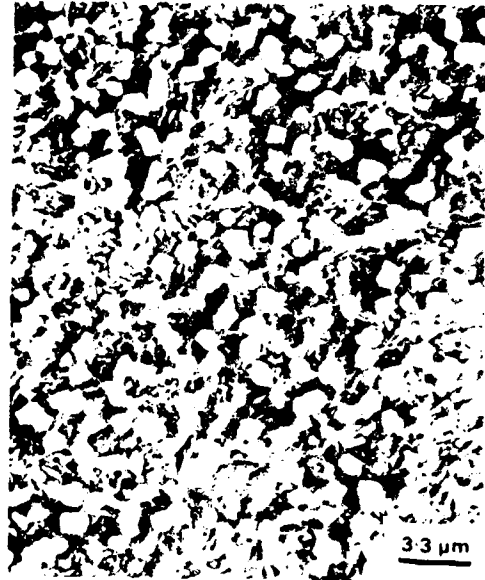


Figure 48. Lattice parameter of annealed powder as a function of particle size.



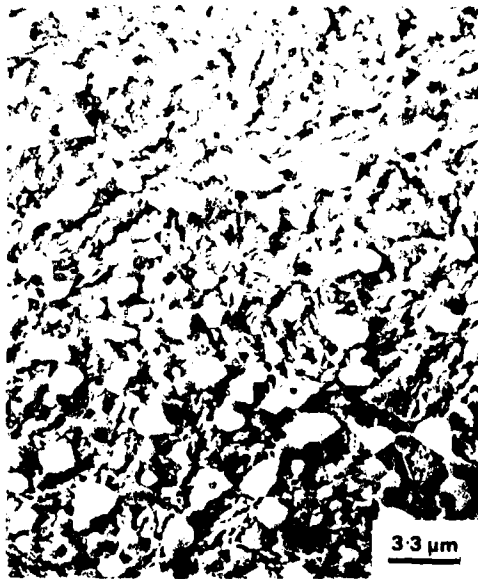


(a)

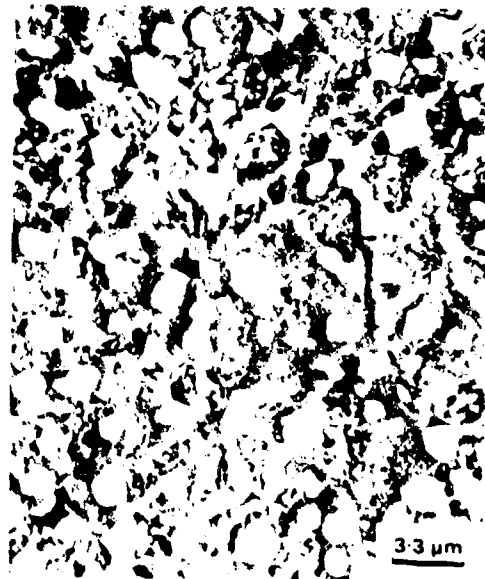


(b)

Figure 50. HIPed (H1); Kalling's etch. SEM. a) 250-840 μm screen.
b) $\leq 44 \mu\text{m}$ screen.

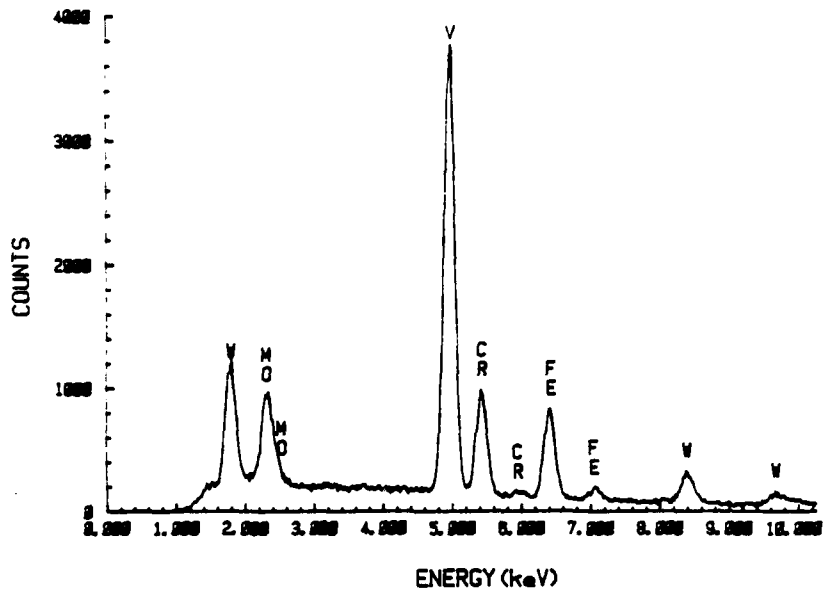


(a)

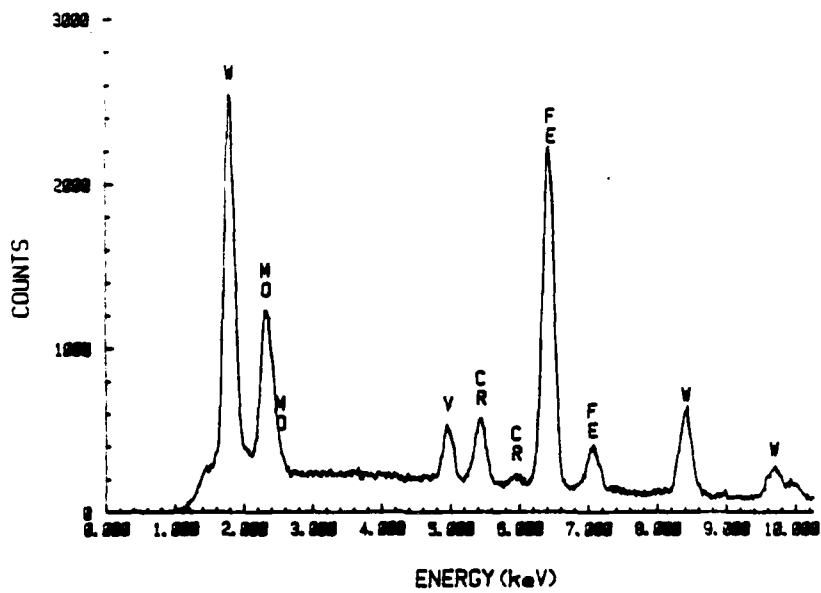


(b)

Figure 51. HIPed (H2); Kalling's etch. SEM. a) 250-840 μm screen.
b) $\leq 44 \mu\text{m}$ screen.

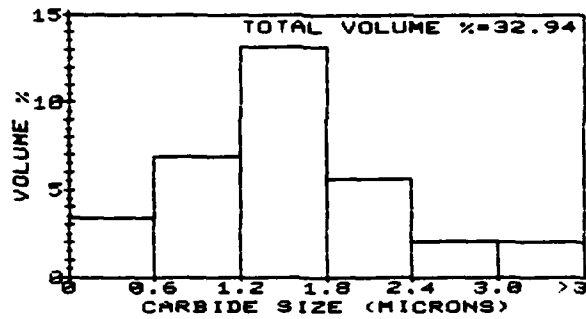


(a)

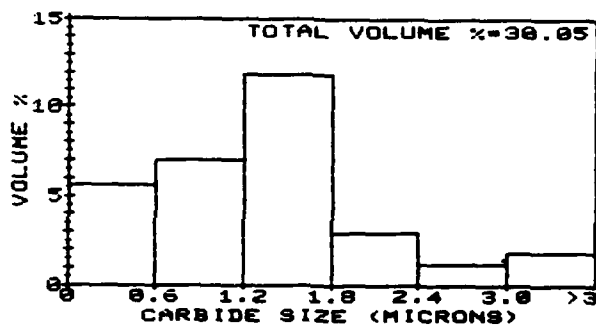


(b)

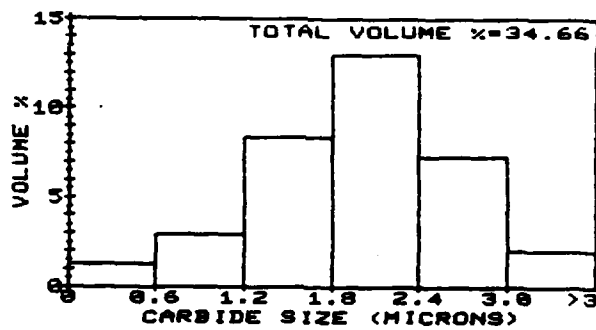
Figure 52. HIPed(H2)/ ≤ 44 μm screen. EDAX Spectrum. a) MC. b) M₆C.



(a)

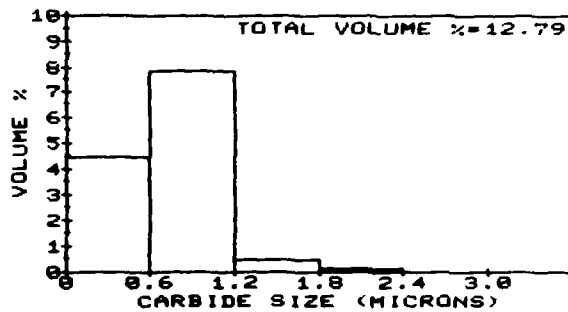


(b)

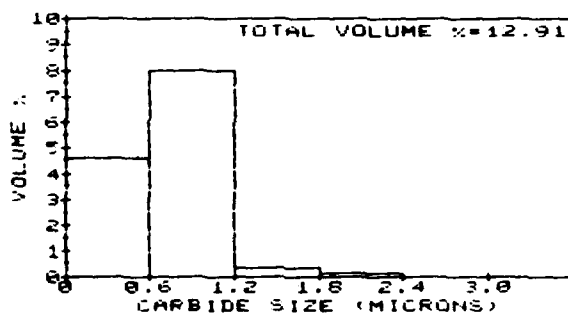


(c)

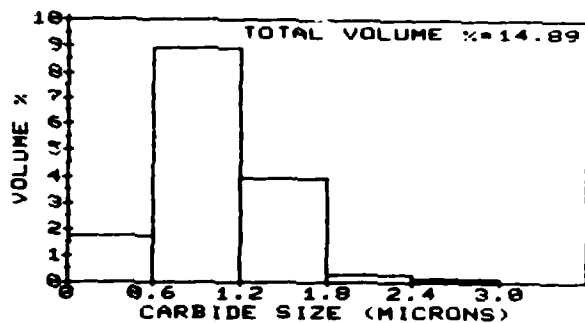
Figure 53. Size distribution - M.C. a) H1/250-840 μm screen. b) H1/ ≤ 44 μm screen. c) H2/250-840 μm screen.



(a)



(b)

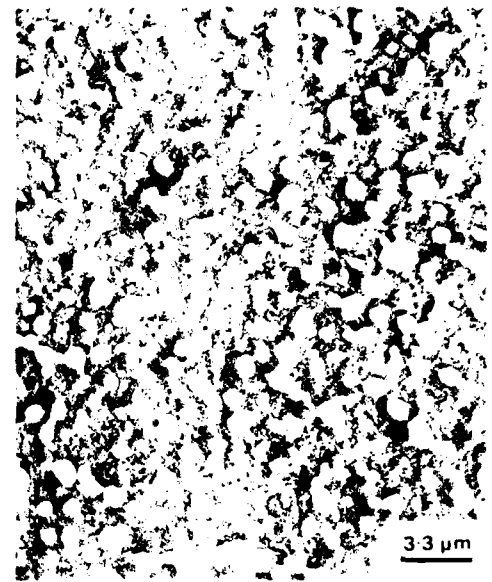


(c)

Figure 54. Size distribution - MC. a) H1/250-840 μm screen. b) H1/44 μm screen. c) H2/250-840 μm screen.



(a)

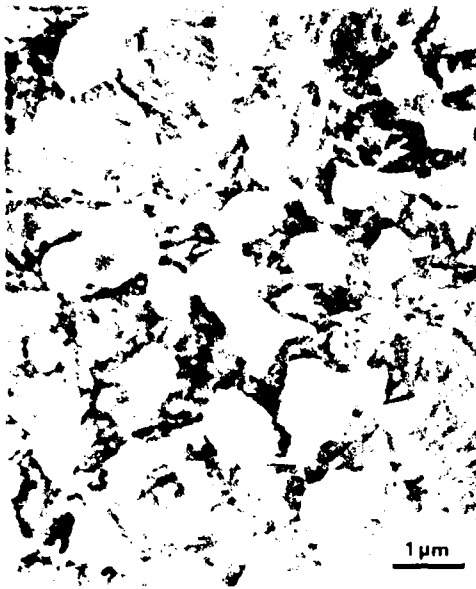


(b)

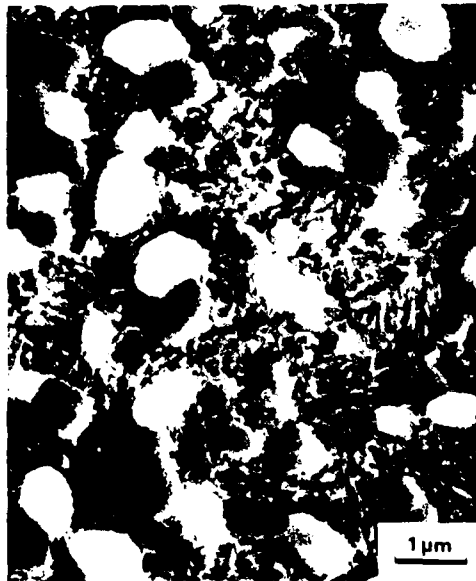


(c)

Figure 55. Heat-treated material, 20-80 μm screen; Kalling's etch, SEM.
a) H1+A1, b) H1+A1+T1, c) H1+A1+T2.



(a)



(b)

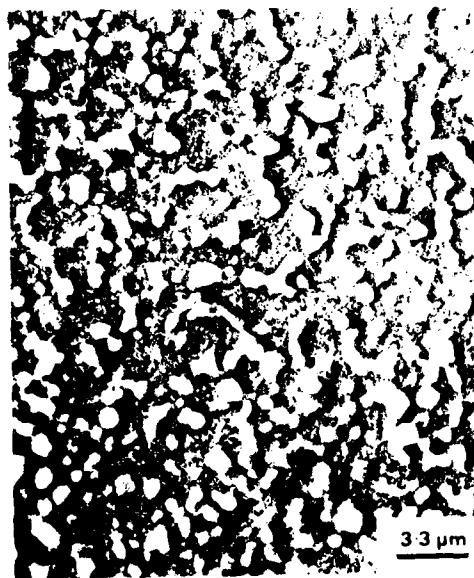
Figure 56. Heat-treated material; Kalling's etch. SEM. a) H1+A1/ $\le 44 \mu\text{m}$ screen. b) H1+A1+T1/250-840 μm screen.



(a)

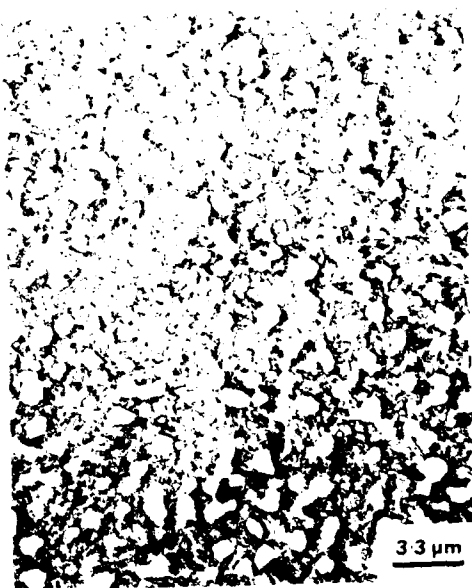


(b)

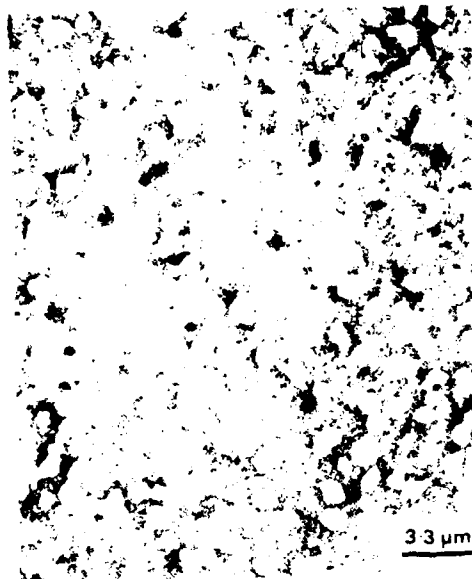


(c)

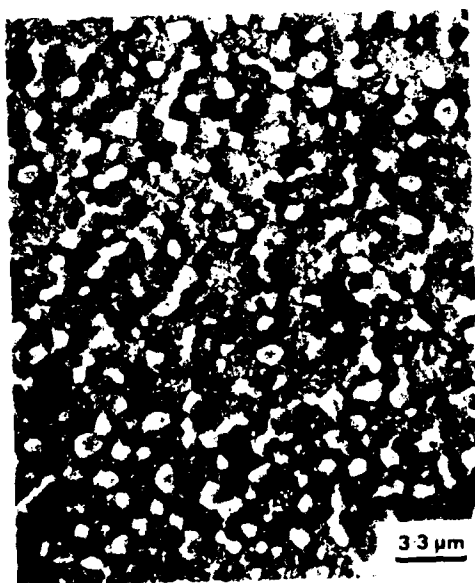
Figure 57. Heat-treated material, 250-850 μm screen; Kalling's etch, SEM.
a) H1+A2. b) H1+A2+T1. c) H1+A2+T3.



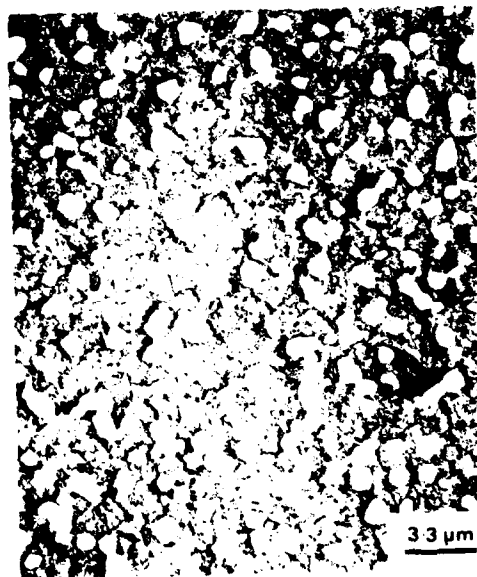
(a)



(b)

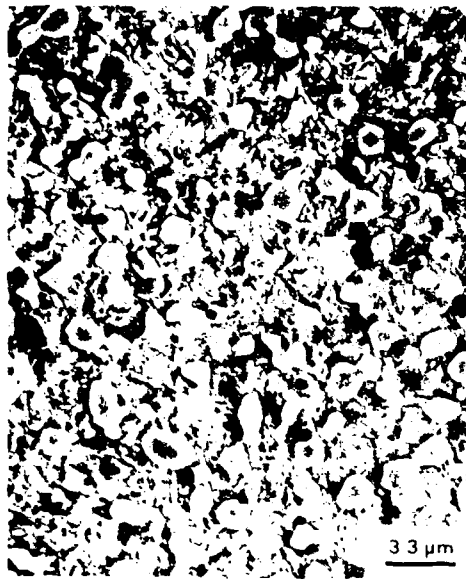


(c)

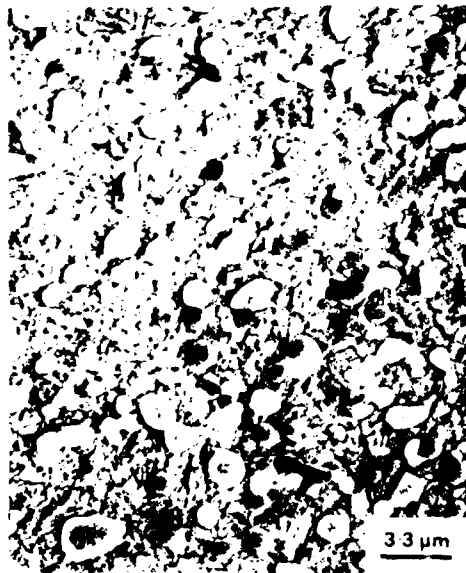


(d)

Figure 58. Heat-treated material, 100 μm screen; Kallina's etch. SEM.
a) H1+Al, b) H1+Al+Ti, c) H1+Al+Ta, d) H1+Al.

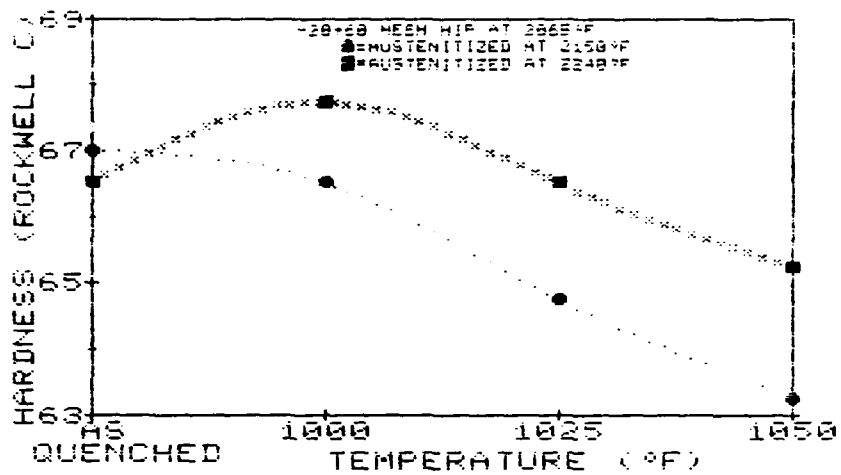


(a)

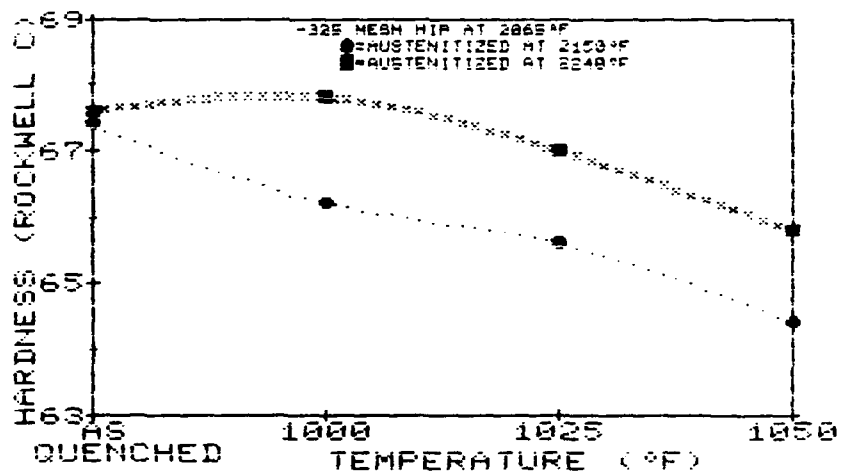


(b)

Figure 59. Heat-treated material, 250-840 μm screen; Kalling's etch. SEM.
a) H₂+Al. b) H₂+Al₂.

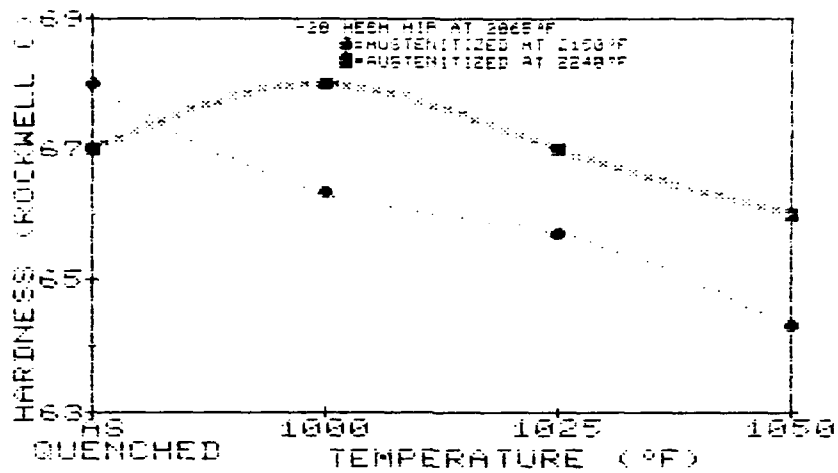


(a)

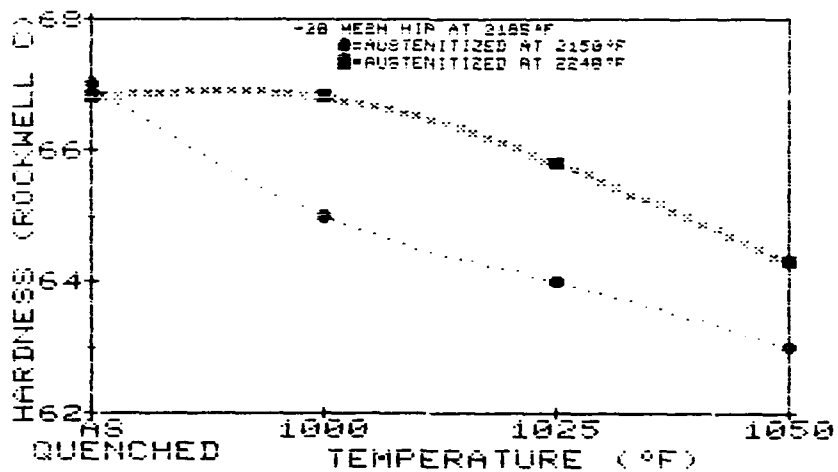


(b)

Figure 60. Hardness as a function of austenitizing temperature and tempering temperature. HIPed (H1). (Indentation load = 25 g). a) 250-840 μm screen. b) <44 μm screen.



(a)



(b)

Figure 61. Hardness as a function of austenitizing temperature and tempering temperature. ≤ 840 μ m screen. (Indentation load = 25g). a) HIPed (H1). b) HIPed (H2).

APPENDIX: CARBIDE SIZE DISTRIBUTIONS IN P/M T15

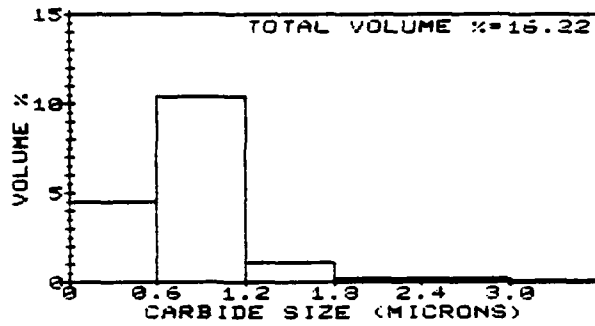


Figure A1. Size distribution - MC;
H1/250-840 μm screen.

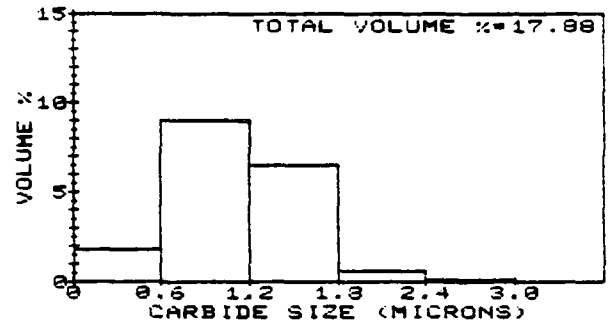


Figure A2. Size distribution - MC;
H2/250-840 μm screen.

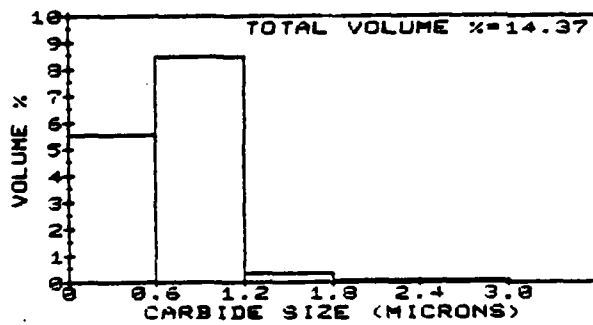


Figure A3. Size distribution - MC;
H1/ ≤ 44 μm screen.

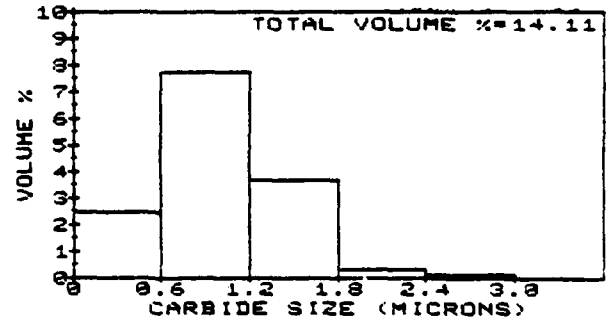


Figure A4. Size distribution - MC;
H2/ ≤ 44 μm screen.

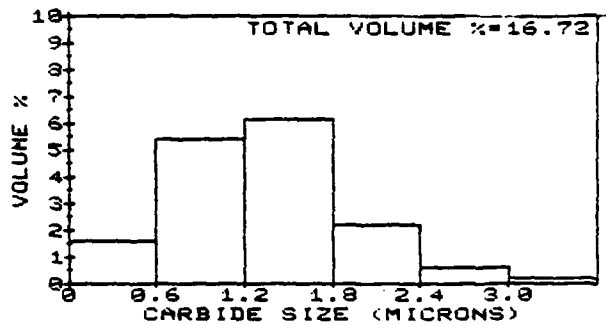


Figure A5. Size distribution - M_6C ; H1/250-840 μm screen.

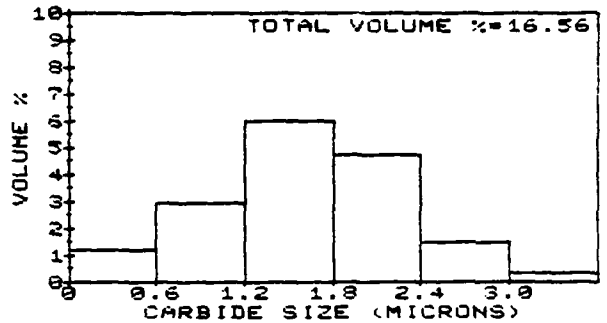


Figure A6. Size distribution - M_6C ; H2/250-840 μm screen.

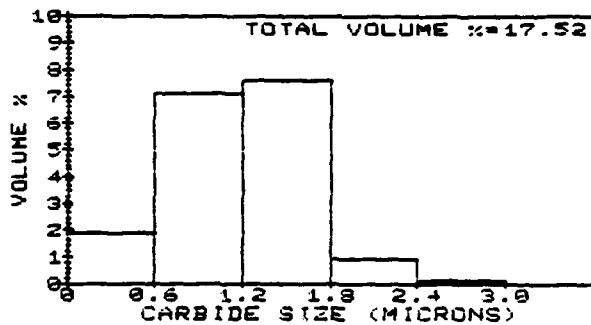


Figure A7. Size distribution - M_6C ; H1/ ≤ 44 μm screen.

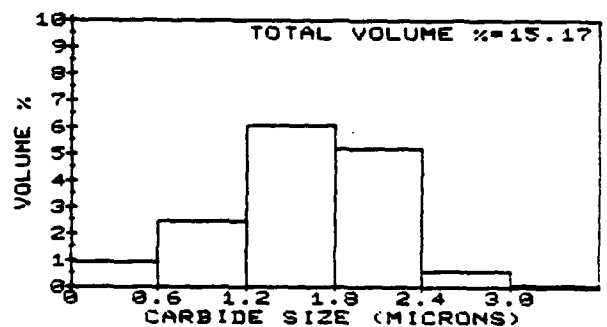


Figure A8. Size distribution - M_6C ; H2/ ≤ 44 μm screen.

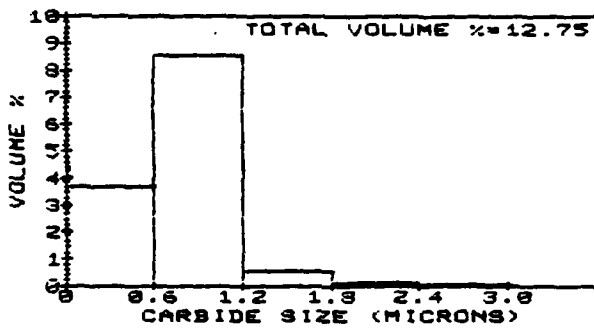


Figure A9. Size distribution - MC;
H1+A2/250-840 μm screen.

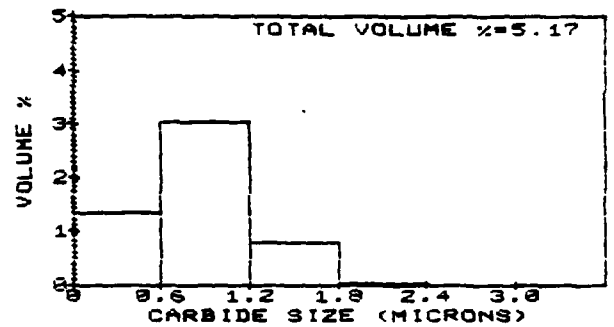


Figure A10. Size distribution - M_6C ;
H1+A2/250-840 μm screen.

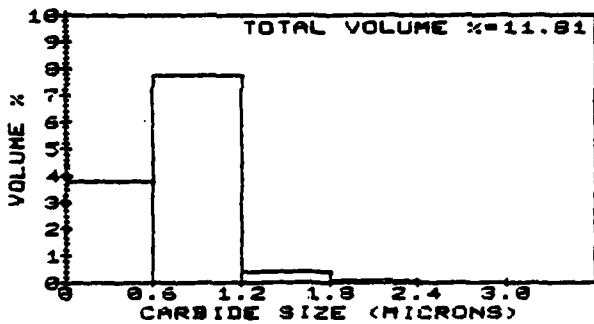


Figure A11. Size distribution - MC;
H1+A2+I1/250-840 μm screen.

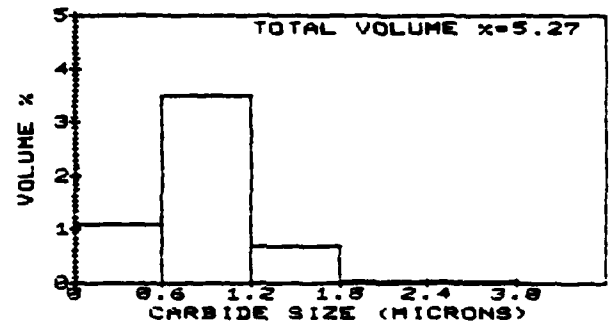


Figure A12. Size distribution - M_6C ;
H1+A2+I1/250-840 μm screen.

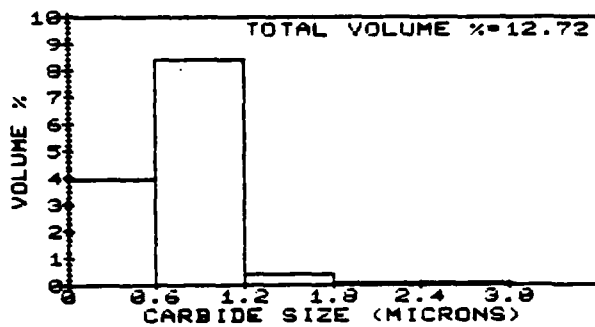


Figure A13. Size distribution - MC;
H1+A2+T2/250-840 μ m
screen.

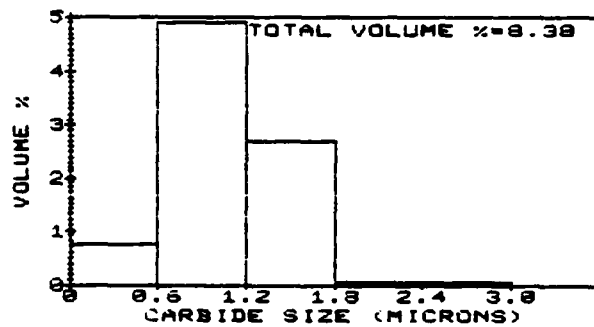


Figure A14. Size distribution - M₆C;
H1+A2+T2/250-840 μ m
screen.

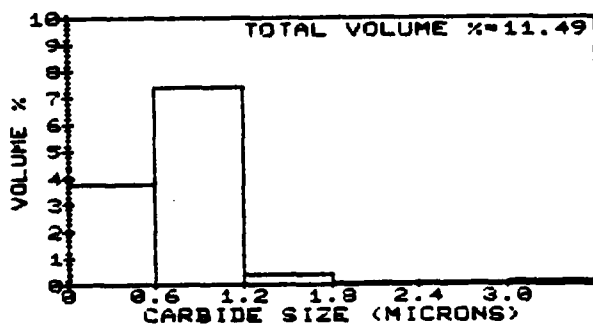


Figure A15. Size distribution - MC;
H1+A2+T3/250-840 μ m
screen.

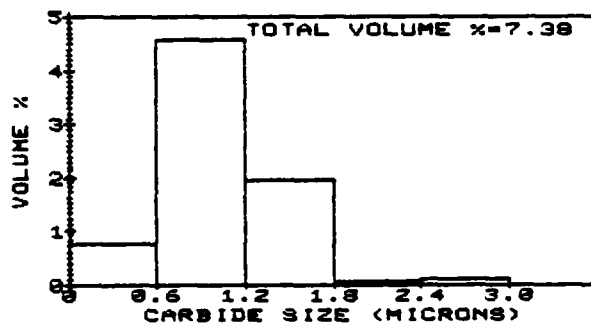


Figure A16. Size distribution - M₆C;
H1+A2+T3/250-840 μ m
screen.

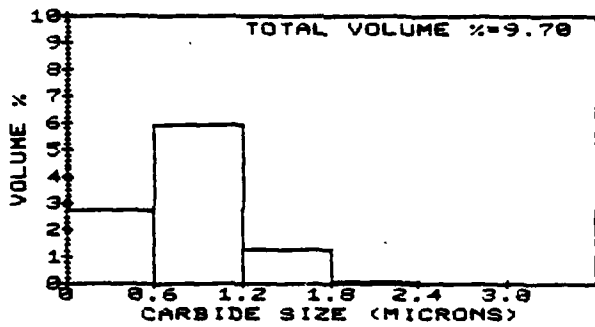


Figure A17. Size distribution - MC; H2+Al/250-840 μm screen.

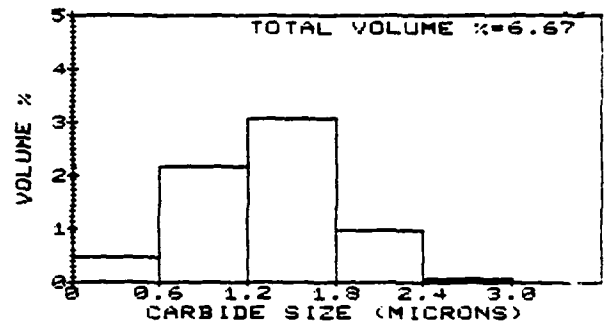


Figure A18. Size distribution - M₆C; H2+Al/250-840 μm screen.

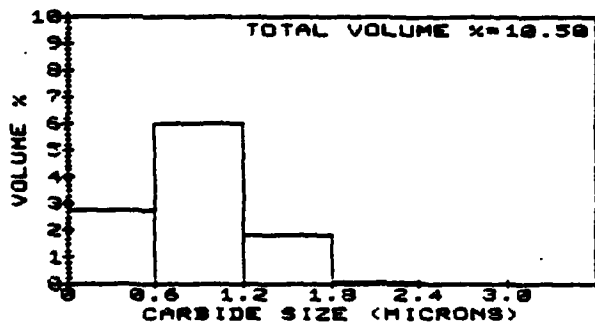


Figure A19. Size distribution - MC; H2+Al+Ti/250-840 μm screen.

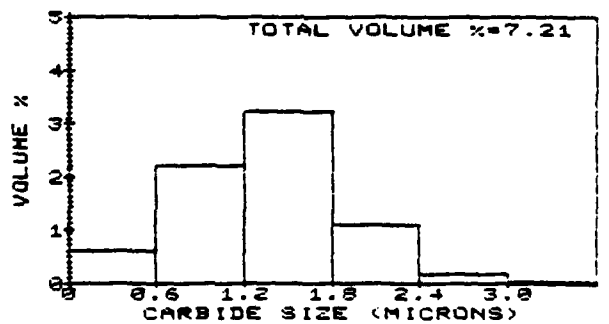


Figure A20. Size distribution - M₆C; H2+Al+Ti/250-840 μm screen.

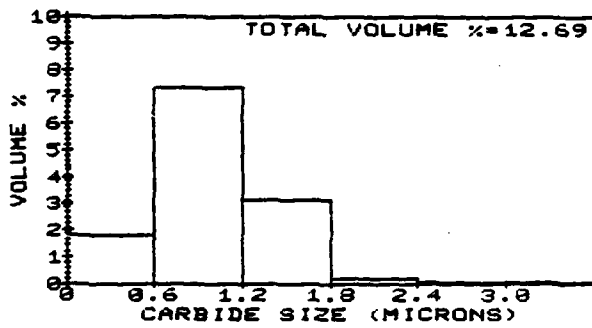


Figure A21. Size distribution - MC;
H2+Al+T2/250-840 μm
screen.

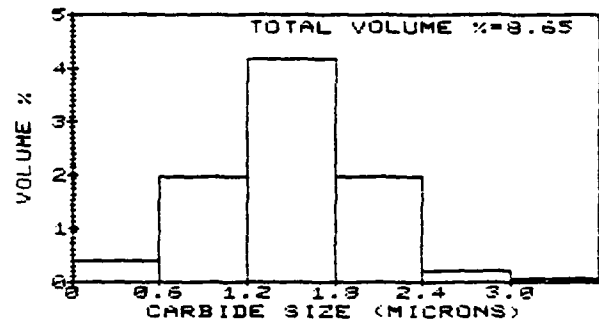


Figure A22. Size distribution - M₆C;
H2+Al+T2/250-840 μm
screen.

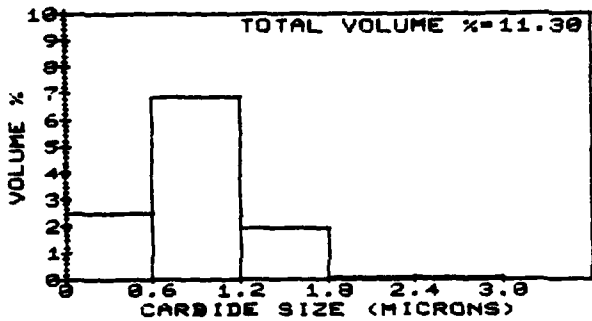


Figure A23. Size distribution - MC;
H2+Al+T3/250-840 μm
screen.

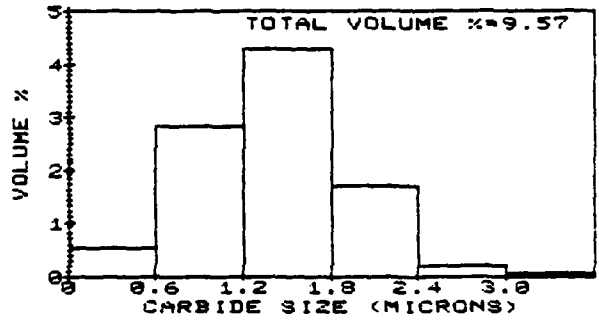


Figure A24. Size distribution - M₆C;
H2+Al+T3/250-840 μm
screen.

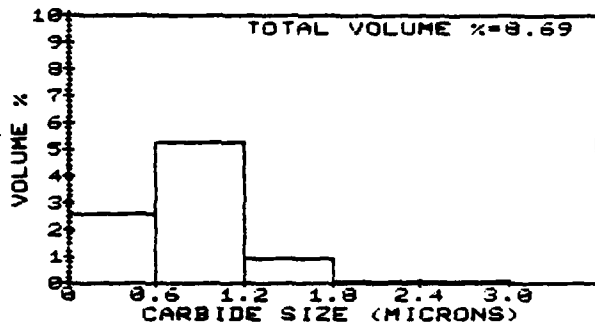


Figure A25. Size distribution - MC; H2+A2/250-840 μ m screen.

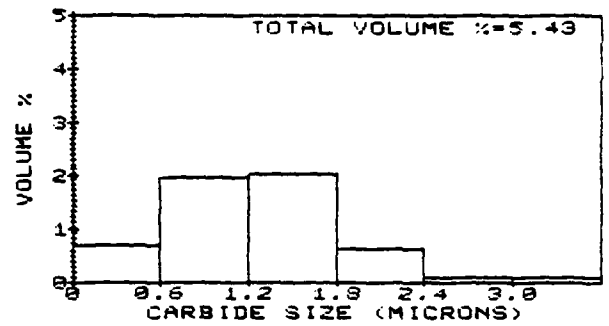


Figure A26. Size distribution - M₆C; H2+A2/250-840 μ m screen.

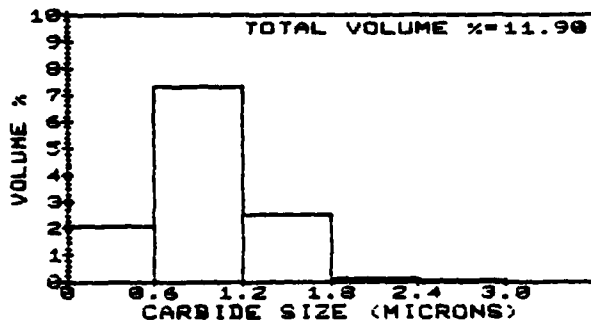


Figure A27. Size distribution - MC; H2+A2+T1/250-840 μ m screen.

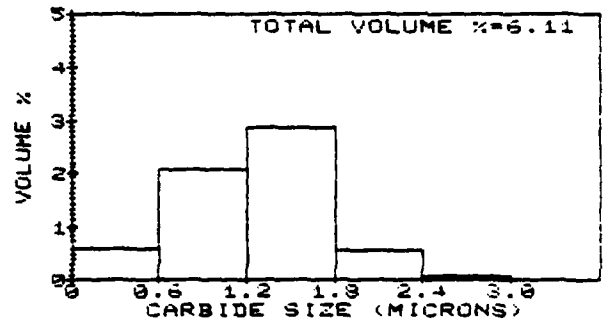


Figure A28. Size distribution - M₆C; H2+A2+T1/250-840 μ m screen.

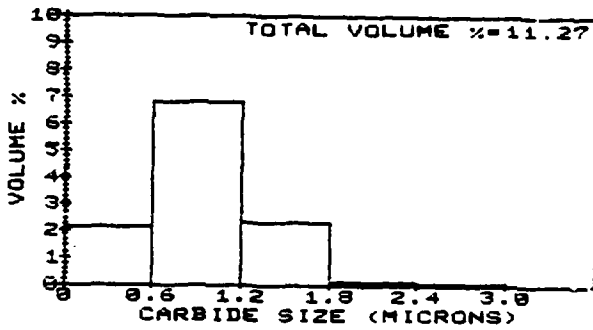


Figure A29. Size distribution - MC; H2+A2+T2/250-840 μ m screen.

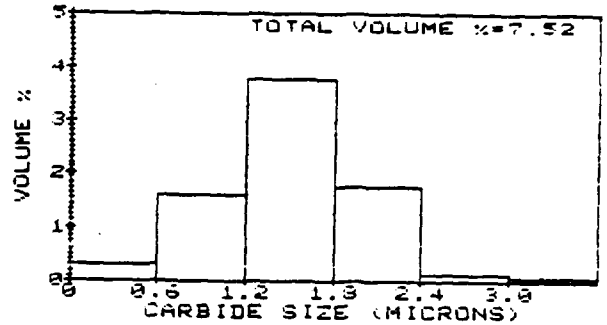


Figure 30. Size distribution - M₆C; H2+A2+T2/250-840 μ m screen.

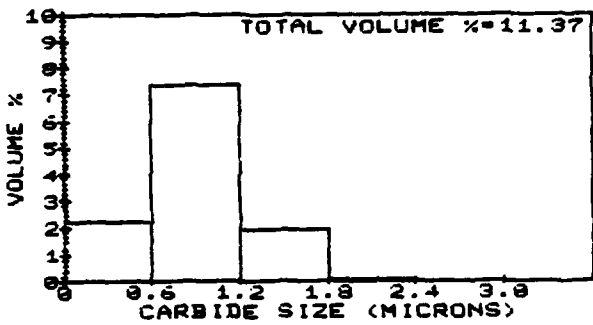


Figure A31. Size distribution - MC; H2+A2+T3/250-840 μ m screen.

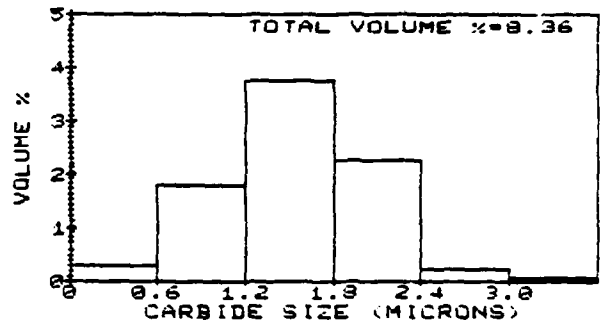


Figure A32. Size distribution - M₆C; H2+A2+T3/250-840 μ m screen.

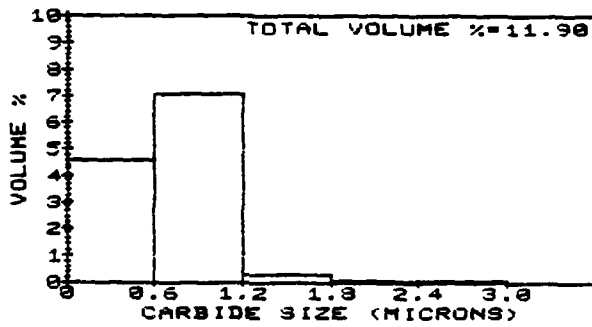


Figure A33. Size distribution - MC;
H1+A2/≤44 μm screen.

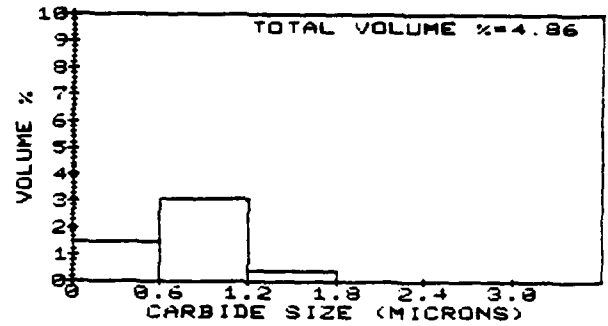


Figure A34. Size distribution - M₆C;
H1+A2/≤44 μm screen.

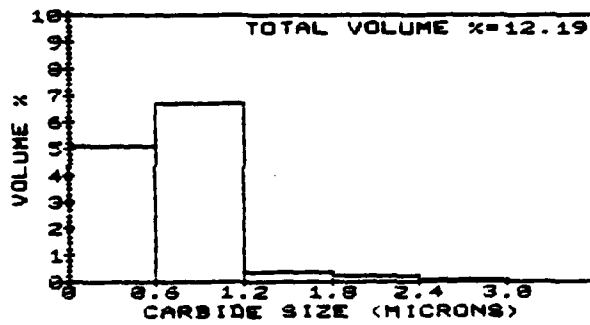


Figure A35. Size distribution - MC;
H1+A2+T1/≤44 μm screen.

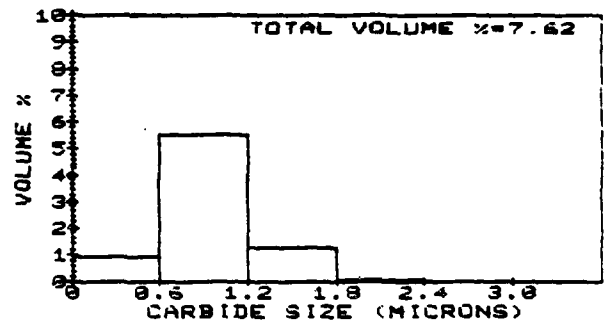


Figure A36. Size distribution - M₆C;
H1+A2+T1/≤44 μm screen.

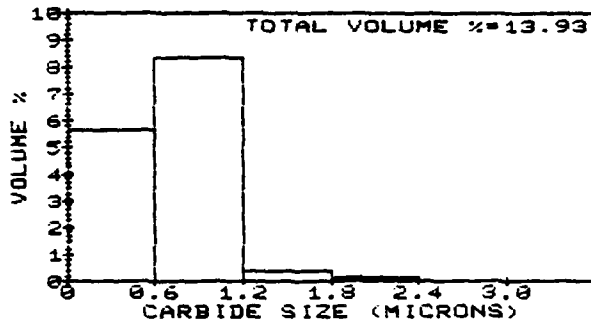


Figure A37. Size distribution - MC;
H1+A2+T2/≤44 μm screen.

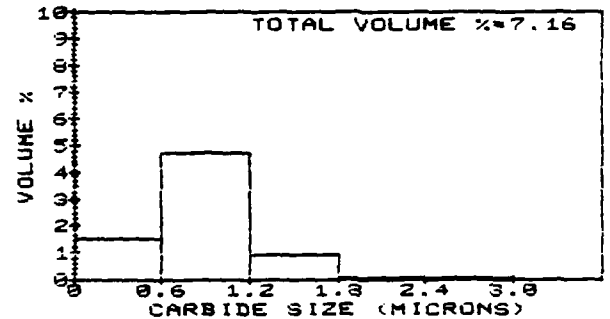


Figure A38. Size distribution - M₆C;
H1+A2+T2/≤44 μm screen.

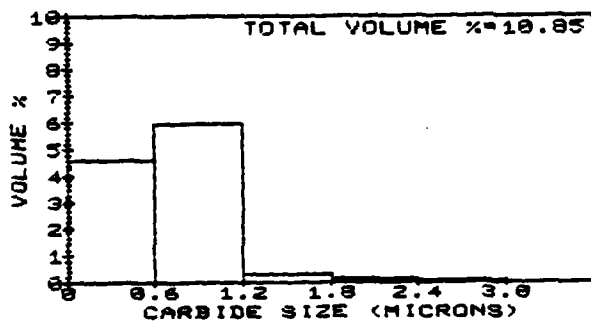


Figure A39. Size distribution - MC;
H1+A2+T3/≤44 μm screen.

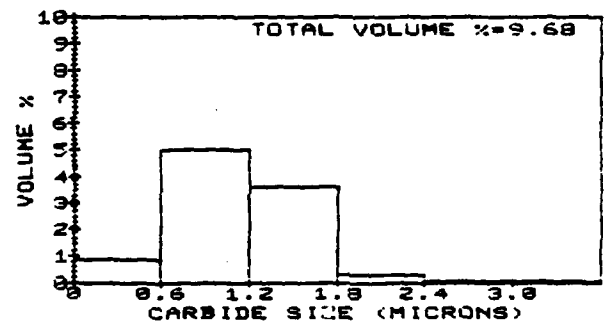


Figure A40. Size distribution - M₆C;
H1+A2+T3/≤44 μm screen.

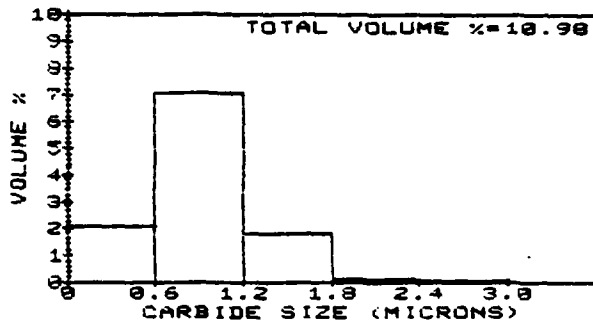


Figure A41. Size distribution - MC; H2+Al/≤44 μm screen.

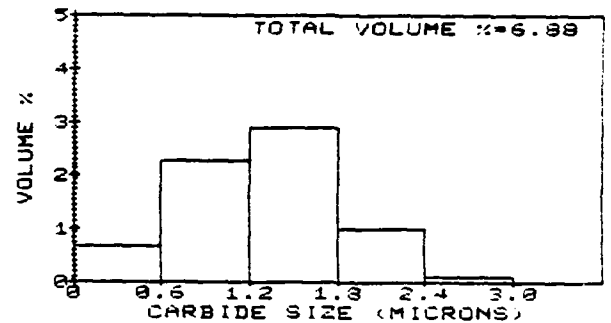


Figure A42. Size distribution - M₆C; H2+Al/≤44 μm screen.

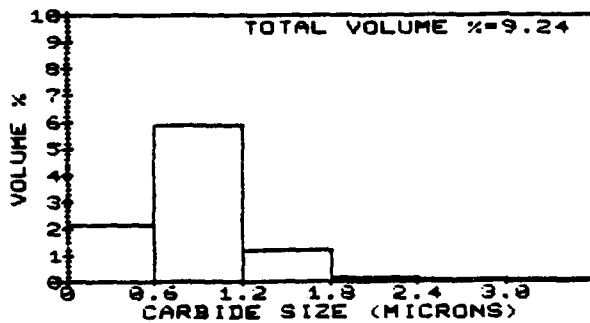


Figure A43. Size distribution - MC; H2+Al+Ti/≤44 μm screen.

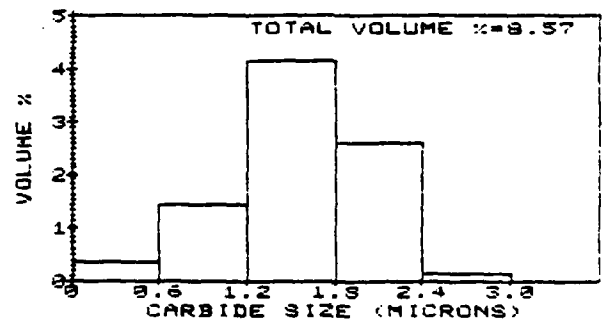


Figure A44. Size distribution - M₆C; H2+Al+Ti/≤44 μm screen.

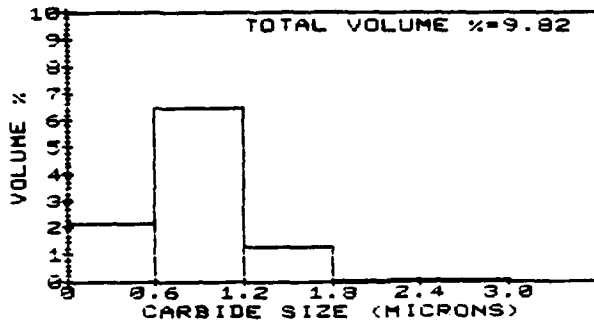


Figure A45. Size distribution - MC;
H2+Al+T2/≤44 μm screen.

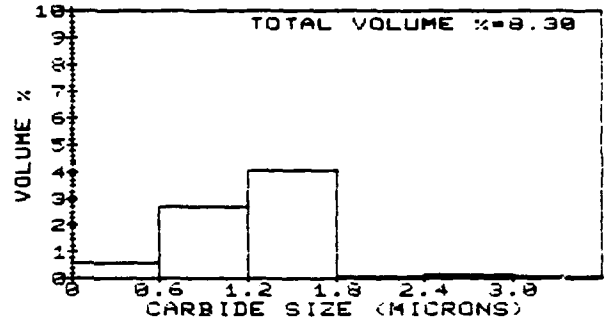


Figure A46. Size distribution - M₆C;
H2+Al+T2/≤44 μm screen.

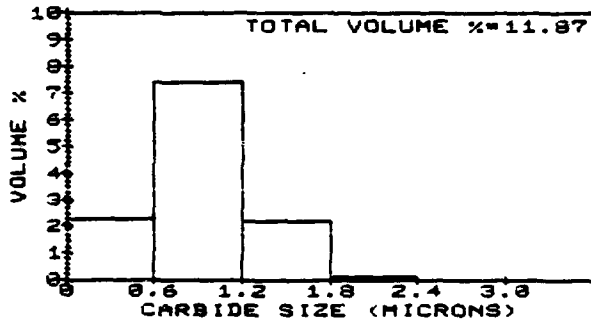


Figure A47. Size distribution - MC;
H2+Al+T3/≤44 μm screen.

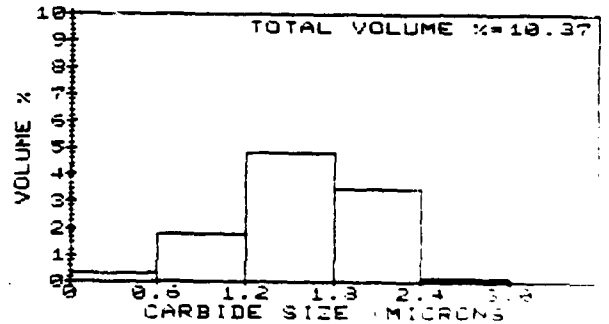


Figure A48. Size distribution - M₆C;
H2+Al+T3/≤44 μm screen.

AD-A126 163

A FUNDAMENTAL STUDY OF TOOL STEELS PROCESSED FROM
RAPIDLY SOLIDIFIED POWDERS(U) DREXEL UNIV PHILADELPHIA
PA DEPT OF MATERIALS ENGINEERING A LAWLEY ET AL.
JAN 83 N00014-81-K-0039

2/2

UNCLASSIFIED

F/G 11/6

NL



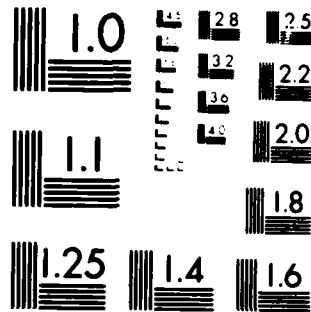
END

DATE

FILMED

1 5 1

DTIC



MICROCOPY RESOLUTION TEST CHART
NATIONAL BUREAU OF STANDARDS-1963-A

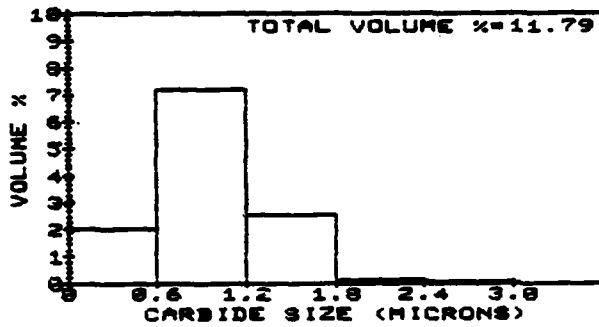


Figure A49. Size distribution - MC;
H2+A2+T1/≤44 μm screen.

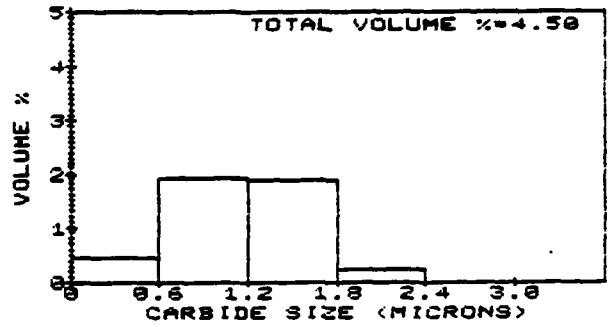


Figure A50. Size distribution - M₆C;
H2+A2+T1/≤44 μm screen.

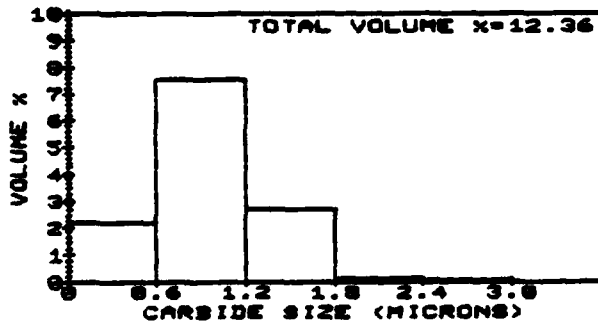


Figure A51. Size distribution - MC;
H2+A2+T2/≤44 μm screen.

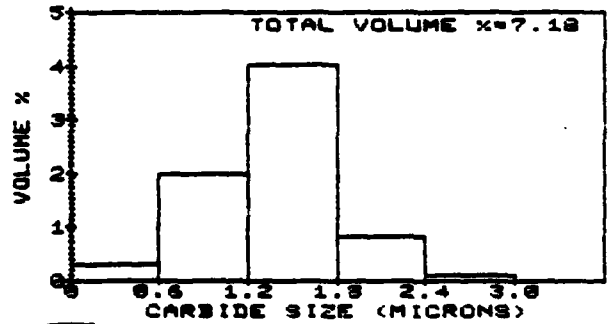


Figure A52. Size distribution - M₆C;
H2+A2+T2/≤44 μm screen.

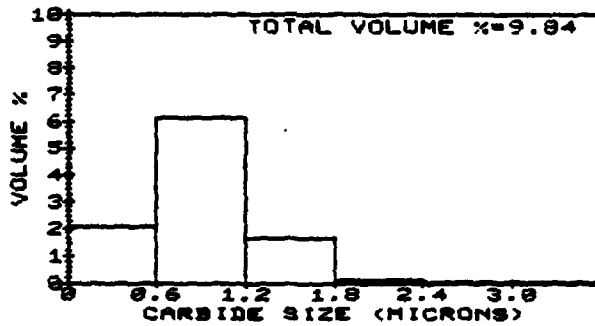


Figure A53. Size distribution - MC;
H2+A2+T3/≤44 μm screen.

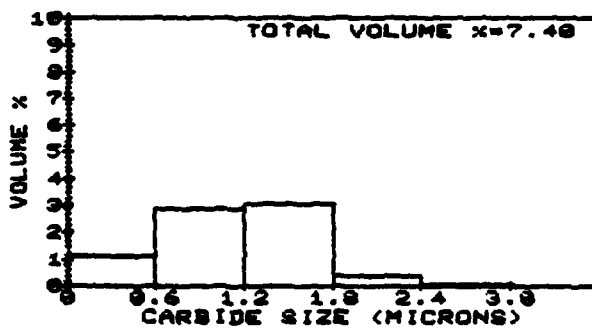


Figure A54. Size distribution - M₆C;
H2+A2+T3/≤44 μm screen.

PRESENTATIONS, REPORTS AND PUBLICATIONS

"Powder Metallurgy Tool Steels", Drexel University, Philadelphia, PA, January 1982.

"Rapid Solidification Science and Technology", University of Illinois, Urbana, Illinois, May 1982.

"Rapid Solidification Science and Technology", Westinghouse R and D Center, Pittsburgh, PA, May 1982.

"Powder Metallurgy and Rapid Solidification Technology-Specialty Alloys", Cabot Corporation, Kokomo, Indiana, May 1982.

"Iron-Base Powder Metallurgy Specialty Alloys", Bethlehem Steel Corporation, Bethlehem, PA, June 1982.

"A Fundamental Study of Tool Steels Processed From Rapidly Solidified Powders", ONR Technical Report, December 1981 (A. Lawley and M. J. Koczak).

"The Microstructure of Tool Steels Processed from Rapidly Solidified Powders", Rapid Solidification Processing: Principles and Technologies, Nat. Bureau of Standards, Gaithersburg, Maryland - in press (K.S. Kumar, M.J. Koczak and A. Lawley).

BASIC DISTRIBUTION LIST

Technical and Summary Reports October 1980

<u>Organization</u>	<u>Copies</u>	<u>Organization</u>	<u>Copies</u>
Defense Documentation Center Cameron Station Alexandria, VA 22314	12	Naval Air Propulsion Test Center Trenton, NJ 08628 ATTN: Library	1
Office of Naval Research Department of the Navy 800 N. Quincy Street Arlington, VA 22217 ATTN: Code 471 Code 470	1 1	Naval Construction Battalion Civil Engineering Laboratory Port Hueneme, CA 93043 ATTN: Materials Division	1
Commanding Officer Office of Naval Research Branch Office Building 114, Section D 666 Summer Street Boston, MA 02210	1	Naval Electronics Laboratory San Diego, CA 92152 ATTN: Electron Materials Sciences Division	1
Commanding Officer Office of Naval Research Branch Office 536 South Clark Street Chicago, IL 60605	1	Naval Missile Center Materials Consultant Code 3312-1 Point Mugu, CA 92041	1
Office of Naval Research Western Regional Office 1030 East Green St Pasadena, CA 91106	1	Commanding Officer Naval Surface Weapons Center White Oak Laboratory Silver Spring, MD 20910 ATTN: Library	1
Naval Research Laboratory Washington, DC 20375 ATTN: Codes 6000 6100 6300 2627	1 1 1 1	Commander David W. Taylor Naval Ship Research and Development Center Bethesda, MD 20084	1
Naval Air Development Center Code 606 Warminster, PA 18974 ATTN: Dr. J. DeLuccia	1	Naval Oceans Systems Center San Diego, CA 92132 ATTN: Library	1
		Naval Underwater System Center Newport, RI 02840 ATTN: Library	1
		Naval Postgraduate School Monterey, CA 93940 ATTN: Mechanical Engineering Department	1
		Naval Weapons Center China Lake, CA 93555 ATTN: Library	1

BASIC DISTRIBUTION LIST (cont'd)

<u>Organization</u>	<u>Copies</u>	<u>Organization</u>	<u>Copies</u>
Naval Air Systems Command Washington, DC 20360 ATTN: Codes 52031 52032	1 1	NASA Lewis Research Center 21000 Brookpark Road Cleveland, OH 44135 ATTN: Library	1
Naval Sea System Command Washington, DC 20362 ATTN: Code 05R	1	National Bureau of Standards Washington, DC 20234 ATTN: Metals Science and Standards Division	1
Naval Facilities Engineering Command Alexandria, VA 22331 ATTN: Code 03	1	Ceramics Glass and Solid State Science Division Fracture and Deformation Division	1 1
Scientific Advisor Commandant of the Marine Corps Washington, DC 20380 ATTN: Code AX	1	Director Applied Physics Laboratory University of Washington 1013 Northeast Forthieth Street Seattle, WA 98105	1
Army Research Office P. O. Box 12211 Triangle Park, NC 27709 ATTN: Metallurgy & Ceramics Program	1	Defense Metals and Ceramics Information Center Battelle Memorial Institute 505 King Avenue Columbus, OH 43201	1
Army Materials and Mechanics Research Center Watertown, MA 02172 ATTN: Research Programs Office		Metals and Ceramics Division Oak Ridge National Laboratory P. O. Box X Oak Ridge, TN 37380	1
Air Force Office of Scientific Research/NE Building 410 Bolling Air Force Base Washington, DC 20332 ATTN: Chemical Science Directorate Electronics & Materials Science Directorate	1 1	Los Alamos Scientific Laboratory P. O. Box 1663 Los Alamos, NM 87544 ATTN: Report Librarian	1
Air Force Materials Laboratory Wright-Patterson AFB Dayton, OH 45433	1	Argonne National Laboratory Metallurgy Division P. O. Box 229 Lemont, IL 60439	1
Library Building 50, Room 134 Lawrence Radiation Laboratory Berkeley, CA	1	Brookhaven National Laboratory Technical Information Division Upton, Long Island New York 11973 ATTN: Research Library	1
NASA Headquarters Washington, DC 20546 ATTN: Code RRM	1		